

Ultrafast Quasiparticle Dynamics in Graphene and 2D Heterostructures

Dissertation

zur Erlangung des Doktorgrades an der Fakultät für
Mathematik, Informatik und Naturwissenschaften

Fachbereich Physik
der Universität Hamburg

Vorgelegt von
Sven Aeschlimann
aus Zürich, Schweiz

Hamburg
2018

Gutachter der Dissertation: Dr. Isabella Gierz
Prof. Dr. Ludwig Mathey

Zusammensetzung der Prüfungskommission:
Dr. Isabella Gierz
Prof. Dr. Ludwig Mathey
Prof. Dr. Michael Potthoff
Prof. Dr. Martin Eckstein
Prof. Dr. Henning Moritz

Vorsitzender der Prüfungskommission: Prof. Dr. Michael Potthoff

Datum der Disputation: 04.02.2019

Vorsitzender des Promotionsausschusses: Prof. Dr. Wolfgang Hansen

Leiter des Fachbereich Physik: Prof. Dr. Michael Potthoff

Dekan der Fakultät MIN: Prof. Dr. Heinrich Graener

To my Mother

Abstract

The intriguing electronic properties of graphene and other two-dimensional (2D) materials are the basis for many advances in fundamental solid state science and technological applications. Tremendous effort has been and still is made from universities, research institutes and technology ventures worldwide towards an industrialization of 2D material-based devices and products.

Graphene, a semi-metal with zero bandgap and quasiparticles that carry Dirac properties, possesses extremely high carrier mobilities and unique optical properties. The linear bandstructure and the pseudospin of the Dirac carriers are known to have decisive influence on scattering amplitudes and dynamical properties of graphene. Among these the prevention of backscattering and existence of Kleintunneling are probably the most peculiar effects. The bearing of Dirac properties are further disclosed by photon-induced pseudospin flips and a remarkable resonance for forward scattering.

Other 2D materials such as monolayers of hexagonal boron nitride (hBN) and transition metal dichalcogenides (TMDCs) feature similar practicalities such as robustness, flexibility and transparency, while offering complementary electronic properties to those of graphene. For example, monolayer TMDCs are direct gap semiconductors with broken inversion symmetry that lifts the spin degeneracy of the band structure in the presence of strong spin-orbit coupling.

As most applications of electronics, optoelectronics and spintronics operate far from equilibrium, the development of such devices requires a thorough understanding of the dynamical properties of materials under these conditions. Therefore, it is essential to investigate out-of-equilibrium femtosecond quasiparticle dynamics which define the feasibility and efficiency of implementing graphene and other 2D materials into novel device structures. This work was set out to investigate ultrafast quasiparticle scattering dynamics in pho-

toexcited graphene and a TMDC/graphene heterostructure with time and angle-resolved photoemission spectroscopy (trARPES). The technique combines ultrafast pump-probe spectroscopy on a femtosecond timescale with the capability of spectral sampling of valence electrons in the energy- and momentum-space. Redistributing quasiparticles by optical excitation establishes non-thermal carrier distributions, the relaxation of which reveals information about the out-of-equilibrium behavior of complex quantum systems. Unlike other techniques, trARPES enables a direct view on transient electronic distributions as they evolve in time due to manybody scattering events. The trARPES laboratory at the Max Planck Institute for the Structure and Dynamics of Matter in Hamburg uses high harmonics generation for full Brillouin zone mapping and tunable pump photon energies for tailored pulsed photoexcitation schemes.

The experiments presented in this thesis revealed the importance of both Auger and other collinear electron-electron scattering processes in the primary thermalization dynamics of photoexcited graphene. These processes directly affect the performance of graphene-based optoelectronic devices such as photodetectors, solar cells, and ultrafast THz laser amplification.

Further, the suitability of two-dimensional WS₂/graphene heterostructures for optical spin-injection into graphene was assessed. In these experiments photoexcitation in resonance to the WS₂ exciton was found to result in an ultrafast charge transfer between the WS₂ layer and graphene. Under photoexcitation with circular polarization the observed charge transfer is expected to be accompanied by spin transfer motivating further investigations of this system with spin-resolved trARPES.

Finally, a method to induce a topological phase transition in graphene by irradiation with strong circularly polarized laser pulses was investigated. The approach relies on the coherent interaction between light and Bloch electrons, i.a. resulting in the formation of photon-dressed states. The successful generation of these “Floquet” sidebands in bulk WSe₂ and the failure thereof in graphene highlights the importance of long electronic scattering times. These findings have important implications for the experimental realization of various theoretically predicted light-induced topological phase transitions.

Zusammenfassung

Die faszinierenden elektronischen Eigenschaften von Graphen und anderen zweidimensionalen (2D) Materialien sind die Grundlage für viele Fortschritte in der fundamentalen Festkörperforschung und für technologische Anwendungen. Universitäten, Forschungsinstitute und Technologieunternehmen setzen sich weltweit für die Industrialisierung von Geräten und Produkten ein, die auf 2D Materialien basieren.

Graphen, ein Halbmetall ohne Bandlücke und Quasiteilchen, die Dirac-Eigenschaften tragen, besitzt extrem hohe Ladungsträgermobilitäten und einzigartige optische Eigenschaften. Es ist bekannt, dass die lineare Bandstruktur und der Pseudospin von Dirac-Ladungsteilchen entscheidenden Einfluss auf Streuamplituden und dynamische Eigenschaften von Graphen haben. Darunter werden vermutlich die Verhinderung von Rückstreuung und die Existenz des Kleintunnels als besonders außergewöhnlich angesehen. Die Auswirkungen von Dirac-Eigenschaften wird auch durch photoneninduzierte Pseudospin-Flips und eine bemerkenswerte Resonanz für die Vorwärtsstreuung offenbart.

Andere 2D-Materialien wie Monolagen von hexagonalem Bornitrid (hBN) und Übergangsmetall-dichalkogeniden (TMDCs) besitzen ähnliche praktische Eigenschaften, die sich durch Robustheit, Flexibilität und Transparenz auszeichnen, während sie komplementäre elektronische Eigenschaften zu Graphen tragen. Zum Beispiel sind Monolagen-TMDCs Halbleiter mit direkter Bandlücke und gebrochener Inversionssymmetrie, wodurch die Spinentartung der Bandstruktur bei starker Spin-Bahn-Kopplung aufgehoben wird.

Da die meisten Anwendungen auf dem Gebiet der Elektronik, Optoelektronik und Spintronik fern vom Gleichgewicht arbeiten, erfordert die Entwicklung solcher Instrumente ein gründliches Verständnis der dynamischen Eigenschaften von Materialien unter diesen Bedingungen. Daher ist es entscheidend, Femtosekunden-Quasiteilchendynamik außerhalb des thermischen Gleichgewichts zu erforschen, um die Machbarkeit und Effizienz der Im-

plementierung von Graphen und anderen 2D-Materialien in neuartige Bauelementstrukturen zu untersuchen.

In dieser Arbeit wurde die ultraschnelle Quasipartikel-Streudynamik in photoangeregtem Graphen und einer TMDC/Graphen-Heterostruktur mit zeit- und winkelaufgelöster Photoemissionsspektroskopie (trARPES) untersucht. Die Technik kombiniert Ultrakurzzeitspektroskopie auf einer Femtosekunden Zeitskala mit der Fähigkeit zur spektralen Auflösung von Valenzelektronen im Energie- und Impulsraum. Die Umverteilung von Quasiteilchen durch optische Anregung stellt nicht-thermische Ladungsträgerverteilungen her, deren Relaxation Informationen über das Verhalten komplexer Quantensysteme fern vom Gleichgewicht liefert. Im Gegensatz zu anderen Techniken ermöglicht trARPES einen direkten Blick auf transiente elektronische Verteilungsfunktionen, die sich aufgrund von Vielteilchenstreuvorgängen über die Zeit verändern. Das trARPES-Labor am Max-Planck-Institut für Struktur und Dynamik der Materie in Hamburg nutzt die Erzeugung von hohen Harmonischen für Messungen über vollständige Brillouinzone und abstimmbare Pump photonenergien für maßgeschneiderte gepulste Photoanregungsschemata.

Die Experimente in dieser Arbeit zeigen die Bedeutung von Auger-Streukanälen und anderen kollinearen Elektron-Elektron-Streuprozessen in der primären Thermalisierungsdynamik von photoangeregtem Graphen auf. Diese Prozesse haben einen direkten Einfluss auf die Leistungsfähigkeit optoelektronischer graphenbasierter Geräte wie Photodetektoren, Solarzellen und ultraschnelle THz-Laserverstärkung.

Weiterhin wurde die Eignung von zweidimensionalen WS_2 /Graphen-Heterostrukturen für die optische Spininjektion in Graphen untersucht. In diesen Experimenten wurde bei Photoanregung in Resonanz mit dem WS_2 -Exziton ein ultraschneller Ladungstransfer zwischen der WS_2 und der Graphen-Schicht festgestellt. Unter Photoanregung mit zirkularer Polarisation wird erwartet, dass der beobachtete Ladungstransfer von Spintransfer begleitet wird. Daraus motivieren sich weitere Untersuchungen mit spinaufgelöster trARPES an diesem System.

Schließlich wurde eine Methode zur Induktion eines topologischen Phasenübergangs in Graphen durch Bestrahlung mit starken zirkular polarisierten Laserpulsen untersucht. Der Ansatz beruht auf der kohärenten Wechselwirkung zwischen Licht und Bloch-Elektronen, was u.a. zur Generierung von *photon-dressed states* führt. Die erfolgreiche Erzeugung dieser "Floquet"-Seitenbänder in WSe_2 und deren Abwesenheit in Graphen unterstreicht die Wichtigkeit langer elektronischer Streuzeiten. Diese Erkenntnisse haben wichtige Implikationen für die experimentelle Realisierung verschiedener theoretisch vorhergesagter lichtinduzierter topologischer Phasenübergänge.

List of Publications

The present thesis is based on my work as a doctoral student at the Max Planck Institute for the Structure and Dynamics of Matter, Hamburg, within the Quantum Condensed Matter Division and at the University of Hamburg. In addition, I am grateful to the *DFG Schwerpunktprogramm 1495 “Graphene”* and the *SFB 925 “Light induced dynamics and control of strongly correlated quantum systems”* for funding the present work.

Publications Relevant for the Thesis

The results presented in this manuscript are based on the following papers:

1. I. Gierz, F. Calegari, **S. Aeschlimann**, M. Chávez Cervantes, C. Cacho, R. T. Chapman, E. Springate, S. Link, U. Starke, C. R. Ast, and A. Cavalleri, “*Tracking primary thermalization events in graphene with photoemission at extreme time scales*”, *Phys. Rev. Lett.*, vol. 115, p. 086803, Aug 2015 [1]

I took part at trARPES experiments and analyzed the experimental data.

2. **S. Aeschlimann**, R. Krause, M. Chávez-Cervantes, H. Bromberger, R. Jago, E. Malic, A. Al-Temimy, C. Coletti, A. Cavalleri, and I. Gierz, “*Ultrafast momentum imaging of pseudospin-flip excitations in graphene*”, *Phys. Rev. B*, vol. 96, p. 020301, Jul 2017 [2]

I performed trARPES experiments and analyzed the experimental data. I wrote the first draft of the manuscript.

Manuscripts in Preparation

1. **S. Aeschlimann**, M. Chavez-Cervantes, R. Krause, A. Rossi, S. Forti, F. Fabbri, C. Coletti, and I. Gierz, “*Direct evidence for ultrafast charge separation in epitaxial WS₂/graphene heterostructure*”, submitted, 2019 [3]

I performed trARPES experiments and took part at the analysis of the experimental data and writing of the manuscript.

2. **S. Aeschlimann**, M. Chavez-Cervantes, R. Krause, S. Forti, F. Fabbri, K. Hanff, K. Roßnagel, C. Coletti, and I. Gierz, “*Practical Limitations of the Floquet Topological Insulator in Graphene*”, in preparation, 2019

I performed trARPES experiments and analyzed the experimental data.

Other Publications and Projects

Other publications and manuscripts beyond the ones related to the results discussed in the thesis:

1. M. Chávez Cervantes, R. Krause, **S. Aeschlimann**, and I. Gierz, “*Band structure dynamics in indium wires*”, Phys. Rev. B, vol. 97, p. 201401, May 2018 [4]

I took part at the trARPES experiments.

2. **S. Aeschlimann**, A. Topp, M. Bianchi, P. Hofmann, I. Gierz, and C. Ast, “*Influence of Defects on the Bandstructure of Graphene*”, in preparation, 2019

I performed the ARPES experiments and analyzed the experimental data.

Contents

Introduction	1
1 Graphene Properties and Fabrication	9
1.1 Equilibrium Properties	9
1.1.1 Dirac Fermions	10
1.1.2 Pseudo-Spin of Graphene	11
1.2 Dynamical Properties	11
1.2.1 Electron-Electron-Scattering	12
1.2.2 Electron-Phonon Scattering	18
1.2.3 Nonequilibrium Carrier Dynamics in Graphene	19
1.3 Graphene Fabrication	22
2 Experimental Methods	25
2.1 ARPES: Angle-Resolved Photoemission Spectroscopy	25
2.1.1 Photoemission from Graphene	26
2.2 TrARPES: Time- and Angle-Resolved Photoemission Spectroscopy	27
2.2.1 Introduction	27
2.2.2 Experimental setup	28
2.2.3 Space Charge Effects	35
2.2.4 Laser-Assisted Photoelectric Effect (LAPE)	36
2.3 Sample Growth and Characterization	38
2.3.1 Epitaxial Graphene	38
2.3.2 WS ₂ /Graphene Heterostructure	40
2.3.3 Bulk WSe ₂	41

3	Tracking Primary Thermalization Events in Graphene at Extreme Time Scales	43
3.1	Introduction	43
3.2	Experiment	46
3.3	Discussion	49
4	Ultrafast Momentum Imaging of Pseudospin-Flip Excitations in Graphene	53
4.1	Introduction	53
4.2	Experiment	54
4.3	Microscopic Simulations	59
4.4	Discussion	60
5	Ultrafast Charge Transfer in Epitaxial WS₂/Graphene Heterostructure	63
5.1	Introduction	63
5.2	Experiment	65
5.3	Discussion	69
6	Practical Limitations of Floquet Topological Insulators	75
6.1	Introduction	75
6.2	Experiment	77
6.3	Discussion	83
	Conclusions and Outlook	84
	Appendices	93
A	Details on Electronic Properties of Graphene	95
A.1	Tight-Binding Model of Graphene	95
A.2	Low Energy Theory and Dirac Hamiltonian	96
A.2.1	2D Dirac Equation and its Solutions	97
A.2.2	2D Dirac Equation in 2nd Quantization	97
A.2.3	Diagonalizing the Dirac Hamiltonian within the Chiral Basis	98
A.3	Topology of Graphene and other 2D Dirac Systems	99
A.3.1	Details on Pseudo-Spin of Graphene	100
A.3.2	Berry-Phase and Berry Curvature	102
A.3.3	Massless Dirac System	104
A.3.4	Honeycomb Lattice with Broken Inversion Symmetry	106
A.3.5	Honeycomb Lattice with Broken Time-Reversal Symmetry	109
A.4	Renormalized Electronic Spectrum	112
A.5	Interband Excitation in Graphene	115

B	Theoretical Background of Photoemission Spectroscopy	117
B.1	Introduction	117
B.2	Theoretical Models	119
B.2.1	Three-Step Model	121
B.2.2	Photoemission from Graphene within the Three-Step Model	123
B.2.3	One-Step Model and Photoemission Theories Beyond the Sudden Approximation	125
C	Additional Results from Microscopic Simulations	127
D	Floquet Theory	131
	Bibliography	135
	Acknowledgements	153

Graphene, a purely two-dimensional material, is a single atomic layer of graphitic carbon. Since its first isolation in 2004 [5, 6], the material has attracted intense attention for its extraordinary properties and served as an exceptionally fertile ground for advancing frontiers of condensed matter physics. A single graphene layer is the strongest material ever discovered, with an ultimate tensile strength of 130GPa [7], while being the most stretchable crystal at the same time [8]. It is the most impermeable material, even to He [8], it has the highest intrinsic electron mobility of up to $2.5 \cdot 10^5 \text{cm}^2 \text{V}^{-1} \text{s}^{-1}$ [7], about 100 times that of silicon. It possesses a record thermal conductivity of more than 3000WmK^{-1} , 10 times as high as copper [8], a Young's modulus of 1TPa [9] and the capability of sustaining high current densities [7].

Graphene is just one of many possible two-dimensional (2D) crystals that are studied nowadays [6]. There are hundreds of layered materials that retain their stability down to monolayers, and whose properties are complementary to those of graphene. Monolayers of hexagonal boron-nitride and of transition metal dichalcogenides (TMDCs) are semiconductors with direct band gaps that span several electron-volts while offering similar practicalities such as transparency, mechanical flexibility and easy processing. A promising approach is to combine these properties and create multifunctional, high-performance materials by building stacked heterostructures consisting of graphene and other 2D materials [6, 10, 11], giving rise to a whole new field of nanoscale engineering.

2D Material-Based Technology

Graphene's properties make it an attractive material for a wide range of technological applications and tremendous effort has been made by public research and various companies with industrial focus (e.g. Samsung, IBM, Nokia) to work towards commercialization of

graphene-based technology [12]. 15 years past the pioneering work on graphene by Geim and Novoselov [5,6], only very few products that involve graphene technology are available off the shelf: e.g. the tennis racket by Head, the battery strap by Vorbeck, the oil drilling mud by Nanochem and the phone touch screen by Samsung [12]. Nevertheless, as the extraordinary growth in the number of organizations developing graphene applications and the increasing number of patents filed make clear, these products are likely to represent only the market entry for a new wave of commercial graphene-based applications in the years to come.

The applications are further extended by other 2D materials, which are studied only since a few years with increased effort towards the development of new technology. The diversity of the 2D materials, especially hybrid systems consisting of heterostacks, hold promise for the design of novel devices with so far unknown functionalities.

While development of 2D material-based devices is more mature in some areas, such as flexible electronics and conductive inks, it is still in its infancies in others, such as biomedical and aerospace technologies. Apart from developing methods for high-quality and large-scale production of these materials, there are still many hurdles to be overcome, both by research and development, before many technologies will be able to reach the market. Citing review articles [11, 13–15], some highlights are listed here:

- **Electronics** (from [13]): The main driving force of the electronic industry is the demand for higher performance and lower power consumption. For digital electronics, graphene and other 2D-materials are promising materials providing the option of ultimately thin “channel” transistors and the opportunity for new device concepts. Despite very high switching speed, it is understood that graphene field effect transistors cannot compete with contemporary high-performance transistors based on Silicon. The zero bandgap leads to at most a few tens I_{on}/I_{off} ratios ($I_{on}/I_{off} > 10^4$ needed for future devices) and large I_{off} . Due to the existence of gaps, TMDC-based field effect transistors compare favorably over graphene, with large I_{on}/I_{off} ratios achieved for MoS_2 transistors [16]. In the best-case scenario of ballistic transport, these are predicted to outperform alternative high-performance devices with short delay times of 60fs. However, there are no reported data on high-frequency operation of devices and circuits based on TMDCs as of now.

While graphene is not considered to replace Si in digital electronics in the near future, it is believed to play a more relevant role for analog and radiofrequency applications. Showing the highest electron mobilities and saturation velocities of any transistor channel material so far, it can potentially outperform current high-

frequency electronics dominated by III-V and SiGa-based semiconductor transistors (reported f_{max} in the range of 1-2THz) and extend frequencies far into the Terahertz regime.

- **Flexible Electronics** (from [14]): The use of graphene as a transparent electrode has already been demonstrated in several flexible devices, including touch screen sensors [17], organic light-emitting diodes [18] and organic photovoltaic devices [19]. The possible applications are humongous, ranging from flexible displays, wearable electronics to transparent heaters and flexible photovoltaic panels.
- **Spintronics** (from [15]): Due to its predicted long spin lifetime ($\sim 1\mu s$), graphene is of particular interest for new forms of information storage and logic devices utilizing the spin degree of freedom. However, the origin of spin relaxation in graphene, observed to be much shorter than expected (up to a few nanoseconds), is still an open question, and there are no “serious” devices built yet.
- **Optoelectronics** (from [11]): Graphene and other 2D materials such as TMDCs serve as intriguing building blocks for optoelectronic applications. Numerous prototype optoelectronic devices such as photovoltaic modules [20,21], optical modulators [22], plasmonic devices [23] and ultrafast lasers [24] have already been demonstrated. A strong focus is laid on graphene-based photodetectors. The absence of a band gap allows universal light absorption over a uniquely wide spectrum, from ultraviolet, visible, near-infrared, mid-infrared, far-infrared to terahertz spectral regimes, unmatched by any other material. Furthermore, ultrafast carrier dynamics and the high carrier mobility allows ultrafast conversion of photons or plasmons to electrical currents or voltages. This enables application in areas such as broadband high-speed photodetection for optical communications, ultrasensitive detection (remote sensing, biomedical imaging, optical communications and gas sensing), mid-infrared detection (biosensing, security and thermal imaging), and THz detection.

Probing Transient Carrier Dynamics: State of the Art and Adressed Open Questions

The possible applications of graphene and other 2D materials seem endless. As already emphasized, many techniques are still in the research and development phase, and working towards a commercial use of graphene still requires effort both from a fundamental and technical point of view.

This work aims at setting up basic conceptions for the development of new technology in the broad field of optoelectronics and to some degree of spintronics. For the design of novel 2D material-based device structures in these areas it is of crucial importance to have an accurate understanding of the dynamical properties of these materials far away from equilibrium. The responsible electron processes are taking place on ultrafast timescales, partly on a sub 10 femtosecond timescale. Ultrafast carrier scattering processes define device performances - being able to manipulate and control these mechanisms allows building more efficient designs.

The development of ultrashort lasers opened the route towards experimental techniques which are able to observe carrier dynamics on timescales ranging from hundreds of femtoseconds down to the attosecond regime. These experiments are based on pump-probe schemes, where two laserpulses with variable time delay impinge on a material of interest: A first pulse, the pump, perturbs the system, usually in the form of redistributing charge carriers to higher energy states, while a second pulse, the probe, tracks the resulting out-of-equilibrium relaxation behavior, revealing information about the underlying dynamical mechanisms.

Employing targeted excitation schemes to pump-probe spectroscopy, allows to study dynamical properties of solids in highly specific non-equilibrium states and even holds promises to transform ultrafast science into a toolset not just of observation, but of precise control over material behavior.

In this work, time- and angle-resolved photoemission spectroscopy (trARPES) is used, a method which combines the ability to observe ultrafast carrier dynamics in real-time, given by pump-probe spectroscopy, with the powerful tool of probing the spectral information of electrons in terms of their initial state energy and momentum, given by photoemission spectroscopy.

Several trARPES experiments were set out to investigate fundamental scattering processes in graphene, with particular focus on the out-of-equilibrium behaviour of a photoexcited electronic system, while one experiment investigated the possibility to induce a phase-transition in graphene by light. A further study investigated the functionality of a TMDC/graphene heterostructure.

Carrier Relaxation in Photoexcited Graphene

Prior studies of ultrafast carrier dynamics in graphene [25–47], mainly employing optical pump-probe spectroscopy and time-resolved photoemission spectroscopy, already established quite a firm picture of the cooling dynamics of thermalized hot electronic

distributions. There is general consent that hot electrons mainly cool by optical phonon emission and to a weaker extent by acoustic phonon emission until equilibration between the electron system and the cold lattice is reached.

In a few investigations, an electronic quasi-equilibrium was observed under certain conditions, where two separately thermalized electron baths for conduction and valence band were found [29, 31, 35, 37]. Interpreted as weak forms of population inversion, these transient quasi-equilibrium states were assumed to decay via optical phonon emission in combination with electron-electron scattering processes.

While the cooling mechanisms were well-understood, the processes that lead to a (quasi)-equilibrium of electrons in the form of one or two Fermi-Dirac distributions, have not been observed to that date, mainly due to a lack of temporal resolution. Some open questions were:

- The occurrence and importance of so-called *Auger-processes* remained unclear. *Auger-processes* have particular technological relevance for optoelectronic applications such as photodetectors and solar cells, due to their ability to manipulate the occupation and kinetic energy within individual bands.
- The angular dependence of two-electron-scattering was debated. Theoretical models led to contradicting results, while some theories predicted enhanced scattering along radial lines through the Dirac point, others predicted a complete prevention of such processes. [48–52].
- The influence of screening on the thermalization dynamics of photoexcited graphene was unknown. This has particular relevance for photoexcited graphene as non-equilibrium electronic distributions can profoundly change dynamical screening properties [51, 53, 54].

In a first study (chapter 3), the primary thermalization dynamics of photoexcited graphene was studied at extreme timescales. The experiments were performed during a beamtime at the ARTEMIS facility at Harwell, UK. Sub 10fs temporal resolution, representing the fastest trARPES study performed on graphene to this day, allowed the observation of nonthermal intraband carrier distributions and their evolution in time towards a Fermi-Dirac distribution. Signatures for *impact ionization* - one particular Auger channel - were found during the first ~ 25 fs after photoexcitation.

A complementary study is given by investigating anisotropic charge excitations in graphene in full two-dimensional momentum space (chapter 4). The experiment revealed an exceeding dominance of collinear scattering over non-collinear scattering. As a result, electrons are very efficiently redistributed along radial lines through the Dirac point, scattering

around the cone happens at a much slower rate. Under the given circumstances of doped graphene samples and strong substrate dielectric screening, this leads to a transient quasi-thermal state with anisotropic temperature.

Photoexcited WS₂/Graphene Heterostructures

One example of the many possible 2D material-heterostructures is given by a stack made up of graphene and monolayer tungsten-disulfide (WS₂). The latter belongs to the family of TMDCs and is a direct-gap semiconductor with a sizable spin splitting of the band structure due to spin-orbit coupling. Such a structure combines the massless Dirac properties and long spin lifetimes of electrons in graphene together with the possibility of spin and valley selective excitation schemes enabled by the spin-polarized bandstructure of WS₂.

Indications for ultrafast charge transfer [55–59] and proximity-induced spin-orbit coupling effects [60–62] make the WS₂/graphene heterostructure a promising candidate for future optoelectronic and optospintronic applications.

For the purpose of investigating the prospects of such devices the relaxation dynamics of a photoexcited epitaxial WS₂/graphene heterostack grown on silicon carbide was studied (chapter 5). With pump pulses resonant to the intralayer exciton of WS₂, a transient charge-transfer state with ~ 1 ps lifetime was found. By employing circularly polarized light, such a charge-transfer state is expected to be spin-polarized opening the route to efficient spin-injection into graphene.

Light-Induced Topological Phase Transition in Graphene

The emerging field of Floquet engineering is a promising route towards the control of bandstructures in solids. The concept is based on driving solid state systems periodically in time in order to change the steady-state behavior of the system and stabilize new topological quantum states that are not present at equilibrium. Within the framework of the Floquet formalism, tailored driving schemes are developed by treating the time-dependent problem in terms of an effective Hamiltonian that hosts stationary quantum states.

In chapter 6, an experiment is described which aims at the realization of one of the most prominent examples of Floquet engineering, given by the so-called *Floquet topological insulator*. In 2009, it was predicted that graphene, a topologically trivial material, undergoes a phase transition to a topological insulator when being subject to strong circularly polarized light [63]. This insulating phase serves as a true realization of the well-known

Haldane model, it is predicted to host one-dimensional metallic edge-states and to give rise to an half-integer quantum Hall effect in the absence of a magnetic field. The experiment reveals difficulties of creating such a *Floquet topological insulator* in graphene and highlights important drawbacks when applying similar predictions from Floquet theory to realistic systems.

CHAPTER 1

Graphene Properties and Fabrication

1.1 Equilibrium Properties

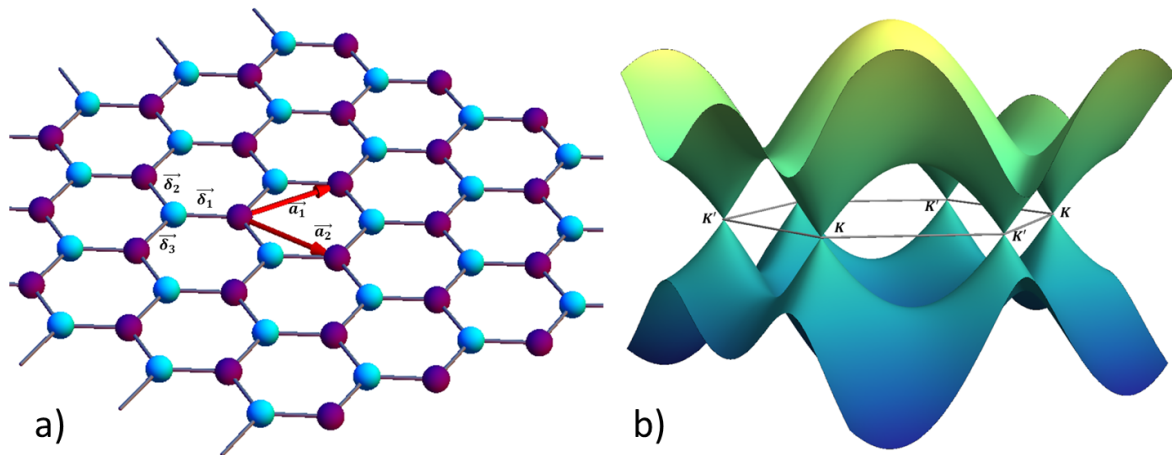


Figure 1.1: a) Crystal structure of graphene: The honeycomb lattice structure made up of carbon atoms consists of two triangular sublattices A and B indicated by two colors. The lattice vectors are \vec{a}_1 and \vec{a}_2 and nearest neighbor vectors $\vec{\delta}_1$, $\vec{\delta}_2$ and $\vec{\delta}_3$ b) Tight-binding bandstructure of graphene and hexagonal Brillouin zone: Conduction and valence band meet at three identical K and K' points on the zone edges.

Many of the striking properties of graphene can be traced back to its electronic structure. A graphene layer is made of carbon atoms arranged in a honeycomb lattice structure (fig. 1.1a). Each atom is covalently bonded to three nearest neighbors by sp^2 -hybridized σ -orbitals, resulting in the high inherent strength of 0.142Nm along carbon bonds. The

tight-binding electronic band structure (shown in fig. 1.1b) is given by a conduction and valence band touching at distinct K and K' points on the Brillouin zone edges. At neutral doping the Fermi level is at the level of the touching points, resulting in a semi-metal with linear band dispersion, no band gap and vanishing density of states. Some further details on the electronic properties of graphene are discussed in appendix A.

1.1.1 Dirac Fermions

In the vicinity of the K and K' points the single-particle Hamiltonian is given by the 2D Dirac equation [64]:

$$h = \hbar v_F \vec{\sigma} \cdot \vec{k}, \quad (1.1)$$

with the Pauli matrix vector $\vec{\sigma} = (\sigma_x, \sigma_y)^T$ and Fermi velocity $v_F \approx 10^6 m/s$, giving rise to the linear eigenstate spectrum $\epsilon_{\nu=\pm 1} = \nu \hbar v_F k$. The low-energy quasi-particles behave like ultra-relativistic massless Dirac fermions (see fig. 1.2), giving rise to high electron mobility, thermal conductivity and to broadband transparency.

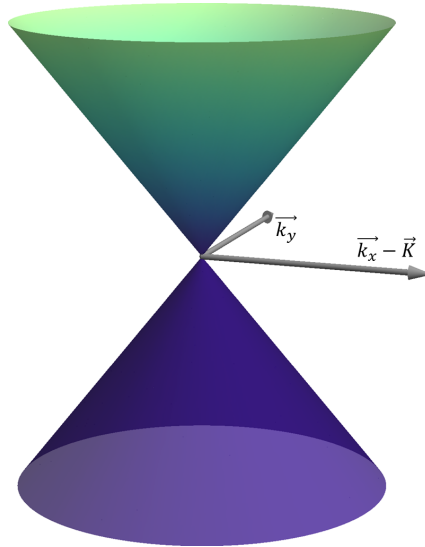


Figure 1.2: Dirac cones at K point: Quasiparticles in graphene behave like massless Dirac fermions.

As discussed in detail in appendix A.3 the touching points at K and K' possess strong rigidity against interactions, lattice defects, and other effects. The persistence of the Dirac points is topologically protected by symmetry. Opening a band gap in graphene requires breaking either the time-reversal or inversion symmetry of the system.

1.1.2 Pseudo-Spin of Graphene

The concept of pseudo-spin can be applied to any two-level system such as the hexagonal lattice system (details on the formal description are given in appendix A.3.1). It is important to note that the pseudo-spin is in no way connected to the actual spin of the electron which is degenerate in graphene. The pseudo-spin defines how the electronic eigenstates are constructed, set up by two sublattice Bloch waves. The in-plane angle defines the phase between the Bloch waves, the out-of-plane angle defines the relative weight between them.

The eigenstates of the tight-binding Hamiltonian of the hexagonal lattice take the form of spinors exhibiting a strict pseudo-spin-momentum locking. For graphene, at equilibrium, all eigenstates carry a pseudo-spin restricted to the x-y-plane. The in-plane pseudo-spin texture of the conduction band is shown in fig. 1.3. The pseudo-spin of the valence band states is opposite to the one of the respective conduction band states, the according pseudo-spin structure of the valence band is therefore obtained by flipping all arrows in fig. 1.3.

Fig. 1.3 indicates the presence of topological defects at the Dirac points at the K and K' points: the pseudo-spin structure exhibits vortices at these points in the Brillouin zone, with anti-clockwise winding at K and clockwise winding at K'. These correspond to reciprocally revoked non-trivial Berry phases of $\pm\pi$ at opposite valleys (details in appendix A.3).

The properties of graphene are profoundly influenced by the nature of the pseudo-spin-structure. The Pseudo-spin causes an angle-dependent photoemission matrix element (sec. 2.1.1) and anisotropic optical interband transition (appendix A.5), while its conservation gives rise to the prevention of backscattering (sec. 1.2.1).

1.2 Dynamical Properties

The tight-binding approximation (discussed in depth in appendix A.1) provides an accurate description of the band structure and incorporates many of the physical properties of graphene. However, for all dynamical properties, i.e. whenever the electronic distribution is brought out of its equilibrium state, in excess of the band dispersion, manybody interactions have a further and decisive influence on how the system evolves in time.

Unambiguously, interactions can have a dramatic influence on solids. They cause a renormalization of band structures and stabilize collective modes such as plasmons and

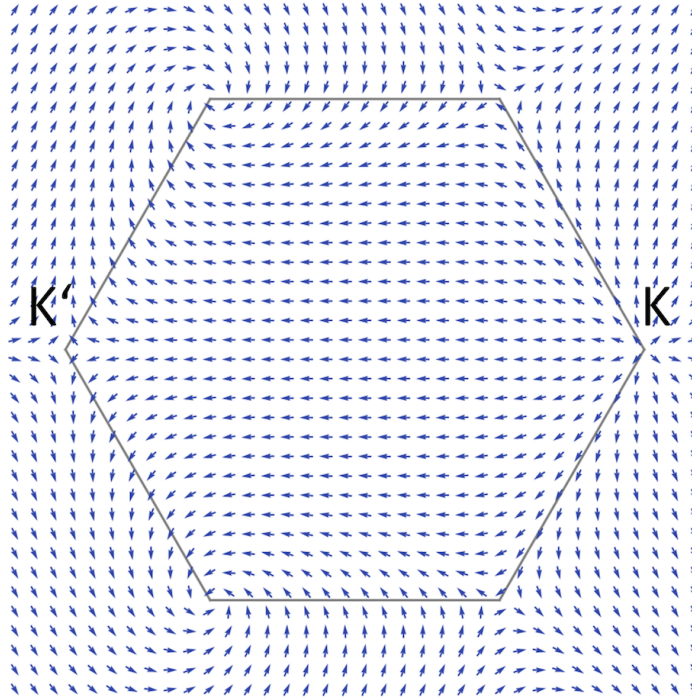


Figure 1.3: Pseudo spin structure of the conduction band of graphene over the full Brillouin zone.

magnons. In materials with particularly strong interactions, they lead to a variety of exotic ground states such as superconductivity and charge ordering. Such materials often possess complex phase diagrams. Concerning the experiments in this work, the most important interactions at work are electron-electron interactions and electron-phonon coupling. Other interactions like spin-orbit coupling, exchange interactions, etc. are of minor importance in graphene or at least under the given circumstances of the experiments.

1.2.1 Electron-Electron-Scattering

Electron-electron scattering happens due to one of the most basic forces in nature - the electro-magnetic interaction or, more specifically, due to Coulomb interaction since electrons in solids move in the non-relativistic limit. While the Coulomb force by itself is a long-range interaction, in most solids the effective 2-particle electron-electron interaction is in fact short-range. The reason is the well-known Thomas-Fermi-screening: Two electrons in a solid interact with each other in a *soup* of mobile charge carriers. The rearrangement of which leads to a reduction of the effective interaction.

In graphene, however, the screening is substantially reduced, owed to two reasons. Firstly, the reduction of dimensions has the consequence that the rearrangement of charges is only happening within a two-dimensional plane while most field lines are going through vac-

uum instead, allowing for a long-range interaction. Secondly the screening is even further reduced in case of graphene at charge neutrality due to the vanishing density of states at the Dirac point.

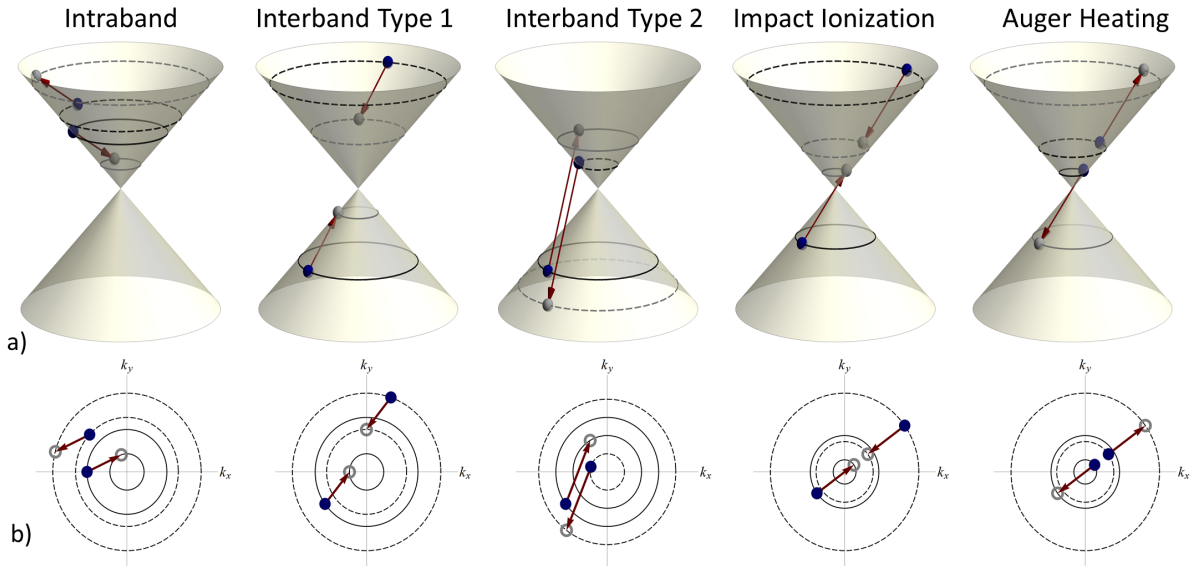


Figure 1.4: All possible types of 2-particle electron-electron scattering processes in graphene. a) Scattering events on the Dirac cones of graphene b) “Top-view” of the electron transitions in the q_x - q_y -plane. Energy-conservation forces scattering of electrons between equipotential circles. In case of Auger-processes (impact ionization and Auger heating) momentum conservation only allows for collinear scattering, while all other type of scattering events are happening in all directions.

An interpretation of the coupling strength of the Coulomb interaction is given by the fine-structure constant α . While in vacuum it has a value of $\alpha = \frac{e^2}{4\pi\epsilon_0 c_0} \approx 1/137$, in graphene the respective coupling constant of the bare Coulomb interaction can reach much larger values $\alpha_G = \frac{e^2}{4\pi\epsilon_0\epsilon_s v_F} \approx 2.2/\epsilon_s$, where ϵ_s is the effective dielectric constant in the presence of a substrate. The possibility of achieving a strong-coupling regime led to several attempts of finding exciton condensation or a stoner instability in graphene both prompting the opening of a gap in the band spectrum [65, 66]. To date, none of which has been found, nonetheless, the vast importance of electron-electron interaction in graphene is not put into question.

The special property of graphene being described by the Dirac Hamiltonian in the low-energy limit leads to a peculiar situation of the electron-electron interaction. The quasi-particles of graphene act like massless ultra-relativistic particles at a speed $\sim c/300$, while the electro-magnetic interaction propagates at the actual speed of light c making the in-

$$\frac{1}{\tau} = \text{Im} \Sigma(\epsilon_1, \vec{k}_1) = \text{Im} \left[\text{Diagram 1} \right] = \int d\omega d^2\vec{q} \left[\text{Diagram 2} \right]^2 \cdot \delta(\{\epsilon_i\}) \delta(\{\vec{k}_i\})$$

Figure 1.5: Electron-electron-scattering in the lowest order of the Coulomb interaction: The scattering rate takes the form of Fermi's golden rule by cutting the self-energy diagrams into parts as described in [67]

interaction still instantaneous as in nearly every condensed matter system. This makes the theory of graphene similar but at the same time very different from Quantum Electro Dynamics (QED).

Some aspects of electron-electron scattering and the effects of the Dirac nature of the electrons shall be discussed here. In fig. 1.4 all possible types of two-particle electron-electron scattering processes that can take place in graphene are shown. These scattering events are responsible for the renormalization of the bandstructure, i.e. the band spectrum observed with ARPES, and the relaxation processes of photoexcited graphene in pump-probe experiments, e.g. in trARPES. The scattering events differ from one-another by the initial and final states of the two scattering electrons being in the upper ($\nu = +1$) or lower Dirac cone ($\nu = -1$).

To get some insight into the physics of the scattering processes it is instructive to take a look at the transition rate of two-electron scattering. In lowest order, the scattering rate is given by the imaginary part of the first order self-energy diagram shown in fig. 1.5. According to the optical theorem, the transition rate can formally be evaluated in the form of Fermi's-golden rule by *cutting* the diagram into halves [67]. The scattering rate of an initial state (ϵ_1, \vec{k}_1) then reads:

$$\begin{aligned}
 \left(\frac{1}{\tau}\right)_{(\epsilon_1, \vec{k}_1)} &= \frac{2\pi}{\hbar} \int d\omega d\epsilon_2 d\epsilon_2' d^2\vec{q} d^2\vec{k}_2 d^2\vec{k}_2' \theta_{1,1'} \theta_{2,2'} V_0^2(q) \tilde{\mathcal{A}}(\epsilon_1, \vec{k}_1) \tilde{\mathcal{A}}(\epsilon_2, \vec{k}_2) \tilde{\mathcal{A}}(\epsilon_2', \vec{k}_2') \\
 &\quad \times \underbrace{\delta(\epsilon_1 + \epsilon_2 - \epsilon_1' - \epsilon_2')}_{\text{energy conservation}} \underbrace{\delta^2(\vec{k}_1 + \vec{k}_2 - \vec{k}_1' - \vec{k}_2')}_{\text{momentum conservation}} \\
 &\quad \times \left[\underbrace{f_1 f_2 (1 - f_1') (1 - f_2')}_{\text{outscattering}} - \underbrace{(1 - f_1) (1 - f_2) f_1' f_2'}_{\text{inscattering}} \right]
 \end{aligned} \tag{1.2}$$

with the electronic distribution functions $f_n = f(\epsilon_n)$, the bare Coulomb propagator $V_0(q) = \frac{e^2}{4\pi\epsilon_0\epsilon_s} \frac{2\pi}{q} = 2\pi\alpha_G v_F \frac{1}{q}$, the spectral functions $\tilde{\mathcal{A}}(\epsilon, \vec{k}) = 2\pi\delta(\epsilon - \nu v_F k)$ ensuring on shell condition (see appendix A.2.3) and the θ -factors:

$$\theta_{1,1'} = \frac{1}{2}(1 + \nu_1 \nu_1' \hat{k}_1 \hat{k}_1') = \frac{1}{2}(1 + \nu_1 \nu_1' \cos(\phi_1 - \phi_1')) \tag{1.3}$$

These *Dirac factors* are a consequence of the pseudo-spin texture of the Dirac quasi-particles, they arise due to projecting initial onto final spinor states. Since the Coulomb interaction keeps the pseudo-spin unchanged, backscattering is prevented ($\theta_{1,1'} = 0$ in case of $\nu_1 \hat{k}_1' = -\nu_1 \hat{k}_1$), giving rise to peculiar effects such as Klein-tunneling [68].

The δ -functions ensure energy and momentum conservation of the two scattering electrons. Fig. 1.4 illustrates how the two conservation laws are fulfilled for the different kinds of two-electron scattering. Energy-conservation forces the initial and final states onto constant-energy levels forming “circles” on the cones. Panel b shows a top view of the circles within the q_x - q_y plane, where the radius of the circles are set by the energy of the initial and final states. Possible processes are given by scattering of one electron from its initial circle to its final circle by a momentum transfer \vec{q} , provided that a second electron can transfer between its initial and final state circle with the opposite momentum transfer $-\vec{q}$ at the same time.

Intraband and Interband Scattering

In case of intraband scattering ($\nu_1 = \nu_2 = \nu_1' = \nu_2'$) and interband scattering (type 1: $\nu_1 = \nu_1' = -\nu_2 = -\nu_2'$, type 2: $\nu_1 = -\nu_1' = -\nu_2 = \nu_2'$) the conditions for energy and momentum conservation can be fulfilled in arbitrary directions, meaning that scattering can happen from any in-plane azimuthal angle of the initial k-vector to other angles. E.g. in the given example of intraband scattering the lower energy state electron can reach any point of its final energy state circle since there will always be a possible respective

transfer of the other electron from its initial to its final energy state circle with the exact opposite momentum transfer.

Auger Scattering

The situation is very different in the case of Auger-processes. These represent all scattering transitions where only one electron jumps to another cone while its scattering partner stays within its initial cone. In contrast to intraband and interband scattering, Auger scattering events can change the respective number of electrons within the conduction and valence band. The two possible Auger processes are impact ionization (the valence band is ionized) and Auger heating also known as Auger recombination (the average kinetic energy of electrons in the conduction band increases). In both cases, momentum conservation leads to a restriction to collinear scattering, meaning that scattering can only happen along one line in momentum space which crosses through the Dirac point. This can easily be seen in the panel b) of fig. 1.4 for the two Auger-processes: the maximally possible momentum transfer of one electron is equal to the minimally possible momentum transfer of the other, allowing scattering only for this one direction.

Forward Scattering Resonance

Besides representing the only channel for Auger processes, collinear scattering events in graphene are subject to a highly peculiar situation for another reason: two interacting electrons that are moving in the same direction, due to the linear spectrum, also move at the same velocity. In these cases, the collision time becomes infinite leading to a strong enhancement of the collinear scattering amplitude [48] which is even further amplified due to the low dimensionality of the 2D graphene system. The effect is sometimes referred to as forward scattering resonance [69].

In perturbation theory, the forward scattering resonance leads to divergent terms which have to be treated with renormalization group analysis [48] by higher order corrections. The most advanced existing calculations are treating the Coulomb-interaction up to random-phase approximation where the dynamical screening compensates for the diverging Coulomb kernel of forward scattering [51]. At this level of the perturbative expansion series the dynamical screening leads to finite intraband collinear scattering, but prevents Auger-processes from happening at all. It is believed that for correct predictions, theoretical models need to take in account the interplay between dynamical screening and eventual broadening of the spectral function due to many body-body effects beyond RPA (such as 3-particle scattering) [51]. These calculations are very challenging and have not been done up to date. Therefore, in graphene, the importance of Auger-processes or

collinear scattering in general is very unclear and still under debate from a theoretical stand point [52].

Further insight into this open question can be gained through experimental evidence. This has been one of the catalysts of the experiments at the core of the current work, which will be presented in chapters 3 and 4 of this thesis.

Plasmons

Plasmons are coherent collective quantum oscillations of a free electron gas density which arise due to the many-body electron-electron interactions. Formally they appear in the form of resonances in the dynamically screened Coulomb potential $V_{\text{eff}} = V_q/\epsilon(\omega, q)$, where V_q is the bare Coulomb potential and $\epsilon(\omega, q)$ the dynamic dielectric function.

Neutral graphene, where the Fermi surface is reduced to a point in k -space, does not possess plasmons. The linear band structure in combination with the completely filled valence band leads to a particle-hole continuum filling up all the relevant phase space above the “light cone”, and therefore preventing the existence of coherent collective excitations [70].

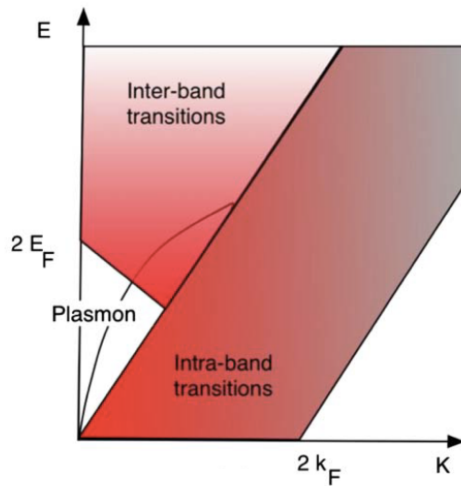


Figure 1.6: Collective plasmon mode and electron-hole continuum in doped graphene, the latter given by intraband and interband electron-hole creation, from [70]

The situation changes for doped graphene, when the chemical potential is moved away from the Dirac point, leading to a Fermi-surface consisting of a circle. A stable plasmon mode with a $\omega_{\text{plasmon}}(q) \propto \sqrt{q}$ dispersion exists up to a value of $\omega \approx \mu$ where it merges into the electron-hole continuum and becomes unstable [71, 72]. The plasmon has been observed experimentally in graphene nanostructures, including a confirmation of the

predicted \sqrt{q} -dispersion [73]. Plasmons in doped graphene are relatively long-lived and appear at lower frequencies than plasmons typically observed in noble metals. Together with the tunability of the plasmons by doping, this makes graphene also potentially interesting for plasmonic technologies [74].

The plasmon leads to a renormalization of the band structure in doped graphene, which has been observed in high-resolution ARPES measurements (detailed in appendix A.4). In highly doped graphene samples the electron-plasmon coupling becomes particularly strong, leading to the creation of plasmaron-sidebands.

A recent theoretical study suggests that the influence of plasmons has been underestimated concerning carrier dynamics of graphene, especially in photoexcited graphene [53,54]. As a pioneering work, the authors propose that the decay of population inversion (see sec. 1.2.3 on previous studies on photoexcited graphene) is partly driven by the process of stimulated emission of plasmons. Simultaneously the plasmon dispersion shows strong deviations from its equilibrium form when electrons are in a quasi-equilibrated state.

1.2.2 Electron-Phonon Scattering

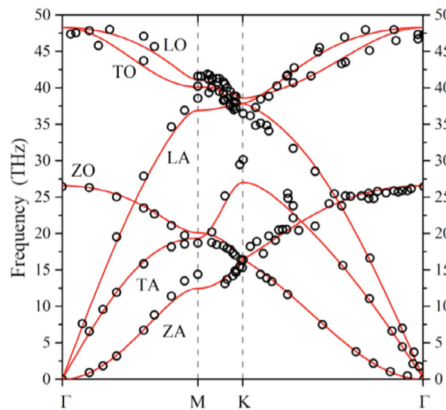


Figure 1.7: Modeled phononic spectrum of graphene (adapted from [75]), superimposed on experimental data points obtained by inelastic x-ray scattering (taken from [76]).

The phononic spectrum of graphene can be seen in fig. 1.7. There is one strongly coupled phonon mode which is the doubly degenerate optical E_{2g} -mode at 48 THz \sim 200meV [77], which splits into the in-plane TO mode and the longitudinal LO mode. Since the submodes are rather flat and the scattering cross section is isotropic, when combining the coupling elements to both submodes [78], the possible scattering processes are quite simple (see fig. 1.8). By emitting (absorbing) a phonon, an electron can reach any point of

the Dirac spectrum 200meV below (above) the original state (fig. 1.8). It is noted that the electron-scattering is not restricted to a single valley, with equal probability scattering from the K to K' valley or vice versa is happening.

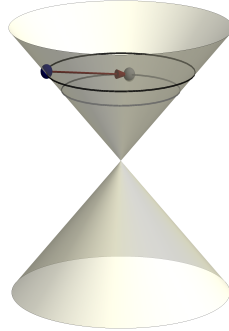


Figure 1.8: Electron Scattering by optical phonon emission with $\hbar\omega_{ph} \approx 200\text{meV}$.

To a much weaker extent, electrons in graphene are also found to scatter with the out-of-plane optical ZO mode (27THz \sim 110meV at Γ) and with acoustic phonons, e.g. in the form of relaxation dynamics in the 0.5-2ps-range of photoexcited graphene [25, 29, 42, 49, 79–83].

1.2.3 Nonequilibrium Carrier Dynamics in Graphene

The special properties of graphene, e.g. semi-metal with zero band gap, linear band-structure, and the Dirac properties of its quasi-particles, make the material a prominent platform for ultrafast carrier dynamics, photonics and optoelectronics. They are already responsible for some unique optical properties of graphene in the linear regime: broadband transparency and universal absorption from the near-infrared to visible [84]. For graphene to play a significant role in ultrafast laser technology, sensor technology or telecommunications, however, it is essential to investigate the femtosecond behavior of photoexcited states far away from equilibrium [31]. Several studies, both experimental and theoretical, dealt with photo-excited graphene [25–47].

Previous Experimental Studies

Early time-resolved studies of photoexcited graphene and graphite have been primarily performed with optical pump probe spectroscopy [25–27, 30]. These studies yielded precise estimates of cooling rates of hot electron distributions. A fast decay-time could be attributed to scattering of electrons with optical phonons and a slow decay-time to scattering with acoustic phonons. Electrons were interpreted to equilibrate to Fermi-Dirac

distributions “instantaneously”, within timescales shorter than the temporal resolution of these experiments. Apart from relaxation dynamics, also pulsed photoluminescence was observed with optical techniques [32–34].

Multiple time-resolved photoemission studies investigated photoexcited graphene with the first one performed in 2012 [85]: in contrast to optical techniques, photoemission directly probes the electronic distributions instead of measuring transitions. These experiments mostly confirmed the interpretations and timescales obtained from previous studies [35, 42–44, 85]. In [42], the direct coupling of electrons to acoustic phonons was found to occur due to supercollision processes (disorder-assisted electron-phonon scattering) as predicted in [81].

Similar cooling dynamics has been observed with trARPES on graphite [46, 47], where also a fast decay-time could be attributed to optical phonon emission. A slow decay time could be traced back due to the anharmonic coupling of the optical phonon to acoustic phonons. Supercollisions are found to be absent in highly ordered pyrolytic graphite due to lower defect concentrations than in epitaxial graphene [47].

By applying pump-lasers in the mid-infrared spectral range in resonance with the optical phonon mode in bilayer graphene, anomalous cooling rates have been found [38, 40], suggesting enhanced electron-phonon coupling due to coherent phonon excitation.

The highest temporal resolution (10-30fs) of pump-probe experiments in photoexcited graphene and graphite so far were achieved with optical techniques in [28, 29, 86]. In [28, 29] it was found that electrons relax to a transient quasi-equilibrium with two separate electron and hole distributions within the conduction and valence band. Such a state was also observed in [31] and in trARPES studies [35, 37], all with temporal resolutions of ~ 40 fs.

Despite sub 14fs temporal resolution in [86], no signature for separate electron and hole distributions were monitored. However, indications for carrier multiplication - generation of multiple electron-hole pairs per absorbed photon - were observed, which was found in a further study by applying multi-color probing at 200fs resolution [87].

Microscopic Picture of Relaxation Dynamics in Photoexcited Graphene

In combination with theoretical calculations and simulations, these experiments led to the following conception of the relaxation dynamics of ultrafast photoexcited graphene (see fig. 1.9): in case of pump photon energies exceeding twice the doping level, interband excitation alters the thermodynamic equilibrium of electronic distributions by creating a big number of electron-hole pairs (fig. 1.9b) which leads to a series of temporally overlap-

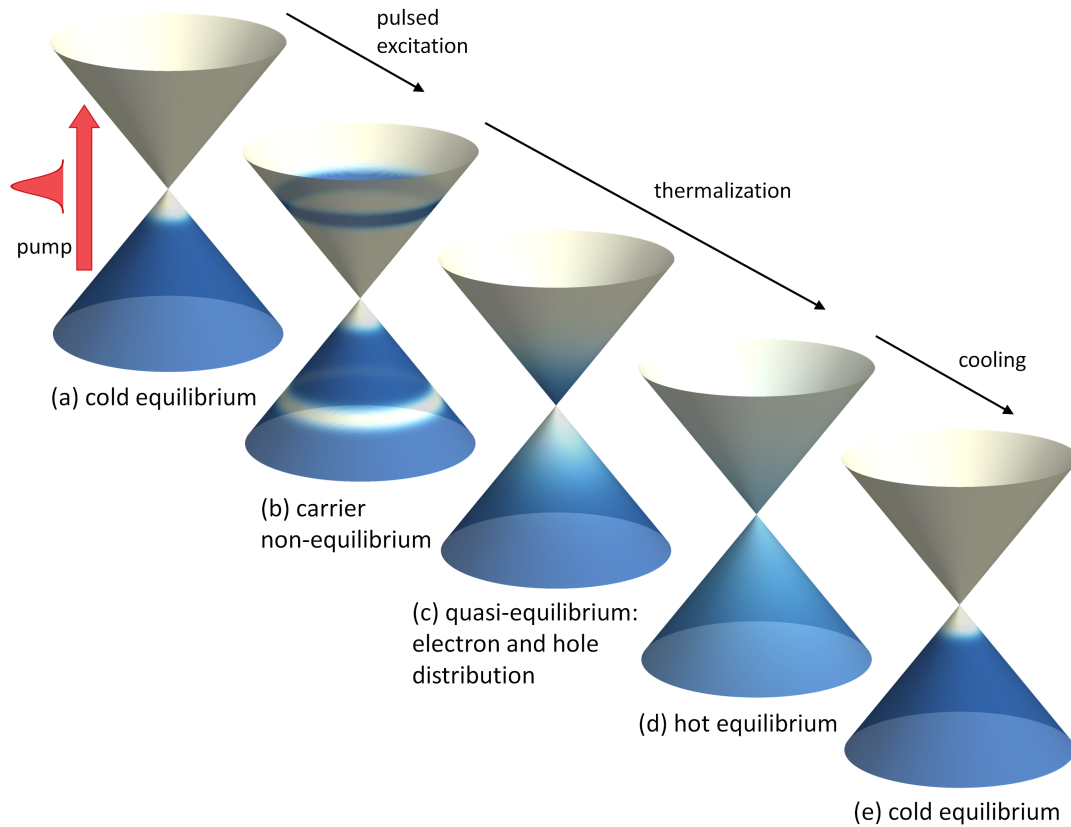


Figure 1.9: Sketch of relaxation dynamics in photoexcited graphene adapted from [53]

ping rapid processes. Electron-electron and electron-phonon-scattering with the strongly coupled optical phonon-mode lead to thermalization towards a hot electronic Fermi-Dirac distribution (fig. 1.9d). On longer time scales, the hot electron system equilibrates with the cold lattice via coupling to optical and acoustic phonons (fig. 1.9e). The timescales of the cooling dynamics are well-understood in terms of a three-temperature model which accounts for three individual baths given by the electrons, optical phonons and acoustic phonons [42].

Under certain conditions, which are not entirely clear and presumably depend on a combination of factors including fluence, doping, and presence of band gaps (e.g. in the case of bilayer graphene), the electronic system relaxes to an intermediate quasithermal equilibrium (fig. 1.9c), given by two separate thermalized distributions for valence and conduction band [49, 50]. The observed quasi-thermal states were interpreted as a weak form of population inversion which has attracted interest for the potential application of THz laser amplification. Population inversion has been predicted to occur in graphene due to the Dirac point acting as a bottleneck during the thermalization dynamics of photoexcited carriers [31, 88].

Full thermalization of electrons, given by the decay of the accumulated electrons at the bottom of the conduction band, is believed to occur through electron-phonon scattering and *Auger recombination*¹ [31, 50].

Prior experimental studies have focused solely on the relaxation dynamics of the transient thermal or quasi-thermal state. Despite their intention of studying the mechanism that leads to (quasi)-thermal equilibrium, they were unable to resolve the responsible scattering processes themselves, mostly due to lack of temporal resolution or limited spectral probing. This led to speculations or educated guesses, e.g. the importance of Auger-scattering was unclear and debated. The experiment in chapter 3 and 4 are dedicated to the thermalization dynamics prior to establishing (quasi)-thermal equilibrium. Both experiments proved the key role of Auger scattering and other collinear electron-electron scattering events during the early thermalization dynamics. Moreover, in the experiment described in chapter 4 the existence of another quasi-thermal state was observed, one of angle-dependent temperature.

1.3 Graphene Fabrication

The first synthesized graphene was exfoliated from highly oriented pyrolytic graphite (HOPG) [5]. To this day, exfoliated graphene are still the highest quality graphene samples available, exhibiting the lowest defect concentrations and highest electron mobilities. Liquid exfoliation is one method towards high-volume production of high-quality graphene [89]. However, the small size of exfoliated flakes is unpractical for many technical purposes.

The industrially most relevant manufacturing method of producing large-area graphene films is currently given by chemical vapor deposition (CVD) on metallic substrates [90], from which graphene-sheets can be transferred onto a variety of substrates. These films usually suffer from polycrystalline structure leading to grain boundaries between single-crystalline domains, which degrades the conductive properties of the sheets. It remains one of the biggest challenges for graphene applications to grow single-crystalline large-area graphene and optimize the transfer to other substrates.

An alternative technique to grow large-scale homogeneous graphene is epitaxial growth on silicon carbide (SiC). It has several advantages, including the possibility of an easy implementation of large-scale manufacturing in existing industrial production lines. SiC serves as an ideal substrate for electronic applications being a wide band-gap semiconductor with a polytype-dependent gap in the range of 3eV. The quality of epitaxial graphene,

¹see sec. 1.2.1 for details on Auger recombination and other electron-electron-scattering channels.

characterized e.g. in terms of electron mobility, suffers from defects which are created during the essential step for the growth given by an annealing procedure. The biggest drawback of epitaxial graphene is presumably the high costs of SiC in comparison to Si [13].

CHAPTER 2

Experimental Methods

2.1 ARPES: Angle-Resolved Photoemission Spectroscopy

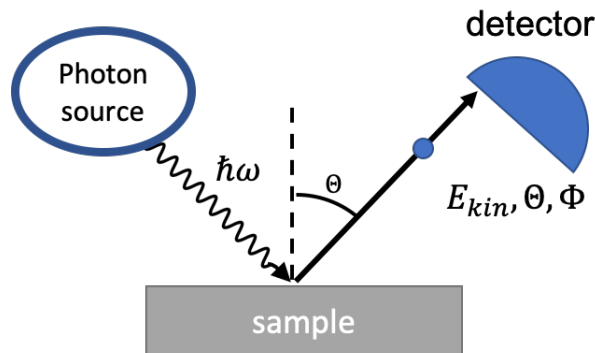


Figure 2.1: Scheme of a modern photoemission spectroscopy setup: a light source produces light in the UV to X-Ray spectral range to emit electrons from a sample. The photoelectrons are detected according to their kinetic energy and their emission angles.

Angle-resolved photoemission spectroscopy (ARPES) was developed for the study of valence electrons, i.e. delocalized electron states over the whole crystal which exhibit a strong energy-momentum dispersion. The method is based on the photoelectric effect: By applying highly monochromatic light radiation in the UV or X-Ray spectral range onto solids, the absorption of photons suffices for electrons to overcome the work function and escape the material (fig. 2.1). By detecting the kinetic energy of the electron and the angle of emission, the in-plane momentum in its initial state can be found by the simple relation

$$k_{\parallel} = \frac{1}{\hbar} \sqrt{2mE_{kin}} \cdot \sin(\theta). \quad (2.1)$$

Within the so-called sudden approximation the photocurrent, representing the rate of electrons leaving the solid with an energy E_{kin} and momentum $\hbar\vec{k}$, is given by:

$$I(E_{kin} = \hbar\omega + \epsilon_i - \phi, \vec{k}) \propto |M_{i \rightarrow f}^k|^2 f(\epsilon_i) \mathcal{A}(\epsilon_i, \vec{k}_i) \quad (2.2)$$

where $M_{i \rightarrow f}^k = \langle \phi_f(\vec{k}) | H_{int} | \phi_i(\vec{k}_i) \rangle$ is the one-electron transition matrix element of the photoemission, which couples the initial single-particle state by photon-absorption onto its final state. $f(\epsilon_i)$ is the electronic distribution function evaluated at the photoelectron's initial state, i.e. the Fermi-function if the system is in the equilibrium state.

The equation relates the photo-current to one of the most fundamental properties of an N-electron system: The photo-current is proportional to the spectral function $\mathcal{A}(\epsilon_i, \vec{k}_i)$. This property of the photoemission process is what makes angle-resolved photoemission spectroscopy the most used technique for measuring band structures in solids. Further details on the theoretical background of photoemission spectroscopy are given in appendix B.

2.1.1 Photoemission from Graphene

Throughout this work, the main purpose of the experiments were to interpret photoemission spectra of graphene. In all experiments described here, a very simplistic 3-step model was sufficient to give accurate results and good agreement with the experimental data. The details on the calculation will be given in appendix B.2.2, the results will be discussed here.

Mapping the one-particle initial state on a plane wave final state leads to the following expression for the photo-current:

$$I(E_{kin}, \vec{k}) \propto \vec{\epsilon}^*(\vec{A}) f(\epsilon_i) \mathcal{A}(\epsilon_i, \vec{k}) \vec{\epsilon}(\vec{A}) \quad (2.3)$$

The spectral function of graphene has (2x2)-matrix form due to its pseudo-spin (sublattice) texture. It is contracted by the polarization-dependent vector:

$$\vec{\epsilon} = \frac{1}{\sqrt{2}} \begin{pmatrix} e^{-i\phi_A} \\ e^{i\phi_A} \end{pmatrix}$$

By separating the spectral function into the parts of the conduction band ($\nu = 1$) and valence band ($\nu = -1$), the expression can be rewritten as:

$$I(E_{kin}, \vec{k}) \propto \sum_{\nu_i=\pm 1} |M_{i,\nu_i \rightarrow f}^k|^2 \tilde{\mathcal{A}}_{\nu_i \nu_i}(\epsilon_i, \vec{k}), \quad (2.4)$$

with the respective absolute square of the one-particle photoemission matrix element

$$|M_{i,\nu_i \rightarrow f}^k|^2 = \left| -ev_F \vec{A} \right|^2 \frac{1}{2} (1 + \nu_i \cos(\phi_k - 2\phi_A)). \quad (2.5)$$

Depending on the polarization of the light, the photoemission matrix element turns part of the bands invisible, an effect which is always present in photoemission spectra of graphene [91, 92, 92, 93] and is known as the *dark corridor* in graphene. Within the photon energies used in this work the plane wave approximation gives accurate results.

For higher photon energies ($\hbar\omega > 40\text{eV}$) deviations in the matrix element have been observed [93]: for one particular polarization ($\vec{E} \perp \Gamma\text{K}$), the dark corridor weakens above 40eV photon energies, it disappears at exactly 52eV, and eventually rotates by 180 at even higher energies. For an accurate description of the photoemission matrix element at high photon energies, a more complex model using time-inverted LEED states as final states is needed [93].

Furthermore, in appendix A.4, the influence of manybody interactions on the spectral function of graphene is discussed by giving a short summary of existing high-resolution ARPES studies.

2.2 TrARPES: Time- and Angle-Resolved Photoemission Spectroscopy

2.2.1 Introduction

In the past decade, ARPES served as one of the most powerful techniques to study the electronic properties of surfaces, interfaces and 2D materials. ARPES offers high-resolution information about electronic band structures at thermal equilibrium and even yields information about manybody effects, since the energy and momentum dependent photocurrent reflects the single-particle spectral function: linewidth-analysis of spectra allows to find lifetimes of holes in the occupied states.

However, the technique fails to track underlying scattering channels of electrons in real time. Moreover, ARPES does not provide any access to dynamical properties of solids away from equilibrium. As most technical applications of solid state materials are based on altering the equilibrium state of electrons in some way, e.g. by a dc or ac electric field

or by photoexcitation, the capabilities of ARPES in the original form are limited in this regard.

Time- and angle-resolved photoemission spectroscopy emerged as a new technique which extends conventional ARPES by ultrafast spectroscopy allowing the simultaneous measurement of the spectral and dynamic information of out-of-equilibrium electronic distributions. Within such a pump-probe scheme, a pump laser pulse of arbitrary wavelength excites the sample, e.g. by electron-hole pair creation or by resonantly driving a designated collective mode, while a subsequent ultraviolet (UV) pulse probes the transient electronic structure at various time delays Δt . With the ultra-high time resolution of femtosecond lasers, trARPES resolves elementary scattering processes in the most direct way possible.

TrARPES is commonly used for measuring the transient population in the unoccupied states of electronic bands upon photoexcitation and track the relaxation of excited carriers due to various decay mechanisms. An alternative and promising route of employing the technique emerges when the pump laser is used to induce and stabilize new transient phases of the material that are not present at equilibrium. TrARPES then measures changes in the occupied electronic band structure, including e.g. metal-to-insulator transitions and melting of charge density waves.

2.2.2 Experimental setup

The newly developed trARPES setup at Hamburg (fig. 2.2) is equipped with a tunable probe source (XUV, 10-45eV), high probe fluence ($\sim 10^9$ ph/s), and a tunable pump source (visible, near-infrared (NIR) and mid-infrared (MIR), 0.4-15 μ m). The system combines the capability of implementing various excitation schemes such as specific electronic interband transitions, intraband excitations and driving collective modes like phonons, with high energy resolution at high photon energy, which is needed for measuring band structures over complete Brillouin zones. The latter is a crucial requirement for measuring the Dirac spectrum of graphene, which is located at the K and K' points at the zone edges.

The Hamburg trARPES laboratory uses a commercial 2-stage Ti:Sapphire laser (*Legend Elite Duo* by *Coherent*) operating at 1kHz repetition rate, generating pulses at wavelength of 790nm with 35fs pulse duration and 12mJ pulse energy. The beam is split into an arm for the probe (2mJ) which is used for high-harmonic generation (the probe beam) and a second arm (10mJ) which is used for the generation of NIR/MIR pump pulses.

2.2. TrARPES: Time- and Angle-Resolved Photoemission Spectroscopy

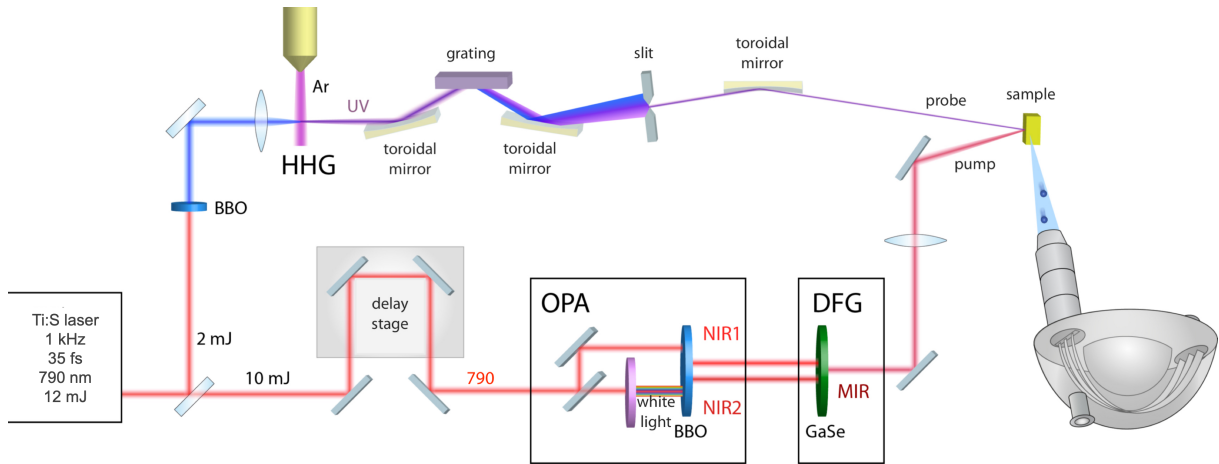


Figure 2.2: Scheme of the trARPES setup at Hamburg featuring tunable pump (NIR/MIR) and probe (UV/XUV) sources at 1kHz repetition rate.



Figure 2.3: XUV beamline at Hamburg consisting of 4 vacuum chambers holding a gasjet, a grating, a slit and 3 toroidal mirrors.

The vacuum system consists of an XUV beamline composed of chambers for high-harmonic generation, a monochromator, a preparation chamber for the growth and annealing of samples, and the main photoemission chamber which operates at a base pressure of $2 \cdot 10^{-10}$ mbar (fig. 2.3). The ARPES chamber is a design by *SPECS* featuring a 6-axis motorized cryostat, with lowest sample temperatures of 10K, and a hemispherical analyzer with CCD camera. The three rotational degrees of freedom provide access to complete Brillouin zones.

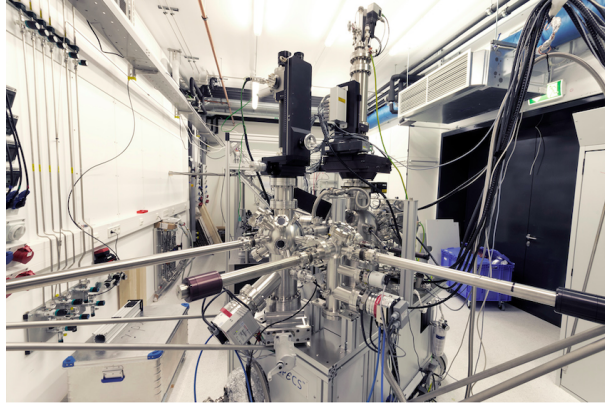


Figure 2.4: ARPES end station consisting of a load lock, preparation chamber and the ARPES main chamber featuring a 6-axis motorized cryostat and a hemispherical analyzer by *SPECS*.

High-Order Harmonic Generation

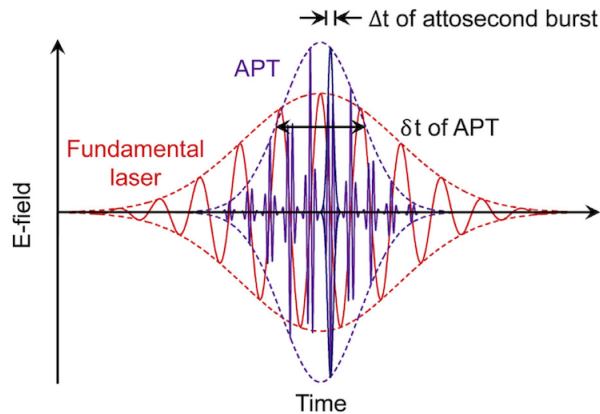


Figure 2.5: Phasematched high-harmonic generation in a multicycle driving laser field (fundamental laser) from [94]. The generated attosecond pulse train (APT) with a temporal envelope δt consists of individual bursts (Δt) which are ejected at the zero-crossing of the driving electric field every half cycle.

The first reports of high-order harmonic generation (HHG) in gases [95, 96] date back to the late 1980s, this unique phenomenon was discovered when ultrashort laser beams were focused onto gas jets. HHG is based on tunneling ionization followed by an acceleration of the electron in the oscillating electric field of the fundamental excitation pulse and a radiative recombination during each optical half-cycle (see fig. 2.5). After decades of substantial improvement, HHG is nowadays used in small research laboratories as a tabletop high-output coherent light source covering a spectrum from the UV to the soft X-ray range, and serves as the only source of attosecond laser pulses.

In the Hamburg XUV beamline, the near-infrared probe beam is focused onto a metal

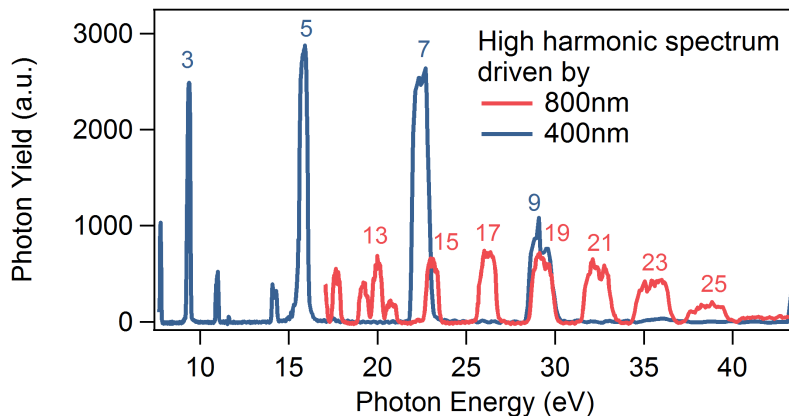


Figure 2.6: High harmonic generation with near-infrared driving laser beam at $\lambda = 800\text{nm}$ versus frequency doubled blue laser beam at $\lambda = 400\text{nm}$. The spectra are obtained by varying the grating angle within a monochromator.

target holding an Argon gas jet for HHG. The strong electric field of the laser beam in the focal point ionizes the Argon atoms. During the recombination of the electrons with the atomic cores every half cycles, attosecond burst pulses of odd harmonics in the UV and XUV spectral range are generated. The temporal envelope of these bursts is a little shorter ($\sim 25\text{-}30\text{fs}$) than the duration of the NIR pulses (see fig. 2.5). Phasematching is achieved by varying the Argon gas output with a piezo controlled valve, ensuring coherent addition of HHG signals from individual atomic emitters [94]. A typical high harmonic spectrum is plotted in fig. 2.6 showing strong photon yield in the range from 20 to 40eV corresponding to the 13th to the 25th harmonic of the fundamental.

The technique has been improved recently by driving the harmonic generation with a blue laser beam, obtained by second harmonic generation from the NIR beam in a beta barium borate (BBO) crystal. While the HHG peaks at lower photon energies around 15eV, the photon yield is considerably higher when driven by the blue laser beam, allowing for faster acquisition rate of photoemission spectra or improved energy resolution for equal signal-to-noise ratios when reducing the XUV spectral width accordingly.

The generated XUV light is monochromatized by a grating based time-preserving monochromator which has been developed by F. Frassetto and L. Poletto from CNR-IFN at Padova, Italy. The monochromator is adapted from the design described in [97,98] and is employed at the ARTEMIS user facility in Harwell, UK. The desired XUV photon energy ($\sim 10\text{-}40\text{eV}$) is selected by rotating a grating and closing the slit thereafter (fig. 2.7). Three gold coated gratings, differing in groove densities and blaze angle, are mounted on a linear translator and can be selected to fulfill particular needs for energy resolution and temporal response depending on the experiment. The monochromator performance under all three

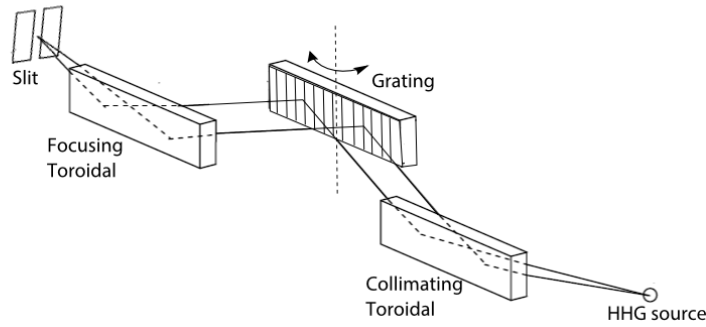


Figure 2.7: Schematics of the monochromator at the Hamburg laboratory consisting of an input toroidal mirror to collimate the light, a grating, and an identical exit toroidal mirror to focus the light onto a slit of adjustable size.

gratings was simulated by the designers and is shown in fig. 2.8. Most experimental results presented in this work have been obtained with the grating featuring a groove density of 120gr/mm at photon energies in between 16 and 26eV. XUV probe pulses therefore possessed spectral bandwidths in the range from 80-180meV and pulse durations of 100-160fs.

Generation of Near-Infrared and Mid-Infrared Pump Pulses

The experiment described in chapter 4 employed NIR pump excitation at 790nm ($\hbar\omega = 1.57\text{eV}$). For this purpose, the direct output beam of the Ti:Sapphire laser was used.

Other experiments required pump beams with different wavelengths. For the generation of NIR (different from 790nm) and MIR pump pulses a commercial optical parametric amplifier (*HE-TOPAS* by *Light Conversion*) and a homebuilt difference frequency generation stage were used.

Optical parametric amplification (OPA) makes use of nonlinear effects triggered by strong laser pulses in certain crystals to generate photons of longer wavelength. In detail, some fraction of the 790nm-beam which feeds the TOPAS is focused onto a sapphire crystal to generate “white light continuum” [99], i.e. broad spectrum of longer wavelength. In the first amplification stage the white light is combined with some other part of the NIR beam at 790nm in a beta barium borate (BBO) crystal. Setting the BBO crystal to a certain angle restricts the phase matching condition of non-linear processes (energy and momentum conservation of photons) to convert two photons (white light + 790nm) into two new photons, called signal and idler photons, both in the NIR range. Two subsequent amplification stages combine the signal beam with the remaining 790nm-light to amplify

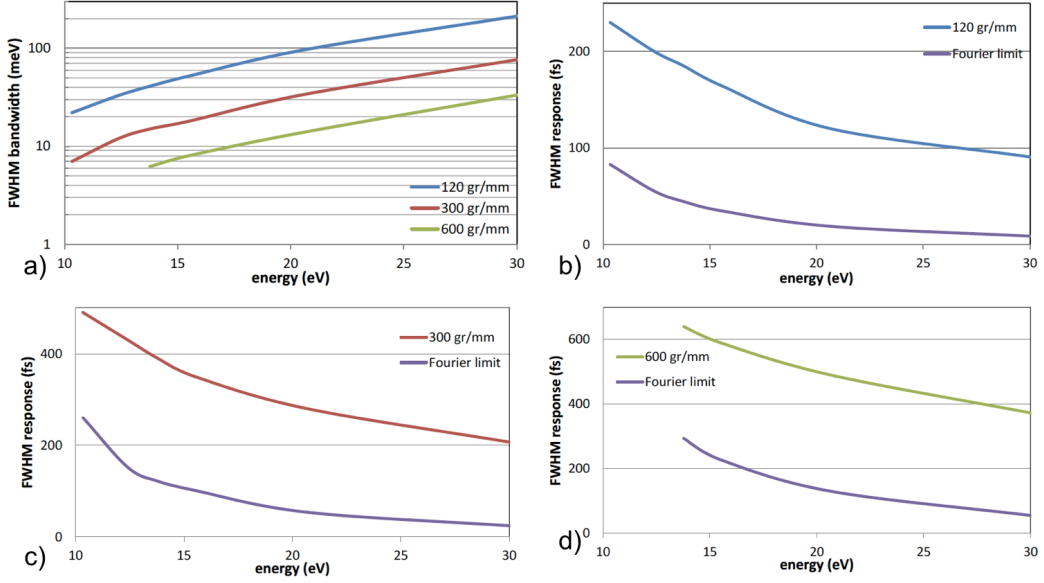


Figure 2.8: Monochromator performance after surpassing a $100\mu\text{m}$ slit assuming a $50\mu\text{m}$ HHG source under three exchangeable gratings: a) Simulated spectral bandwidth as a function of photon-energy. b),c),d): Temporal response of the three gratings compared to the Fourier limit of the corresponding spectral bandwidth.

the signal beam further. Making use of a computer software, crystal angles and delays within the TOPAS can be modified for changing the wavelength of signal and idler beams within the 1160-1600nm range for the signal, and 1600-2600nm for the idler. With an input power of 10mJ, output powers of 4mJ are achieved (signal and idler combined).

For the experiment described in chapter 5, pump pulses in the visible spectrum with $2\text{eV} \hat{=} 620\text{nm}$ photon energy (orange by eye) were used to excite a $\text{WS}_2/\text{graphene}$ heterostructure in resonance to the exciton energy. For this purpose, pump pulses were created by frequency-doubling the OPA signal output beam with 1eV photon energy ($\lambda = 1.25\mu\text{m}$) in a BBO crystal thereafter.

The Hamburg setup is capable of generating mid-infrared pump pulses, for which difference frequency generation (DFG) is used: the homebuilt DFG stage recombines the signal and idler output beams from the TOPAS on a gallium selenide (GaSe) crystal, bought from *Eksma optics*, to generate light with photon energies given by the difference in photon energy between signal and idler. By changing the wavelength of signal and idler, DFG laser beams in the spectral range from 3-12 μm and pulse energies up to 80 μJ can be generated. Fig. 2.9 shows a typical DFG spectrum measured by Fourier-transform infrared spectroscopy.

The experiment described in chapter 6 employed mid-infrared pump pulses at $4.45\mu\text{m}$ for which signal and idler beams at respective wavelengths of $\lambda_{\text{signal}}=1340\text{nm}$ and $\lambda_{\text{idler}}=1920\text{nm}$ were used.

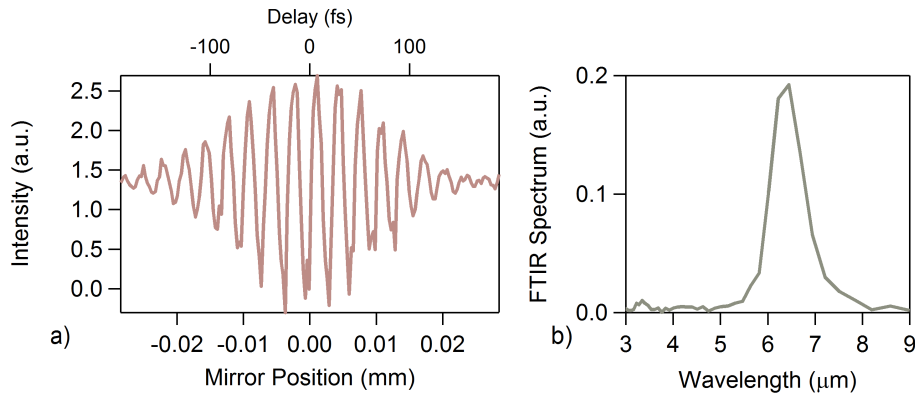


Figure 2.9: Typical mid-infrared pump laser spectrum obtained by Fourier-transform infrared spectroscopy (FTIR): a) Varying photodiode current when moving the mirror position within a Michelson interferometer and b) its Fourier transform representing the pump laser spectrum peaking at a wavelength of $\lambda = 6.3\mu\text{m}$.

Sub 10fs Pulse-Compression at the ARTEMIS facility

The experiment described in chapter 3 was performed at the ARTEMIS user facility at the Rutherford Appleton Laboratory in Harwell, United Kingdom. The materials science end station offers a very similar setup as the Hamburg laboratory. ARTEMIS uses the 2-stage Ti:Sapphire laser (*Red Dragon* by *KMLabs*), operating at the same repetition rate of 1kHz, generating pulses at 790nm with 30fs pulse durations.

One major variation is given by a differently designed time-preserving grating-based monochromator where grooves are oriented horizontally in contrast to the Hamburg ver-

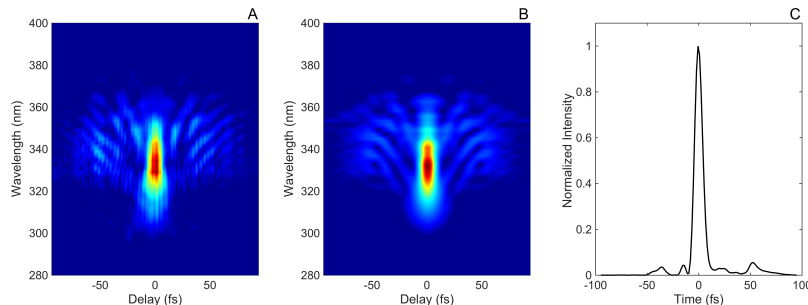


Figure 2.10: Second-harmonic FROG reconstruction of the compressed pulses. A Second-harmonic FROG trace acquired as a function of delay. B Reconstructed second-harmonic FROG trace. C Reconstructed pulse intensity profile. The retrieved pulse duration is 8.3fs.

sion which uses vertical orientation [98] (see fig. 2.7). Selecting a harmonic of choice is achieved by rotating the grating by the normal axis instead [98]. While the Hamburg design is optimized for high energy resolution (reaching $< 10\text{meV}$ XUV bandwidths with the gratings featuring 600gr/mm and 300gr/mm as seen in fig. 2.8), the ARTEMIS design is optimized for high temporal resolution facilitating sub 10fs temporal responses.

For the purpose of probing carrier dynamics in photoexcited graphene at extreme timescales, $\leq 10\text{fs}$ pump and probe pulses were generated by temporal pulse compression with self-phase modulation. 1mJ of energy was compressed down to 8fs with a hollow-core fiber filled with 1.4bar of neon operated with a pressure gradient and followed by 10 chirped mirrors. Pulse compression resulted in a slight blue shift of the spectrum to a central wavelength of 670nm (1.85eV). $400\mu\text{J}$ of energy were used for high harmonics generation (HHG) in argon, $20\text{mJ}/\text{cm}^2$ were used to excite the sample. Due to the longer path in air two additional chirped mirrors were added to the pump path resulting in a pump pulse duration of 10fs. All pulse durations and pulse spectra were measured using second-harmonic frequency-resolved optical gating (FROG) (see fig. 2.10).

Out of the broad HHG spectrum, the harmonic at $\hbar\omega_{\text{probe}} = 30\text{eV}$ was selected by using two different gratings, offering slightly different time or energy resolution [98]. Both pump and probe pulses were s-polarized, with the electric field vector in the plane of the graphene sample perpendicular to the ΓK direction

2.2.3 Space Charge Effects

Photoemission spectroscopy is subject to space charge effects limiting experimental resolution and resulting in systematic measurement errors if not accounted for correctly. The experiments in this work were performed as such to reduce space charge effects to an unavoidable minimum.

Probe Induced Space Charge

The problem arises due to the generation of a cloud of photoelectrons by the UV/XUV pulse that expands due to Coulomb repulsion, leading to smearing of the energy and momentum information of photoelectrons [100–103]. In order to minimize the effects, the probe pulse energy should be reduced such that there is approximately only one photoelectron per pulse.

Here, the adjustable monochromator slit was closed to a size where probe-induced space charge effects were reduced to non-observable magnitudes. At these settings, the XUV pulse energy sufficed for signal-to-noise ratios allowing for high quality photoemission spectra within reasonable acquisition times.

Pump Induced Space Charge

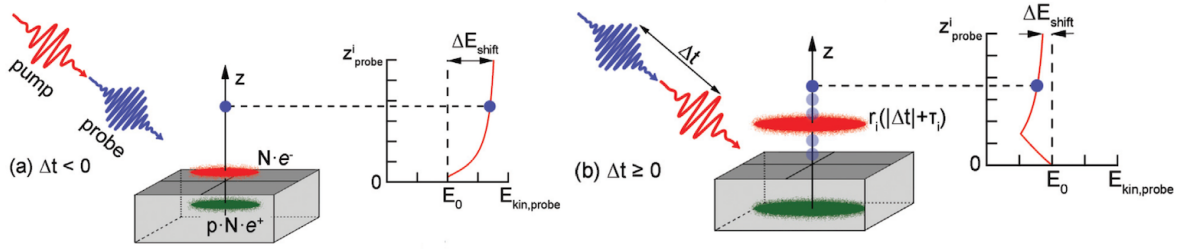


Figure 2.11: Schematic illustration of pump-induced space charge effects on ARPES spectra from [104]: (a) At negative pump-probe delays the spectrum is shifted to higher kinetic energies. (b) At positive delays the probe-induced photoelectrons pass through the pump-induced electron cloud and the spectrum shifts to lower kinetic energies.

Pump induced space charge effects are more complex and have not been studied as systematically yet. They result from the Coulomb repulsion between two separate photoelectron clouds ejected by the UV/XUV probe pulse and the pump pulse [104–106]. In trARPES experiments, pump photon energies are usually smaller than the work function of the sample, thus, pump-induced photoelectrons are a priori unexpected. However, due to the typically required high pump fluences, a space charge cloud of low energetic photoelectrons is created by multiphoton absorption.

Depending on the pump-probe delay, the extensive and relatively slowly moving pump induced electron cloud is known to decelerate or accelerate the investigated probe-induced photoelectrons (see fig. 2.11). In case of metallic samples, the induced mirror charge of the electron cloud further decelerates the probe-photoelectrons.

In order to reach desired non-equilibrium states in experiments, pump induced space charge effects cannot be circumvented to all extent. Besides delay-dependent energy shifts of spectra, a broadening of bands around time zero ($\Delta t=0$) was observed in all experiments. Such a *loss of effective energy and momentum resolution* was interpreted as a weak form of spacecharge effects which becomes particularly strong when the probe-photoelectron travels through the pump-induced electron cloud.

2.2.4 Laser-Assisted Photoelectric Effect (LAPE)

The laser-assisted photoelectric effect (LAPE) creates sidebands in ultraviolet photoemission spectra in the presence of a strong laserfield from concurrent pump pulses. The sidebands appear as replicas separated by the pump photon energy from the original bands (see fig. 2.12b).

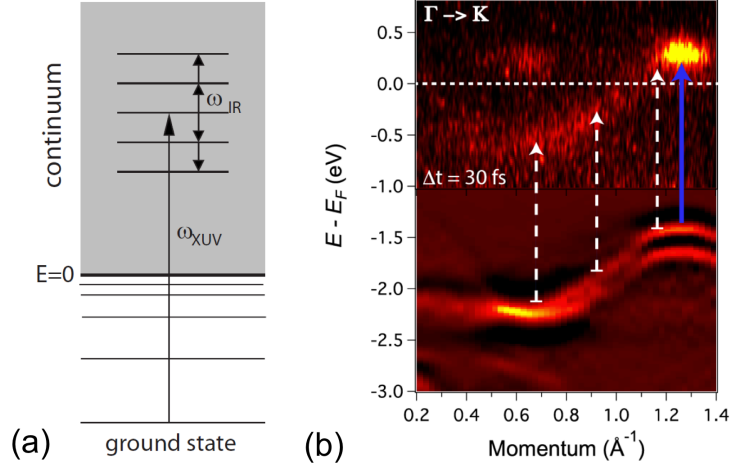


Figure 2.12: Laser-assisted photoelectric effect (LAPE): (a) Schematics of the LAPE principle from [107]. (b) Experimental observation of LAPE replicas of bulk MoSe₂ valence bands upon photoexcitation at 1.58eV photon energies from [108].

The principle of LAPE, originally known from photoemission from atoms, is understood as follows [107] (see fig. 2.12a): first, the initial state electrons are photoemitted into excited state in the continuum by the UV/XUV probe pulse with negligible influence by the driving pump laserfield. Then, the photoemitted electrons evolve as quasi-free electrons in the pump electric field, comparatively unaffected by the periodic crystal potential. This results in a redistribution of the photoelectrons in the continuum by absorption and stimulated emission of pump photons in the vicinity of the surface. The surface acts as a continuous sink of momentum normal to the surface, enabling the exchange of photons. The resulting photon-dressed final states of the photoelectrons are known as Volkov states [107].

In the “soft photon” limit ($E_{\text{kin}} \gg \hbar\omega_{\text{pump}}$), the ratio of the n -th order LAPE sideband’s intensity (I_n) in comparison to intensity of the field-free band ($I_0^{(\text{off})}$) can be approximated by ordinary Besselfunctions [107, 109], J_n :

$$I_n/I_0^{(\text{off})} = J_n^2 \left(\frac{\hbar\vec{k}_f \cdot \vec{E}_{\text{pump}}}{\omega_{\text{pump}}^2} \right) \quad (2.6)$$

For moderate field strengths, using $J_1(x) \approx \frac{x}{2}$ for small x , the first order LAPE sideband intensity can be approximated to:

$$I_1/I_0^{(\text{off})} \approx \frac{(\hbar\vec{k}_f \cdot \vec{E}_{\text{pump}})^2}{4\omega_{\text{pump}}^4} \quad (2.7)$$

In this regime, the sideband intensity depends linearly on the pump laser intensity. Track-

ing the temporal evolution of the LAPE signal allows exact timing synchronization between laser pulses and determination of crosscorrelated pulse durations.

2.3 Sample Growth and Characterization

2.3.1 Epitaxial Graphene

The features of epitaxial graphene on SiC, including the high-quality large-area single-crystalline structure, are ideal for photoemission spectroscopy, and have been widely studied in the past decade [91, 110–116].

Alternative growth methods (see sec. 1.3), such as exfoliation are not as suitable for photoemission spectroscopy mainly due to small flake sizes. While early difficulties given by polycrystalline structure growth are overcome for many years, CVD grown large-area single-domain graphene sheets have great suitability for photoemission spectroscopy [117]. However, CVD grown graphene usually rests upon metallic substrates, making such samples unpractical for time-resolved studies due to screening and space charge effects (see sec. 2.2.3). Post-transferring to semiconducting substrates or direct CVD growth on non-metallic substrates remains complicated and inconvenient [118].

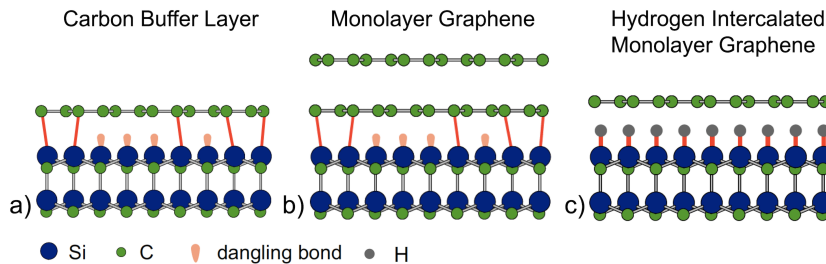


Figure 2.13: Sketch of atomic structure of epitaxial graphene grown on silicon carbide (SiC) from [119]: a) inactive carbon layer referred to as carbon buffer layer, b) thermal decomposed monolayer graphene (TDMLG), c) hydrogen intercalated monolayer graphene

The samples used in this work were grown by the group of U. Starke at the Max-Planck Institute of Solid State Research in Stuttgart (Germany) and the group of C. Coletti at the Istituto Italiano di Tecnologia at Pisa (Italy).

For the epitaxial growth procedure, pieces of ~ 5 -10mm were cut out from commercially available nominally on-axis oriented single crystalline 6H- or 4H-SiC(0001) wafers. The samples were first cleaned via wet chemical methods and then hydrogen-etched at about 1400°C in 1 bar of H_2 in order to remove polishing damages. This way the resulting surface contains atomically flat terraces, hundreds of nanometres wide separated by unit

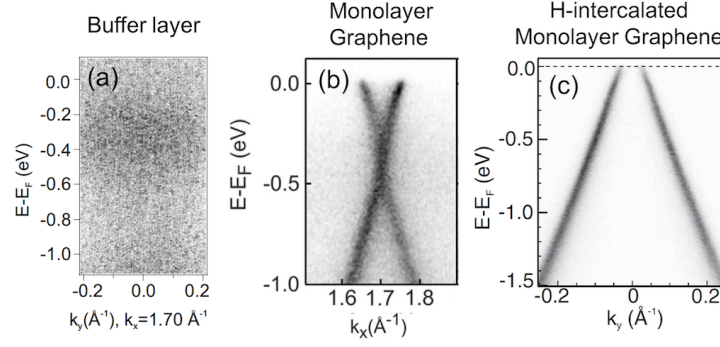


Figure 2.14: High resolution ARPES spectra of epitaxial graphene grown on SiC from [120]: a) inactive carbon buffer layer shows only non-dispersive states, b) thermal decomposited monolayer graphene (TDMLG) is n-doped ($\mu = 0.4eV$), c) hydrogen intercalated monolayer graphene is p-doped ($\mu = -0.2eV$)

cell high steps. The SiC samples were then graphitized in Ar atmosphere at elevated temperatures. Upon annealing at $1390^{\circ}C$ for 10min, a carbon buffer layer formed on the Si-face of the SiC: an inactive carbon layer with remaining SiC bonds which possesses no π -bands but only non-dispersive bands. At a temperature of $1470^{\circ}C$ a second carbon layer developed, which forms an actual sp^2 hybridized graphene monolayer and is referred to as thermal decomposited monolayer graphene (TDMLG) [121, 122]. TDMLG samples are intrinsically n-doped due to the substrate, with a chemical potential $\mu \sim 0.4eV$ and an effective screening constant of $\epsilon = 22$ [111].

Various modifications of epitaxial graphene are known nowadays. Apart from TDMLG, hydrogen intercalated monolayer graphene was used in this work, also known as quasi-free standing monolayer graphene (QFMLG). In order to intercalate the samples with hydrogen, graphene buffer layers were annealed in molecular hydrogen at a pressure close to 1bar and temperatures around $700^{\circ}C$ for approximately 20min. This treatment led to the intercalation of hydrogen underneath the buffer layer resulting in its electronic decoupling from the substrate by saturating the dangling SiC bonds with hydrogen atoms. In photoemission spectra, QFMLG generally shows sharper bands than TDMLG due to a smaller defect concentration, it is intrinsically p-doped with the chemical potential $\mu \sim -0.2eV$ and possesses an effective screening constant of $\epsilon = 4.4$ [111].

After growth, these samples were exposed to air, characterized by Raman spectroscopy, reinserted into ultrahigh vacuum, and cleaned via mild annealing at $800^{\circ}C$ (TDMLG) or $600^{\circ}C$ (QFMLG).

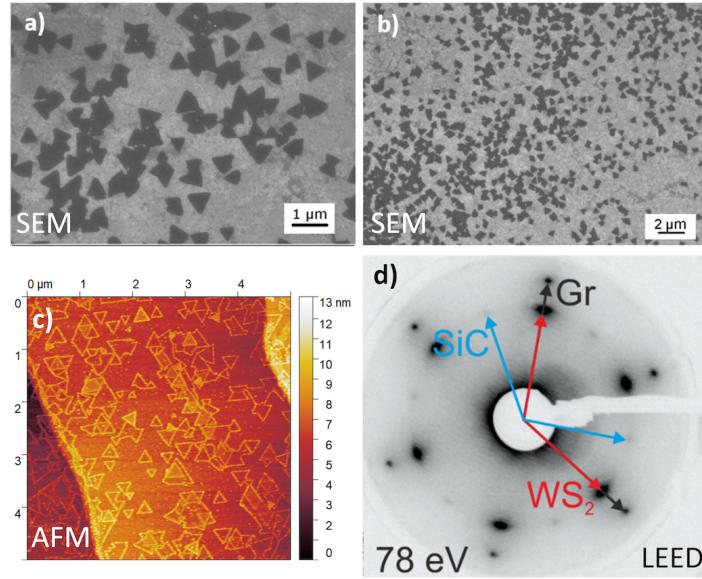


Figure 2.15: Sample characterization: (a), (b) SEM analysis: The pictures were obtained with an accelerating voltage of 5keV and a beam current of 30pA. (c) AFM analysis (d) LEED analysis: The picture was obtained with an electron energy of 78eV. Blue, black, and red arrows point to the diffraction spots of the SiC substrate, the graphene layer, and the WS₂ layer, respectively.

2.3.2 WS₂/Graphene Heterostructure

In chapter 5, an experiment investigating the relaxation dynamics of photoexcited WS₂/QFMLG/SiC(0001) heterostructure is described. The samples were grown and characterized by the group of Camilla Colleti at IIT@NEST at Pisa.

The hydrogen intercalated graphene samples were grown on commercial semiconducting n-doped 6H-SiC(0001) wafers from *SiCrystal GmbH* as described in sec. 2.3.1. The whole process was carried out in a commercial *Black Magic*TM growth chamber from *Aixtron*. The WS₂ growth was carried out in a standard hot-wall reactor by chemical vapor deposition (CVD) [123, 124] using WO₃ and S powders with a mass ratio of 1:100 as precursors. The WO₃ and S powders were kept at 900°C and 200°C, respectively. The WO₃ powder was placed close to the substrate. Argon was employed as carrier gas with a flow of 8sccm. The pressure in the reactor was kept at 0.5mbar.

The samples were characterized with secondary electron microscopy (SEM, ZEISS Merlin), atomic force microscopy (Anasys AFM), Raman and photoluminescence spectroscopy, as well as low energy electron diffraction (LEED). SEM (fig. 2.15a) reveals WS₂ single-crystalline domains with a side length varying between 300 and 700nm. In some areas several single crystalline domains are found to merge. From the low magnification image in fig. 2.15b a WS₂ coverage of 40% is estimated, suitable for the tr-ARPES analysis.

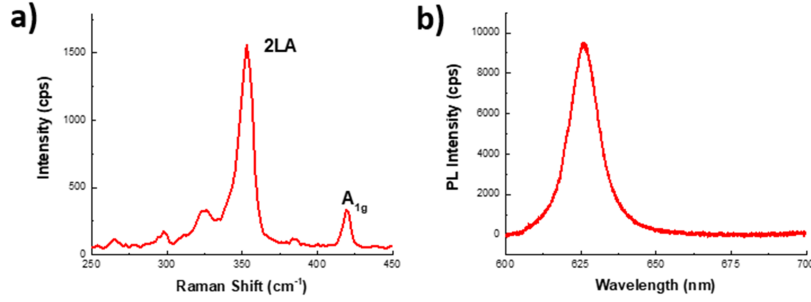


Figure 2.16: Raman (a) and photoluminescence spectrum (b). The measurements were performed with 1mW, 532nm laser excitation using a $100\times$ - $N.A.$ 0.90 objective at room temperature.

The orientation of the WS_2 triangles reveals the presence of two different domains with an angle of 60° between them.

The AFM analysis in fig. 2.15c confirms the island size distribution obtained by SEM. In addition, the topographical map reveals that about 10% of the flakes consist of WS_2 bilayers.

In order to assess the crystalline quality of the samples as well as the relative alignment of the WS_2 with respect to the graphene layer LEED measurements were carried out. Prior to the measurement the sample was mildly annealed at $200^\circ C$ in ultra-high vacuum. The LEED picture in fig. 2.15d confirms the identical azimuthal alignment of the two layers. In combination with the SEM results from fig. 2.15a it is concluded that the WS_2 islands grow such that either the ΓK - or the $\Gamma K'$ -direction of the WS_2 island is aligned to the ΓK -direction of the graphene layer.

The ratio of the 2LA and A_{1g} peak intensities in the Raman spectrum in fig. 2.16a confirms the presence of monolayer WS_2 [123]. Figure 2.16b shows the photoluminescence spectrum of the WS_2 excitonic emission centered at 625nm (1.98eV) [123].

2.3.3 Bulk WSe_2

The investigation described in chapter 6 studies Floquet effects in bulk tungsten diselenide ($2H-WSe_2$), a layered semiconducting material which belongs to the family of TMDCs and possesses an indirect bandgap of $\sim 1eV$. In the $2H$ -phase, WSe_2 has two layers per unit cell which are stacked in a hexagonal form and belongs to the space group D_{6h}^4 . These samples were grown by the group of Kai Roßnagel at the university of Kiel, Germany, following the method of chemical vapor transport reactions [125].

The primary materials, tungsten-wire 99.998% and selenide-granulate 99.999%, were enclosed at correct stoichiometric relations together with iodine as carrier gas within evac-

uated quartz ampullae (volume of 24cm^3). Placing ampullae in an oven with four temperature zones, the materials were subject to a temperature gradient. The temperatures ($T_{\text{max}}=920^\circ\text{C}$, $T_{\text{min}}=840^\circ\text{C}$) were chosen such that iodine fully changes to the vapor phase but the “feed” materials only sublime. Due to the temperature gradient, materials migrated from the hot to the colder sides of the ampullae. There, materials condensed and the crystal growth took place.

The crystal growth duration was 600 hours, whereafter samples were cooled down slowly and degased within fume hoods for several weeks.

For the photoemission experiments, samples were cleaved in ultra-high vacuum with the use of adhesive *Kapton* tape.

CHAPTER 3

Tracking Primary Thermalization Events in Graphene at Extreme Time Scales

The results from this chapter have been published in *I. Gierz, F. Calegari, S. Aeschlimann, M. Chávez Cervantes, C. Cacho, R. T. Chapman, E. Springate, S. Link, U. Starke, C. R. Ast, and A. Cavalleri*. “Tracking primary thermalization events in graphene with photoemission at extreme time scales”, *Phys. Rev. Lett.*, 115:086803, Aug 2015 [1].

3.1 Introduction

Two types of Auger scattering - Auger recombination and impact ionization - are amongst the primary processes that mediate the thermalization of across gap excited carriers in semiconductors. These two processes involve the annihilation or generation of an electron-hole pair by exchanging energy with a second carrier, which is either accelerated or decelerated. Impact ionization, also called inverse Auger scattering, is generally suppressed, as the decelerated carriers must have excess energies higher than the band gap itself (see fig. 3.1a).

The dynamics of pre-thermal Dirac carriers in photoexcited graphene are expected to host unconventional phenomena that differ from the ones known from typical semiconductors. For example, microscopic simulations [49, 50] predict that in graphene, which is gapless, impact ionization may dominate at early times.

This can be understood as follows [49, 50]: for a non-equilibrium distribution with holes in the valence band at $E = E_D - \frac{1}{2}\hbar\omega_{\text{pump}}$ and electrons in the conduction band at

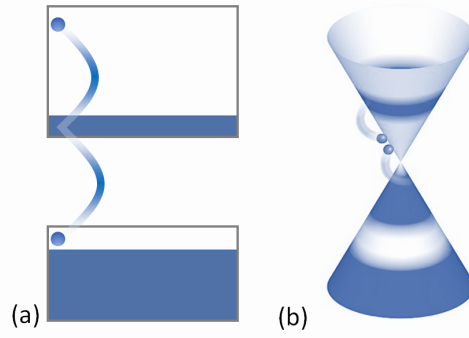


Figure 3.1: Auger scattering in a photoexcited prototype semiconductor (a) and in photoexcited graphene (b): In (a), thermalization is mediated by Auger recombination. In (b), impact ionization is predicted to be dominant at the earliest time delays [49, 50].

$E = E_D + \frac{1}{2}\hbar\omega_{\text{pump}}$ in undoped graphene (shown in fig. 3.1b), where E_D and $\hbar\omega_{\text{pump}}$ are the Dirac point and pump photon energy, respectively, the recombination of electron-hole pairs required for Auger recombination is strongly suppressed due to the lack of holes at the top of the valence band. On the other hand, the available phase space for the inverse process (impact ionization), where the excess energy of an electron high in the conduction band is used to generate secondary electron-hole pairs, is large. Therefore, impact ionization is believed to dominate over Auger recombination for as long as it takes to establish a thermalized electronic distribution.

As Auger processes change the number of carriers within individual bands, they are important not only for fundamental research but also for technological applications. Most notably, carrier multiplication, for which the absorption of a single photon may generate multiple electron-hole pairs due to a predominance of impact ionization, has raised interest for the design of highly efficient optoelectronic devices such as solar cells, photodetectors and for THz laser amplification.

However, these theoretical arguments apply only for undoped graphene and low excitation fluences (few $\mu\text{J}/\text{cm}^2$). At high pump fluences, the balance between impact ionization and Auger recombination is predicted to be reestablished within a few tens of femtoseconds, reducing the carrier multiplication factor considerably [49, 50]. Furthermore, real graphene samples typically rest on a substrate resulting in a non-negligible doping of the graphene layer. The presence of either electron or hole doping will reduce the importance of Auger-processes in general and shift the importance towards alternative scattering channels such as intraband electron-electron scattering.

Previous optical experiments deduced transient electron distribution functions by compar-

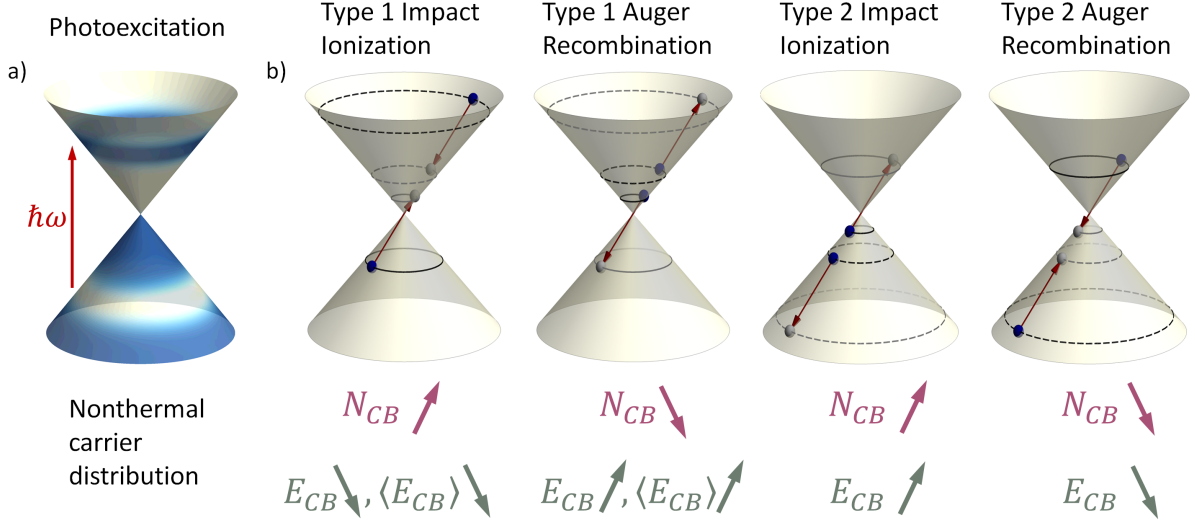


Figure 3.2: Photoexcitation and Auger scattering channels in graphene: a) Interband Excitation b) All forms of impact ionization and Auger recombination and their experimentally observable signatures in terms of total number of electrons N_{CB} , total kinetic energy E_{CB} , and average kinetic energy $\langle E_{CB} \rangle = E_{CB}/N_{CB}$, all within the conduction band.

ing differential transmission, reflectivity, or absorption data to model calculations. In this way, high-temporal-resolution experiments estimated an electronic thermalization time between 13 and 50fs [29, 86].

Carrier multiplication was observed in two experimental studies using optical pump-probe spectroscopy [86, 87]. Based on estimates of the absorbed photon density or relying on theoretical modelling, these experiments found values for carrier multiplication up to ~ 2 electron-hole-pairs per absorbed photon [86, 87] in a low fluence regime ($< 100 \mu\text{J}/\text{cm}^2$). Despite the indirect evidence for carrier multiplication from these studies, the direct observation of Auger-processes in graphene did not succeed so far. The occurrence of carrier multiplication, in fact Auger processes in general, is highly questionable from a fundamental perspective. Auger processes and their importance in graphene is a complex and so far unresolved theoretical problem (see section 1.2.1 on the *forward scattering resonance*). Theoretical predictions [48–52, 69] range from a complete suppression of Auger scattering to proclaiming them as predominant relaxation channels for photoexcited carriers. The matter demands further experimental investigations of prethermal photoexcited carriers in graphene.

Photoemission techniques, which directly measure electron numbers as a function of energy and momentum, are ideally suited for a direct visualization of Auger scattering. Figure 3.2 shows all possible Auger scattering events in graphene of which four different types can be identified. Each event leaves an observable individual fingerprint by modifying the number and (average) kinetic energy of electrons within the conduction

band¹.

Previous time- and angle-resolved photoemission spectroscopy (tr-ARPES) experiments were performed at pump fluences on the order of mJ/cm². The temporal resolution of ≥ 30 fs was then insufficient to resolve pre-thermal carrier distributions [35–38, 42–45].

In the experiment described here, < 8 fs extreme-ultraviolet pulses are used to detect this imbalance, tracking both the number of excited electrons and their kinetic energy with time- and angle- resolved photoemission spectroscopy. Over a time window of approximately 25fs after absorption of the pump pulse, an increase in conduction band carrier density and a simultaneous decrease of the average carrier kinetic energy is observed, revealing that relaxation is in fact dominated by impact ionization.

3.2 Experiment

The experiments were performed using the Materials Science end station at the Artemis user facility at the Rutherford Appleton Laboratory in Harwell, United Kingdom. Technical details of the setup are described in section 2.2.2. Lightly hole-doped quasi-freestanding epitaxial graphene samples (see sec. 2.3.1) were excited with pump pulses at 670nm (1.85eV) and 10fs pulse durations. Sub 10fs XUV probe pulses at 30eV photon energy were obtained by HHG and selected by a grating-based monochromator. The experiments were performed with two gratings with different dispersion (G300 with 300 grooves per mm and G60 with 60 grooves per mm), optimizing either time or energy resolution [98]. Both pump and probe pulses were s-polarized, with the electric field vector in the plane of the graphene sample perpendicular to the Γ K direction.

Fig. 3.3A shows tr-ARPES snapshots of graphene’s linear π -bands along the Γ K direction for selected pump-probe time delays across the rising edge of the pump-probe signal². Due to the s-polarization of the probe pulse [93] and to the photoelectron’s sublattice interference effect [128], described in section 2.1.1, only the right-hand branch of the Dirac cone was visible in this geometry. These snapshots were recorded with a temporal resolution³ of

¹Type 1 impact ionization and type 1 Auger recombination as defined in fig. 3.2 lead to distinct changes of the total and the average kinetic energy of electrons within the conduction band (E_{CB} and $\langle E_{CB} \rangle$, respectively). Type 2 Auger processes lead to a well-defined change of E_{CB} but are rather inefficient for the change of the average kinetic energy, on average they are expected to keep $\langle E_{CB} \rangle$ nearly unchanged.

²The optical matrix element describing the absorption of the pump photon is anisotropic with nodes along the direction of the pump polarization [78, 126, 127] (see appendix A.5), in this case perpendicular to the Γ K direction, and maxima in the direction perpendicular to the pump polarization, in this case Γ K. The response of the electronic structure was measured along the Γ K direction where the effect of the pump pulse is the strongest. In this direction in k-space the pump photo-response is also instantaneous, as further addressed in an experiment in chapter 4.

³The temporal resolution as given by the pump and probe pulse cross-correlation

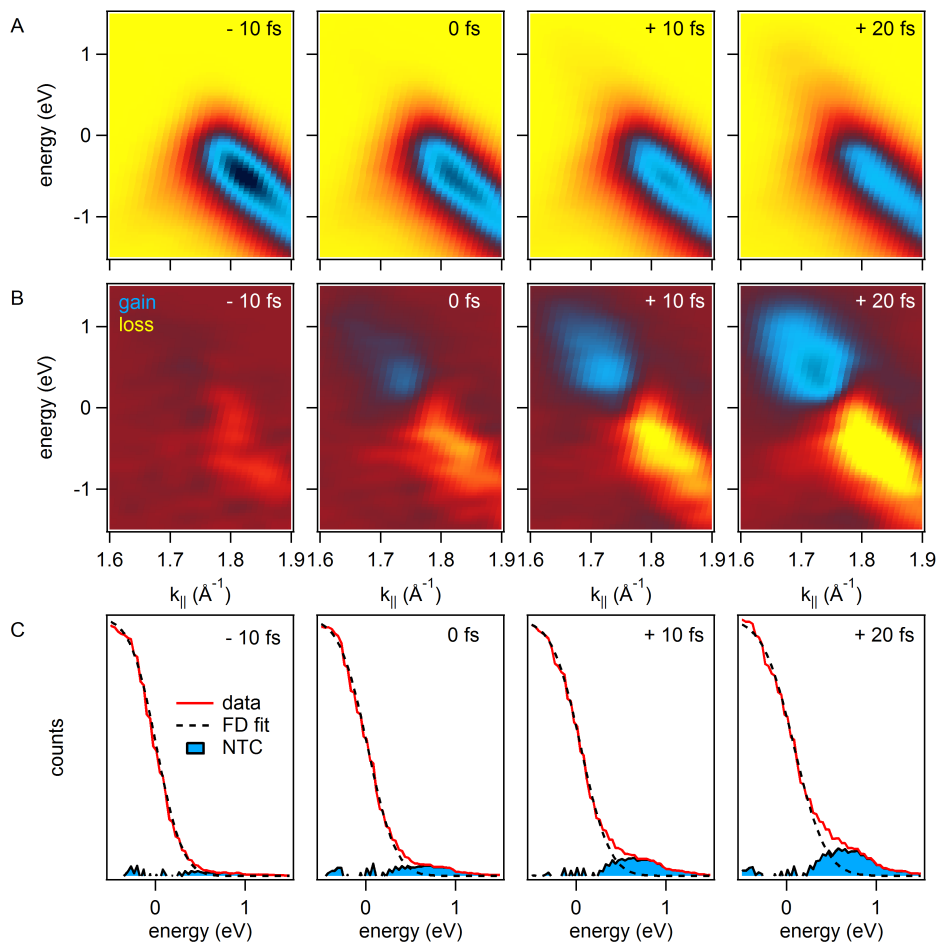


Figure 3.3: TrARPES measurements in graphene recorded with grating G300 featuring a temporal resolution of $\sigma=14\text{fs}$ and an energy resolution of 500meV . A: Snapshots for different pump-probe time delays. B: Corresponding pump-induced changes of the photocurrent. The data in panel A and B has been smoothed. C: Electronic distribution functions (red line) together with Fermi-Dirac fits (FD fit, black dashed line) revealing the presence of non-thermalized carriers (NTC, blue). The y-axis scale in C is linear. The measurements presented in this figure were carried out using the high-energy-resolution grating G300 (details see text).

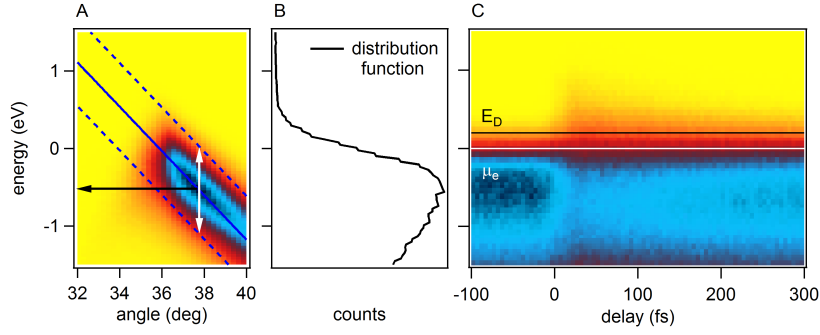


Figure 3.4: A Electron distributions in B were extracted from the raw data by summing up the intensity along the white arrow and attributing it to the energy indicated by the black arrow. Blue lines indicate the peak position (continuous) \pm full width at half maximum (dashed). B Electron distribution function as a function of energy. The drop at negative energy is caused by photoemission matrix element effects. C Electron distribution functions from B for different pump-probe delays as a two-dimensional color plot. The position of the chemical potential μ_e and the Dirac point E_D are indicated by white and black lines, respectively.

$\sigma = 14$ fs and an energy resolution of 500 meV achieved by using a monochromator grating with 300 grooves per millimeter (G300) [98].

The pump-induced changes of the photocurrent are plotted in fig. 3.3B. A loss (gain) of electrons below (above) the equilibrium chemical potential, which is used here as zero-energy reference, is observed.

From the snapshots in Fig. 3.3A, transient electron distribution functions were extracted and compared to Fermi-Dirac (FD) distributions in Fig. 3.3C. For that purpose lineouts at constant angle (energy distribution curves) were taken from the raw data, their integrated intensity was determined within the full width at half maximum (FWHM) of the peak and attributed to the energy of the peak position (see fig. 3.4). At negative delays, immediately before arrival of the pump pulse (-10 fs in Fig. 3.3C), the distribution follows a FD distribution, indicating the presence of a completely thermalized electron gas. Near zero time delay, a shoulder develops in the conduction band above $E_D = 200$ meV. The residual weight between the experimental distribution function (red line in Fig. 3.3C) and the FD fit (dashed black line in Fig. 3.3C) is taken as proportional to the number of non-thermal carriers (NTC's, blue shaded area in Fig. 3.3C). The number of NTC's keeps increasing until the peak of the pump-probe signal is reached at a time delay of ~ 20 fs. These NTC's can be understood as a precursor of the inverted carrier population observed in previous studies with longer pump pulses at slightly smaller photon energies [31,35,37]. Figure 3.5 summarizes the results of the Fermi-Dirac fits from fig. 3.3C. The figure shows the temporal evolution of the electronic temperature (T_e , light red), and of the number of non-thermal carriers (NTC, light blue), where NTC corresponds to the area of the blue

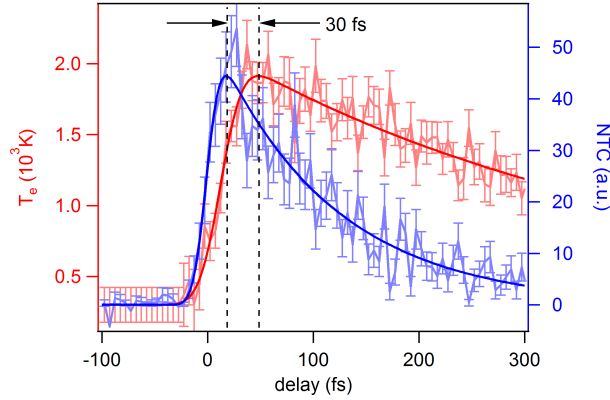


Figure 3.5: Results of Fermi-Dirac fit of the data shown in Fig. 3.3C. Electronic temperature (T_e , light red) and number of non-thermalized carriers (NTC, light blue) as a function of pump-probe delay. Zero time delay is defined as the middle of the rising edge of the number of non-thermalized carriers. Dark red and blue lines are fits to the data. Error bars represent the standard deviation.

shaded region in fig. 3.3C. Dark red and blue lines represent fits to the data including an error function to describe the rising edge and a single exponential decay. The temperature shows a delayed rise and peaks 30fs after the number of non-thermal carriers reaches its maximum. The decay times of the temperature and of the number of non-thermal carriers are $412\text{fs} \pm 32\text{fs}$ and $113\text{fs} \pm 6\text{fs}$, respectively.

Higher-temporal-resolution measurements were performed with a second monochromator grating with 60 grooves per millimeter (G60), resulting in a temporal resolution of $\sigma=8\text{fs}$ at the cost of loss in energy resolution. Respective snapshots of these measurements are shown in fig. 3.6. The number of carriers in the conduction band at $E > E_D$, N_{CB} , and their average kinetic energy, E_{CB}/N_{CB} , were determined directly from the raw data and displayed in Fig. 3.7. For about 25fs around zero pump-probe time delay, the average kinetic energy E_{CB}/N_{CB} was observed to decrease while the number of carriers N_{CB} kept increasing, indicating type 1 impact ionization (fig. 3.2).

3.3 Discussion

From these measurements the following scenario can be envisaged (see fig. 3.8): Impact ionization is the primary scattering mechanism during the first $\sim 25\text{fs}$, accumulating carriers at the bottom of the conduction band and establishing a precursor of the population inversion observed in previous studies [35, 37]. Alternative electron-electron scattering channels to Auger processes, such as intraband and interband scattering (see sec. 1.2.1)

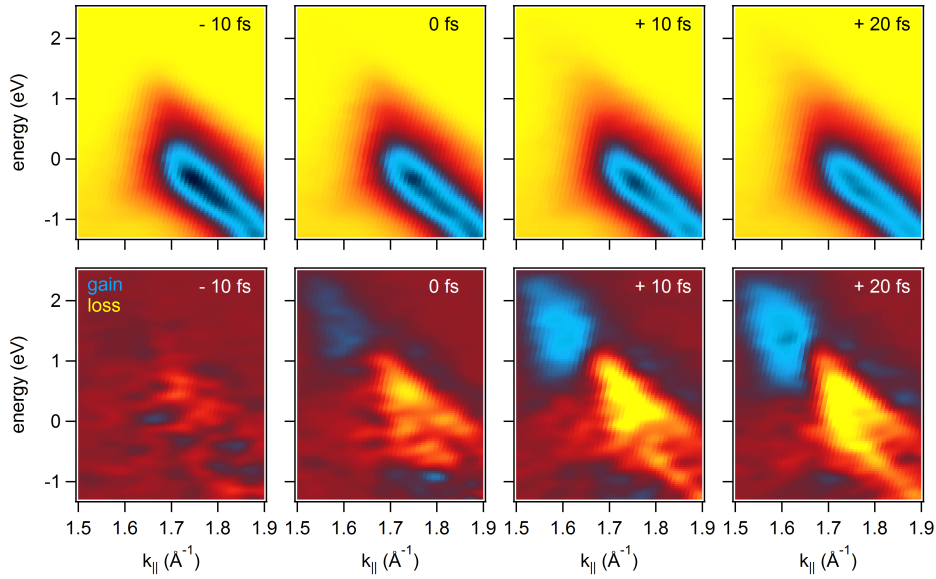


Figure 3.6: TrARPES snapshots recorded with grating G60 featuring a temporal resolution of $\sigma = 8\text{fs}$ and an energy resolution of 800meV : A: Snapshots for different pump-probe time delays. B: Corresponding pump-induced changes of the photocurrent. The data in panel A and B has been smoothed

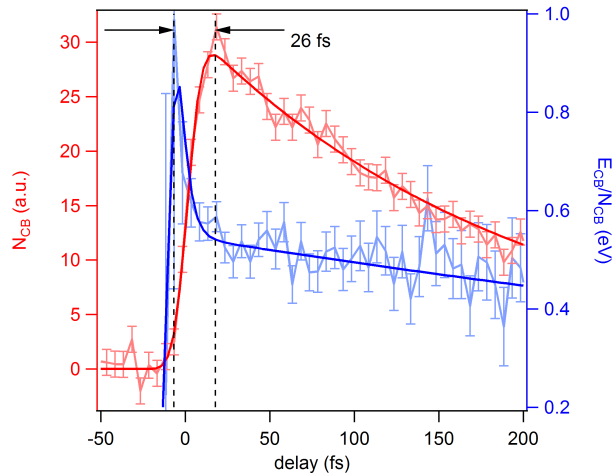


Figure 3.7: Direct evidence for impact ionization. Comparison between the temporal evolution of the total number of carriers inside the conduction band (N_{CB} , light red) and the temporal evolution of their average kinetic energy (E_{CB}/N_{CB} , light blue). Around zero time delay E_{CB}/N_{CB} already decreases while N_{CB} keeps increasing, indicating impact ionization. Dark red and blue lines are fits to the data that serve as guides to the eye. The fitting function consists of an error function to describe the rising edge plus a single (N_{CB}) or double exponential decay (E_{CB}/N_{CB}). The measurements presented in this figure were carried out using the low-energy-resolution grating G60 (details see text). Error bars represent the standard deviation.

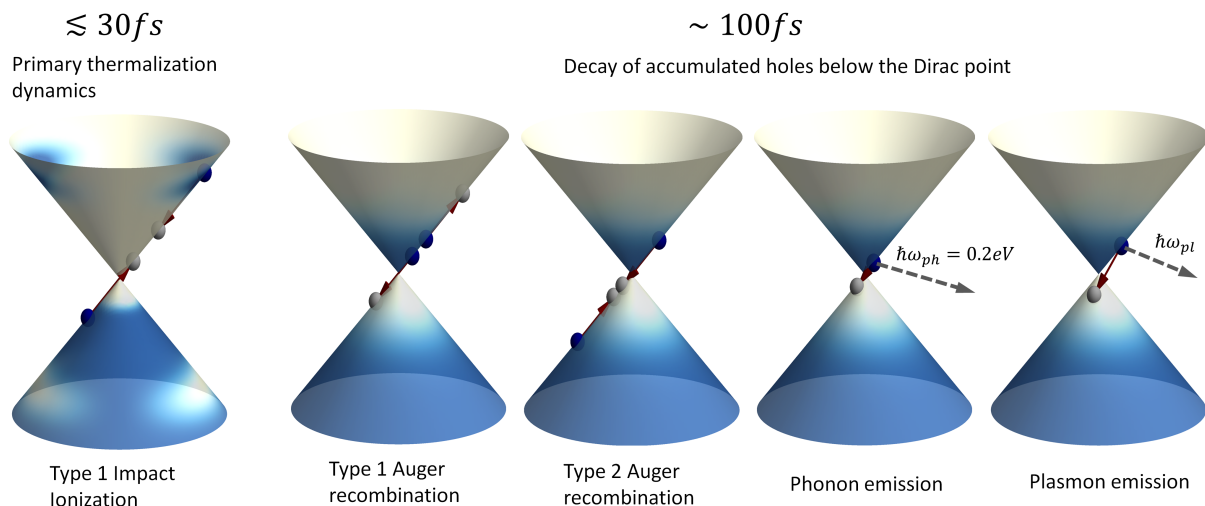


Figure 3.8: Thermalization dynamics in photoexcited graphene: a) Primary intraband thermalization is strongly driven by impact ionization. b) Interband thermalization is driven by Auger recombination, phonon emission and plasmon emission.

are assisting processes for intraband thermalization⁴ without changing the number of electrons in the conduction band.

At the stage, where the number and average kinetic energy of electrons within the conduction band fall simultaneously (as seen at $t \approx +20\text{fs}$ in fig. 3.7), the electrons reached a pre-equilibrated state where Auger recombination and impact ionization are happening at the same rate. Complete thermalization⁵ is hindered by the relaxation bottleneck imposed by the Dirac point [31, 35, 37].

The accumulated carriers at the bottom of the conduction band which are represented by the NTC's in fig. 3.3C and fig. 3.5, then decay through both types of Auger recombination, phonon emission and as recently proposed additionally by plasmon emission [53, 54] within $\sim 100\text{fs}$, re-establishing a (single) Fermi Dirac distribution [35]. This lifetime is similar to the one found for population inversion [31, 35, 37]. The fully thermalized system with elevated electronic temperature is known to cool down by optical and acoustic phonon emission [79–81] giving rise to the slowest decay time of $\sim 400\text{fs}$ observed in this experiment.

These experiments are the most direct experimental observation of Auger processes, in particular impact ionization, in graphene. Impact ionization is found to be a dominating

⁴Intraband thermalization is reached when the electrons within separate Dirac cones are at thermal equilibrium. In that situation, the total electronic distribution function is given by two Fermi-Dirac distributions, one for the upper and lower Dirac cone, respectively.

⁵Complete thermalization of the electronic system is reached, when the electronic distribution function over the whole bandstructure, i.e. both Dirac cones, is given by a single Fermi-Dirac distribution.

mechanism to thermalize excited carriers within the conduction band without establishing an equilibration between the bands. Impact ionization, and therefore carrier multiplication, only dominates up to the point where the counteracting process of Auger recombination becomes feasible. This point is reached when the electrons are accumulated at the bottom of the conduction band and the holes at the top of the valence band. These results support the recently pronounced indirect evidence of carrier multiplication in graphene in the weak excitation regime observed by optical pump-probe spectroscopy [86,87].

CHAPTER 4

Ultrafast Momentum Imaging of Pseudospin-Flip Excitations in Graphene

The results from this chapter have been published in *S. Aeschlimann, R. Krause, M. Chávez-Cervantes, H. Bromberger, R. Jago, E. Malić, A. Al-Temimy, C. Coletti, A. Cavalleri, and I. Gierz*. Ultrafast momentum imaging of pseudospin-flip excitations in graphene, *Phys. Rev. B*, 96:020301, Jul 2017 [2].

4.1 Introduction

The pseudospin of Dirac electrons in graphene manifests itself in a peculiar momentum anisotropy for photo-excited electron-hole pairs (see appendix A.5), resulting in unconventional hot carrier dynamics. These interband excitations are in fact forbidden along the direction of the light polarization, and are maximum perpendicular to it [78, 129].

The existence of such anisotropic photo-carrier distributions in graphene was observed in optical pump-probe experiments [126, 127, 130, 131], which showed a pronounced difference in the time-dependent optical response for different probe polarizations. The decay of the anisotropy extracted in this manner was attributed to optical phonon emission [78, 126, 127, 130, 132, 133]. However, a complete picture for these non-equilibrium phenomena can only be obtained by tracking both carrier energy and momentum in the time domain.

Utilizing the capabilities of trARPES, transient carrier distributions were sampled along the cone-shaped bandstructure over a two-dimensional area in k-space. This allowed

tracking the evolution of the anisotropic charge carrier distributions in all relevant dimensions.

The experiment is a complementary investigation to the sub 10fs-pulse trARPES study on graphene described in chapter 3, tackling thermalization dynamics from a different perspective. The previous study revealed the dominance of impact ionization over Auger recombination in the early thermalization dynamics, both representing Auger processes. The current study primarily investigates the relative importance of radial relaxation versus azimuthal relaxation as sketched in fig. 4.1). As discussed in detail in sec. 1.2.1, radial relaxation is mediated by Auger processes and collinear intraband and interband electron-electron scattering. Azimuthal relaxation, i.e. scattering around the cone, can happen through non-collinear electron-electron scattering and electron-phonon-scattering.

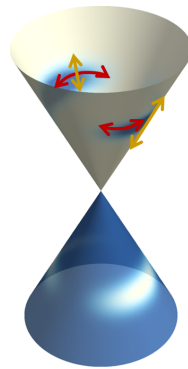


Figure 4.1: Sketch: Radial versus azimuthal scattering

In a first step, it is shown that the rapidly-established quasi-thermal electron distribution initially exhibits an azimuth-dependent temperature, consistent with relaxation through efficient collinear electron-electron scattering. Azimuthal thermalization is found to occur only at longer time delays, at a rate that is dependent on the substrate and the static doping level. Furthermore, pronounced differences in the electron and hole dynamics in n-doped samples are observed. By simulating the Coulomb- and phonon-mediated carrier dynamics it was possible to disentangle the influence of excitation fluence, screening, and doping, and develop a microscopic picture of the carrier dynamics in photo-excited graphene. The results clarify new aspects of hot carrier dynamics that are unique to Dirac materials, with relevance for photo-control experiments and optoelectronic device applications.

4.2 Experiment

Two different kinds of graphene samples were used for the present investigation. N-doped TDMLG samples with an equilibrium chemical potential of $\mu_e = +0.4\text{eV}$ and an effective screening constant of $\epsilon = 22$ [111] and p-doped QFMLG samples with the chemical

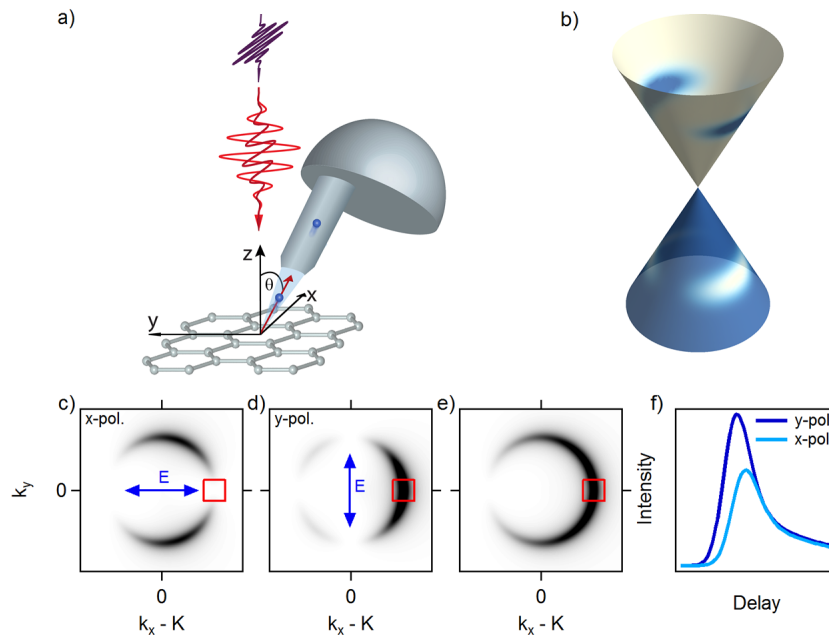


Figure 4.2: a) Sketch of the experimental setup. The sample is excited with x- or y-polarized pump pulses (red). Photoelectrons are ejected with x-polarized XUV probe pulses (violet) and pass through a hemispherical analyzer. b) Expected anisotropic charge carrier distribution after photo-excitation of monolayer graphene. Occupied and empty states are shown in blue and white, respectively. c)-e) Expected photoemission spectra at constant energy $E = E_D + \hbar\omega_{\text{pump}}/2$ as a function of k_x and k_y in the first instant after photo-excitation with x- (c) and y-polarized light (d) and the expected spectrum of an isotropic distribution (e). f) Sketch of the expected temporal evolution of the number of carriers inside the red box shown in (c), (d) and (e).

potential at $\mu_e = -0.2$ eV and an effective screening constant of $\epsilon = 4.4$ [111] were grown by the group of C. Coletti as described in sec. 2.3.1.

The trARPES experiments were performed at the Max Planck Institute for the Structure and Dynamics of Matter (MPISD) in Hamburg using pump pulses at 800nm (1.55eV) and the 17th harmonic at $\hbar\omega_{\text{probe}} = 26.3$ eV of the HHG spectrum for probe pulses (see sec. 2.2.2). The probe polarization was fixed along the x axis (fig. 4.2a). The polarization of the pump pulses was switched between x and y by rotating a half-wave plate. Both pump and probe impinged onto the sample at normal incidence. The experimental data shown in this work was obtained with pump fluences ranging from 1.3 to 2.8 mJ/cm². The energy and temporal resolution of the tr-ARPES experiment were 350 meV and 145 fs, respectively.

For the experiments reported here, a hemispherical analyzer with the entrance slit parallel

to the x axis was used, to measure the photocurrent as a function of energy and in-plane momentum k_x (fig. 4.2a). In order to record the complete Dirac cone (photocurrent as a function of k_x , k_y , and energy) the sample was rotated around the x axis.

Pump pulses at $\hbar\omega_{\text{pump}} = 1.5$ eV generated electron-hole pairs at $E_D \pm \hbar\omega_{\text{pump}}/2$, where E_D is the energy of the Dirac point where conduction and valence band meet (fig. 4.2b). As further discussed in appendix A.5, the optical excitation involves pseudospin flips which results in an angle-dependent transition probability $|M_{\text{excitation}}|^2 \propto \sin^2(\phi_k - \phi_A^{\text{pump}})$ [78, 129], where ϕ_k and ϕ_A^{pump} are the angles between the k-vector of the electron or the pump polarization and the x axis, respectively. As immediately evident from the expression above, the transition probability was then zero along the direction of the electric field ($\phi_k = \phi_A^{\text{pump}}$) and maximum perpendicular to it.

It is noted, that also the photocurrent is subject to a momentum-dependent transition matrix element. The photoemission cross section in graphene is proportional to $|M_{\text{photoemission}}|^2 \propto 1/2(1 + \cos(\phi_k - 2\phi_A^{\text{probe}}))$ [128, 134, 135], with $\phi_A^{\text{probe}} = 0$ in the present experiment, which turns part of the Dirac cone invisible. The photoelectron distribution can then be obtained by multiplying the actual carrier distribution with $|M_{\text{photoemission}}|^2$.

Figures 4.2c-e illustrate the expected photoelectron distribution at $E_D + \hbar\omega_{\text{pump}}/2$ as a function of k_x and k_y for excitation with x- and y-polarized light (figs. 4.2a and 4.2b), and, for comparison, for a homogeneous carrier distribution (fig. 4.2c). Figure 4.2f shows the expected evolution in time of the photocurrent inside the red box in figs. 4.2c-e [78, 126, 127, 130–133]. For pump pulses polarized along the x axis, the carriers are expected to fill these states only after scattering around the cone. Hence, one expects to measure a delayed rise and a lower peak signal for excitation with x-polarized light compared to excitation with y-polarized light. The two curves are also expected to overlap once the distribution becomes isotropic, before further cooling by optical and acoustic phonon emission occurs at longer time delays [25, 29, 42, 49, 79–83].

In a first set of experiments the photocurrent was measured as a function of energy and k_x , and the effect of x- and y-polarized excitation in p- and n-doped samples was compared (upper and lower panel of fig. 4.3, respectively¹). Figures 4.3a and 4.3d show ARPES

¹In fig. 4.3 the data sets for two samples were measured at different excitation fluences. In the supplementary information of [2] a corresponding data set for the n-doped sample with an excitation fluence of 1.3 mJ/cm² can be found. The reason why this data is not reported here, is that in this measurement there is a time-zero drift between the data recorded with x- and y-polarized pump pulses, due to unstable lab conditions on that particular day. It shall be stressed that the difference between the two peak intensities is similar to the one seen in fig. 4.3.

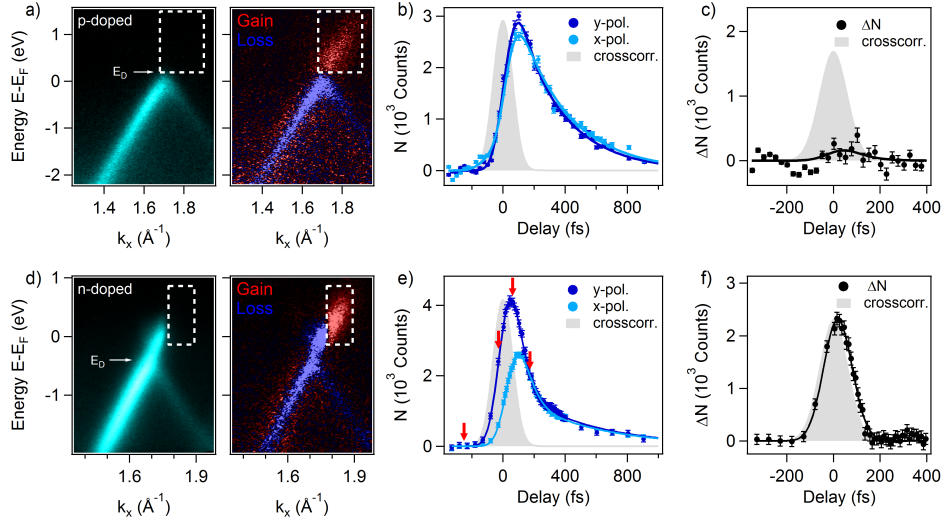


Figure 4.3: Photoemission data for p-doped (upper panel, excitation fluence of 1.5 mJ/cm^2) and n-doped graphene (lower panel, excitation fluence of 2.8 mJ/cm^2): a), d) ARPES spectra for negative time delays and pump-induced changes of the photocurrent for y-polarized pump pulses at the peak of the pump-probe signal. b), e) photocurrent integrated over the area of the white boxes in (a) and (d) versus pump-probe delay for x- (light blue) and y-polarized pump pulses (dark blue). The respective difference in intensity is shown in (c) and (f). The light gray area represents the temporal cross-correlation of pump and probe pulses.

snapshots at a negative pump-probe delay and pump-induced changes of the photocurrent at the pump-probe delay at which the signal was maximum. In order to compare the number of excited carriers for x- and y-polarized pump pulses the photocurrent was integrated over the area indicated in figs. 4.3a and 4.3d (white boxes). The time-dependent photocurrent is shown in figs. 4.3b and 4.3e. These data were fitted with an error function convolved with a double exponential decay. The temporal cross-correlation between pump and probe pulses (gray-shaded area), as obtained from the temporal derivative of the error function, has a full width at half maximum of 145 fs. For p-doped samples, the pump-probe signal for x- and y-polarized pump pulses was found to be the same within the error bars. On the contrary, a pronounced difference between the two pump polarizations was found for the n-doped sample, indicating the presence of a long-lived anisotropic carrier distribution. Figs. 4.3c and 4.3f show plots of the time-dependent anisotropy (difference between the dark and light blue curves in figs. 4.3b and 4.3e), which was found to relax at a rate limited by the time resolution of the experiment.

Time-dependent carrier distributions for all k_x and k_y values were measured for n-doped samples and x-polarized pump pulses. Constant-energy cuts integrated over an interval of $\pm 50 \text{ meV}$ around $E_D + \hbar\omega_{\text{pump}}/2$ are reported for four different delays (fig. 4.4), in-

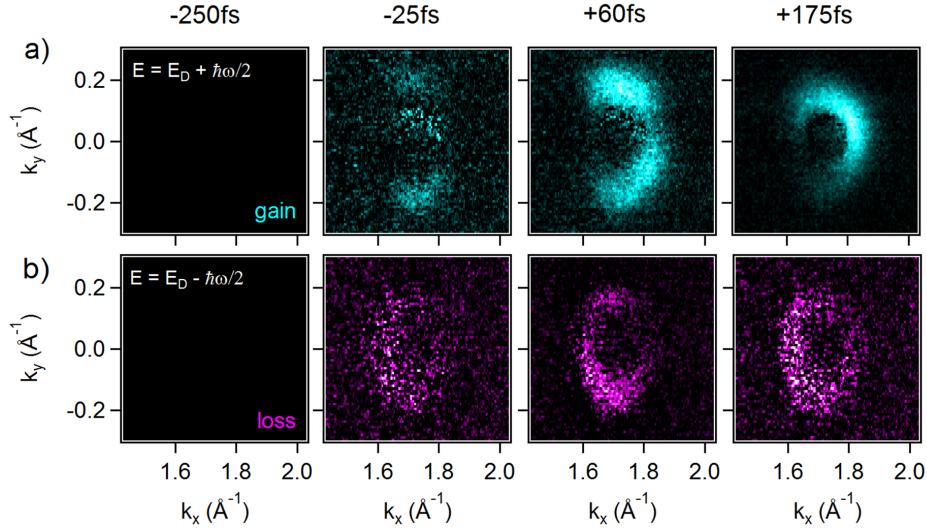


Figure 4.4: Photoemission spectra at constant energy $E = E_D + \hbar\omega_{\text{pump}}/2$ (panel a) and $E = E_D - \hbar\omega_{\text{pump}}/2$ (panel b) as a function of k_x and k_y for an excitation fluence of 2.8 mJ/cm^2 at four different time delays as indicated by red arrows in Fig. 4.3e. Note that the sickle-shaped image at $t = 175 \text{ fs}$ is slightly rotated away from the k_x axis due to a small azimuthal misalignment of the sample and that the photoemission cross section for the valence band leads to zero intensity on the opposite side of the Dirac cone compared to the conduction band.

indicated by red arrows in fig. 4.3e. At negative delay ($t = -250 \text{ fs}$) no excited carriers are detected. For time delays $t = -25 \text{ fs}$, that is half way through the rising edge, the anisotropic carrier distribution is already observable, reaching its maximum at $t = +60 \text{ fs}$. At $t = +175 \text{ fs}$ the carrier distribution becomes isotropic, with an angular dependence caused by the photoemission matrix element alone. The measured spectra nicely agree with the expectations shown in figs. 4.2c-e. For comparison, the photoexcited hole distribution at $E_D - \hbar\omega_{\text{pump}}/2$ is shown in fig. 4.4b. It is noted that the photoemission cross section for the valence band is flipped with respect to the one of the conduction band. Sketches of the expected measured hole distribution can be obtained by mirroring fig. 4.2c-e on the k_y -axis. The measured hole distribution (fig. 4.4b) shows a much smaller anisotropy than the measured electron distribution (fig. 4.4a).

By integrating the two-dimensional ARPES spectra in fig. 4.3d along k_x for x- and y-polarized pump pulses, transient electron distribution functions were obtained [35,136] at the minima and maxima of $|M_{\text{excitation}}|^2$, respectively, in the direction where the photoemission cross section is maximum. The gray data points in fig. 4.5a show the distribution at negative delay. Light and dark orange data points show the distributions for x- and y-polarized pump pulses at $t = +50 \text{ fs}$ where the pump-probe signal reaches its maximum for excitation with y-polarized light. The black lines are Fermi-Dirac fits convolved with

a Gaussian with a full width at half maximum of 350 meV to account for the finite energy resolution. The temporal evolution of the resulting electron temperature is shown in fig. 4.5b. At early times, the electron temperature along k_x is found to be smaller for x-polarized pump pulses than for y-polarized pump pulses.

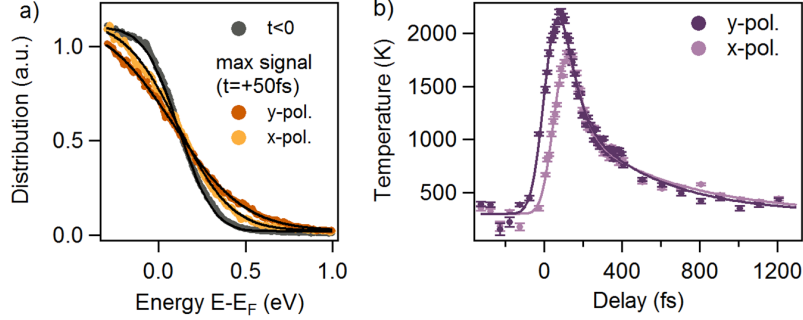


Figure 4.5: a) Electron distribution functions along the k_x direction for n-doped graphene. Gray curves show the distribution at negative pump-probe delay, light and dark orange curves show the respective distributions at $t = 50$ fs for x- and y-polarized pump pulses. Black curves are Fermi-Dirac fits. b) Temporal evolution of the electron temperature obtained from the fits in (a).

4.3 Microscopic Simulations

In order to clarify the influence of static doping and substrate screening on the time-dynamics, microscopic simulations were carried out by the group of Ermin Malic at Chalmers University of Technology (Gothenburg, Sweden). The applied many-particle approach is built around Graphene Bloch Equations (GBE) that have been derived in the density matrix formalism within the second-order Born-Markov approximation [137–141]. More details on the theoretical approach can be found in refs. [78, 142]. The effects arising from the electrons in the core states and the surrounding substrate are taken into account by introducing a dielectric background constant ε_{eff} . The screening stemming from other valence electrons is calculated within an effective single-particle Hamiltonian approach leading to the Lindhard approximation of the dielectric function $\varepsilon(\vec{q})$ [138, 142]. The aim of the simulations was to model the measured anisotropy in trARPES experiments on p- and n-doped graphene samples defined as

$$\Delta N = \frac{1}{\Delta E} \int_{E_F}^{E_{\max}} \left(\rho_E^{k_x}(t) - \rho_E^{k_y}(t) \right) dE. \quad (4.1)$$

Fig. 4.6a shows the simulated dynamics of the anisotropy ΔN for both samples that were used in the experiment. To disentangle the elementary processes responsible for the

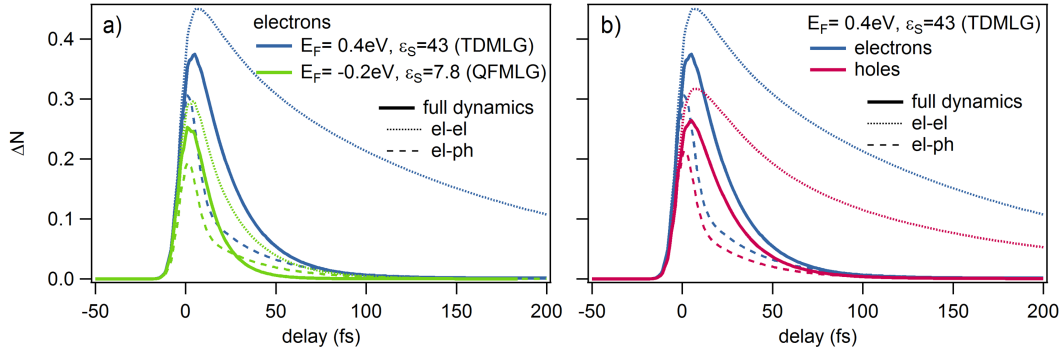


Figure 4.6: a) Simulated temporal evolution of the electron-anisotropy ΔN comparing the n-doped TDMLG versus the p-doped QFMLG sample b) Electron- vs. hole-anisotropy both in the TDMLG sample. Solid lines represent the full dynamics, dotted and dashed lines represent the dynamics for electron-electron and electron-phonon scattering only, respectively.

decay of the anisotropy, the full dynamics (continuous lines) as well as calculations taking into account only electron-phonon (el-ph, dashed lines) or electron-electron scattering (el-el, dotted lines) are plotted. It might seem surprising that the anisotropy decays faster when only electron-phonon scattering is present in comparison to the full dynamics. The reason is that the dynamical scattering mechanisms are not independent of one another. In particular, fast electron-electron scattering can minimize the probability of a certain excited electron state to decay via electron-phonon scattering. In agreement with the experimental observations, a more pronounced and a longer-lived carrier anisotropy for the n-doped sample compared to the p-doped sample is found. Furthermore, fig. 4.6b shows the simulated temporal evolution of the electron anisotropy in the conduction band and the hole anisotropy in the valence band for the n-doped sample. In good qualitative agreement with the experimental results, the hole anisotropy is found to be smaller and to decay faster.

4.4 Discussion

It is first noted that the measured electron distribution can be described with a Fermi-Dirac distribution at all pump-probe delays (fig. 4.5a), indicating that electron-electron scattering thermalizes the photo-excited carriers on a time scale short compared to the temporal resolution. The observed pump-polarization dependence of the electron temperature (fig. 4.5b) shows that this quasithermal state has an azimuth-dependent temperature and provides direct evidence that electron-electron scattering is highly efficient along lines pointing radially away from the Dirac point as predicted in [78, 132].

Relaxation around the cone, which re-establishes an isotropic carrier distribution, can

occur through electron-phonon scattering or non-collinear electron-electron scattering. While the decay of the anisotropy is believed to be dominated by phonon emission in the low fluence regime [78, 126, 132], it is expected that non-collinear electron-electron scattering is of similar importance for the high excitation fluences applied in this work². In agreement with the experiment, theoretical simulations find a larger and longer-lived anisotropy for the n-doped sample compared to the p-doped sample (fig. 4.6a). As the measured lifetime of the anisotropy in the present work is resolution limited, the difference in lifetime shows up as a difference in amplitude of the measured anisotropy.

The reason for the enhanced lifetime of the anisotropy in the n-doped sample can be traced back to the large value of the chemical potential that reduces the scattering phase space for both non-collinear electron-electron (dotted lines in fig. 4.6a) and electron-phonon scattering (dashed lines in fig. 4.6a)³. Moreover, the strong effective screening of the Coulomb interaction due to the large dielectric constant of the substrate in the n-doped sample substantially reduces non-collinear electron-electron scattering further so that electron-phonon scattering remains the main decay mechanism of anisotropy as seen in fig. 4.6a.

The microscopic simulations are also able to reproduce the difference between electron and hole dynamics in the TDMLG sample (fig. 4.6b). This can be explained by the finite positive value of the chemical potential that breaks the electron-hole symmetry and increases (decreases) the scattering phase space for holes (electrons) both for non-collinear carrier-carrier and carrier-phonon scattering.

Based on the experimental observations and the simulations, the following hierarchy of electronic relaxation mechanisms in graphene can be established: The fastest scattering process is given by collinear electron-electron scattering where electrons are redistributed along radial lines in k-space that go through the Dirac point. The responsible collinear scattering events are given by Auger processes, already observed in the previous experiment in chapter 3, and by collinear intraband and interband scattering. The dominance of collinear scattering holds for a wide accessible parameter range concerning the static doping level, background dielectric screening, and pump fluence and is most likely explained by the *forward scattering resonance* (see sec. 1.2.1).

Electron-phonon scattering and non-collinear electron-electron scattering are happening on a slower and similar time-scale in the 50-200fs range. Both are strongly dependent on the static doping level, while the latter is also influenced by substrate screening and

²This is confirmed in a further simulation for neutrally doped graphene with low substrate dielectric screening shown in appendix C

³To get profound insights into the elementary processes behind the anisotropy, additional simulations were carried out to investigate the impact of pump fluence, doping, and substrate screening on the anisotropy. These simulations and a detailed discussion thereof can be found in appendix C.

dynamic screening of the Coulomb-interaction.

These results visualize photo-carrier dynamics that are unique to Dirac materials, in which the pseudospin is responsible for peculiar anisotropic photo-carrier distributions. The ability to tune hot carrier dynamics via doping or screening might potentially be exploited in graphene-based thermoelectric devices [143–147], or other opto-electronic applications of this class of solids.

CHAPTER 5

Ultrafast Charge Transfer in Epitaxial WS₂/Graphene Heterostructure

A manuscript based on the experimental results described in this chapter has been submitted: *S. Aeschlimann, M. Chavez-Cervantes, R. Krause, A. Rossi, S. Forti, F. Fabbri, C. Coletti, and I. Gierz*, “Direct evidence for ultrafast charge separation in epitaxial WS₂/graphene heterostructure”, *arXiv:1904.01379*, 2019 [3].

5.1 Introduction

Starting with the first extraction of monolayer graphene in 2004 [5], the isolation of other two-dimensional materials subsequently followed the years thereafter. Among these are hexagonal Boron nitride (hBN) and the big group of transition metal dichalcogenides (TMDC) [6]. Despite possessing similar hexagonal atomic lattice structures, both materials exhibit very different electronic properties that differ from those of graphene. Since their sublattice symmetry is broken due to differing sublattice atoms, the electrons behave like massive Dirac fermions with band gaps spanning over several eV 's (see appendix A.3.4 for details on hexagonal lattice systems with broken inversion symmetry). 2H-TMDCs additionally show a large spin-splitting of their valence band structure due to strong spin-orbit coupling in combination with the lack of inversion symmetry.

The availability of many different two-dimensional materials has opened up the possibility to create novel ultimately thin heterostructures with completely new functionalities based on tailored dielectric screening and various proximity-induced effects [148–150]. Proof-of-principle devices for future applications in the field of electronics and optoelectronics

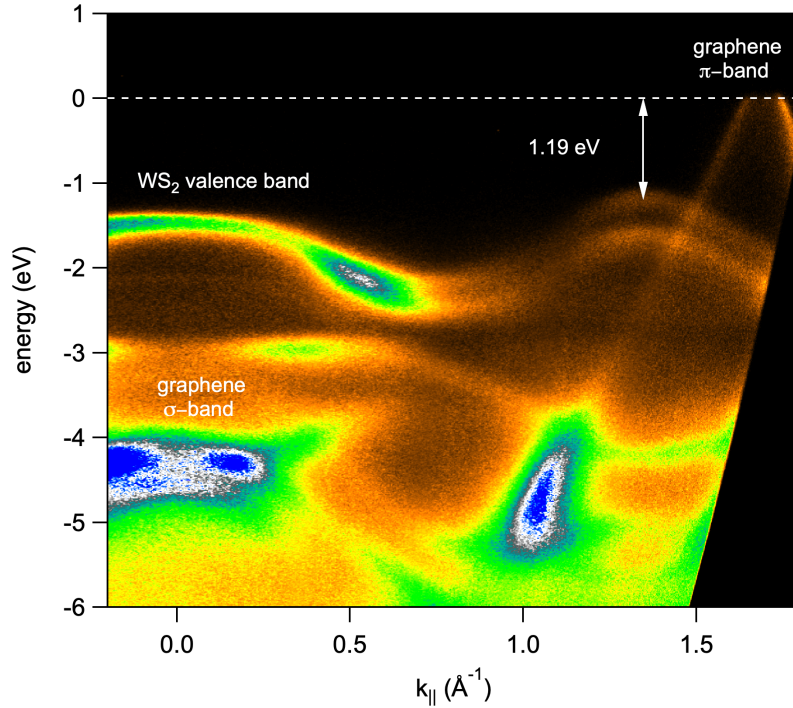


Figure 5.1: Equilibrium high resolution ARPES spectrum of a WS₂/graphene heterostructure measured along the ΓK -direction with an unpolarized helium lamp.

have been realized [11, 151, 152].

The focus of the experiment described here lies on epitaxial van-der-Waals heterostructures consisting of monolayer WS₂, a direct-gap semiconductor with a sizable spin splitting of the band structure [153, 154], and monolayer graphene, a semimetal with conical band structure and extremely high carrier mobility [5, 70, 155], grown on hydrogen-terminated SiC(0001) as described in sec. 2.3.

Indications for ultrafast charge transfer [55–59] and proximity-induced spin-orbit coupling effects [60–62] make WS₂/graphene and similar heterostructures promising candidates for future optoelectronic and optospintronic applications.

In the present study, the ultrafast charge transfer in the WS₂/graphene heterostructure is investigated. It is found that, after photoexcitation at resonance to the exciton in WS₂, the photoexcited holes rapidly transfer into the graphene layer while the photoexcited electrons remain in the WS₂ layer. This highly asymmetric charge transfer is interpreted in terms of differences in scattering phase space caused by the relative alignment of WS₂ and graphene bands as revealed by high resolution ARPES. In combination with spin- and valley-selective excitation using circularly polarized light the investigated WS₂/graphene heterostructure might provide a new platform for efficient optical spin

injection into graphene.

5.2 Experiment

Setting out to reveal the relaxation pathways of photogenerated electron-hole pairs in WS₂/graphene, trARPES was employed at the Hamburg photoemission laboratory (see sec. 2.2.2 for details on the experimental setup). For that purpose the heterostructure was excited with 2eV pump pulses ($\lambda = 620nm$) resonant to the A-exciton in WS₂ [58] and photoelectrons were ejected with a second time-delayed probe pulse at 26eV photon energy and $\sim 100fs$ pulse duration.

The overall energy and time resolution of the experiment are 240meV and 200fs, respectively. As photoemission spectroscopy is an extremely surface sensitive technique, samples with an incomplete WS₂ coverage of $\sim 40\%$ were used in order to eject photoelectrons from both the WS₂ and the graphene layer. The sample growth and a detailed characterization of the epitaxial WS₂/graphene heterostructure is described in sec. 2.3.2.

A high-resolution ARPES spectrum showing the band structure of such a heterostructure across the first Brillouin zone was obtained with a helium lamp and in collaboration with the group of Martin Aeschlimann at the university of Kaiserslautern, Germany (fig. 5.1). The spectrum allows for a precise determination of the energetic band alignments: the graphene layer is found to be hole-doped with the Dirac point located 0.3eV above the chemical potential. The top of the spin-split WS₂ valence band is found to be 1.2eV below the chemical potential.

Experimental Results

Figure 5.2a shows a trARPES snapshot of the band structure close to the WS₂ and graphene K-points measured at negative pump-probe delay before the arrival of the pump pulse. Here, the spin splitting of the WS₂ valence band is not resolved due to space charge broadening from the presence of the pump beam, even at negative delays (see sec. 2.2.3). Figure 5.2b shows the pump-induced changes to the photocurrent after photoexcitation at a pump photon energy of 2eV with a pump fluence of $2mJ/cm^2$. The snapshot in fig. 5.2b was taken at a pump-probe delay of 200fs where the pump-probe signal reaches its maximum. Red and blue colors indicate gain and loss of photoelectrons, respectively.

In order to analyze this rich dynamics in more detail, firstly the transient peak positions of the WS₂ valence band and the graphene π -band are determined. For that purpose line profiles along the dashed lines in fig. 5.2a are extracted and fitted by a gaussian (gray dashed line in fig. 5.2a) yielding the energy shift of the WS₂ valence band and a

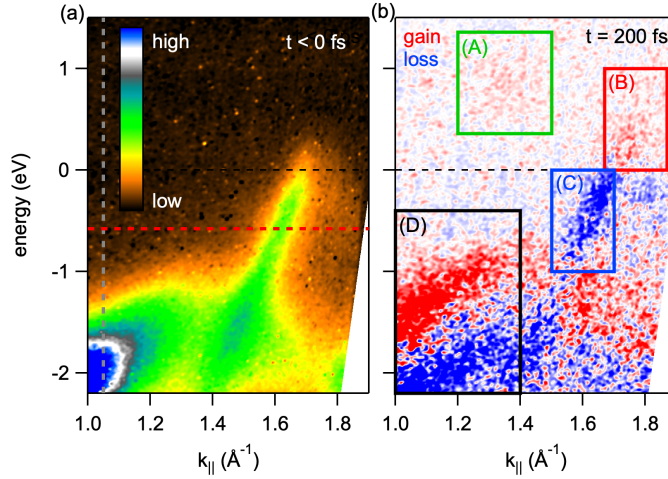


Figure 5.2: Photocurrent dynamics in an epitaxial WS₂/graphene heterostructure. (a) Photocurrent along the Γ K-direction measured with p-polarized XUV pulses at 26 eV and at negative pump-probe delay. Dashed gray and dashed red lines mark the position of the line profiles used to extract the transient peak shifts in fig. 5.3. (b) Pump-induced changes to the photocurrent 200fs after photoexcitation. The boxes indicate the area of integration for the pump-probe traces displayed in fig. 5.4.

Lorentzian (red dashed line in fig. 5.2a) yielding the momentum shift of the graphene π -band. The energy shift of the graphene π -band is then obtained by multiplying the momentum shift with the Fermi velocity. It is found that the WS₂ valence band shifts up by 90meV (fig. 5.3a) and the graphene π -band shifts down by 50meV (fig. 5.3b). The exponential lifetime of these shifts is found to be 1.2 ± 0.1 ps for the valence band of WS₂ and 1.7 ± 0.3 ps for the graphene π -band. These peak shifts provide first evidence of a transient charging of the two layers, where additional positive (negative) charge increases (decreases) the binding energy of the electronic states. It is noted that the up-shift of the WS₂ valence band is responsible for the prominent pump-probe signal in the area marked by the black box in fig. 5.2b.

Next, the pump-probe signal is integrated over the areas indicated by the colored boxes in fig. 5.2b and the resulting counts are plotted as a function of pump-probe delay in fig. 5.4. Figure 5.4A shows the dynamics of the photoexcited carriers close to the bottom of the conduction band of the WS₂ layer with a lifetime of 1.1 ± 0.1 ps as obtained from an exponential fit to the data.

Figure 5.4B and C show the pump-probe signal of the graphene π -band. Interestingly, it is found that the gain of electrons above the equilibrium chemical potential (fig. 5.4B) has a much shorter lifetime (180 ± 20 fs) compared to the loss of electrons below the equilibrium chemical potential (1.8 ± 0.2 ps in fig. 5.4C). Further, the initial gain of the photocurrent

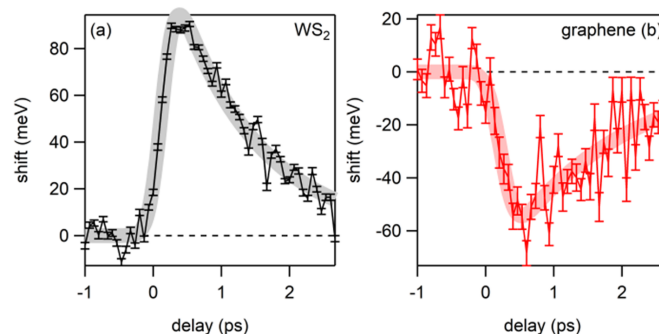


Figure 5.3: Transient band shifts after photoexcitation. Change in peak position of the WS₂ valence band (a) and graphene π -band (b) as a function of pump-probe delay together with exponential fits. The lifetime of the WS₂ shift in (a) is 1.2 ± 0.1 ps, the lifetime of the graphene shift in (b) is 1.7 ± 0.3 ps.

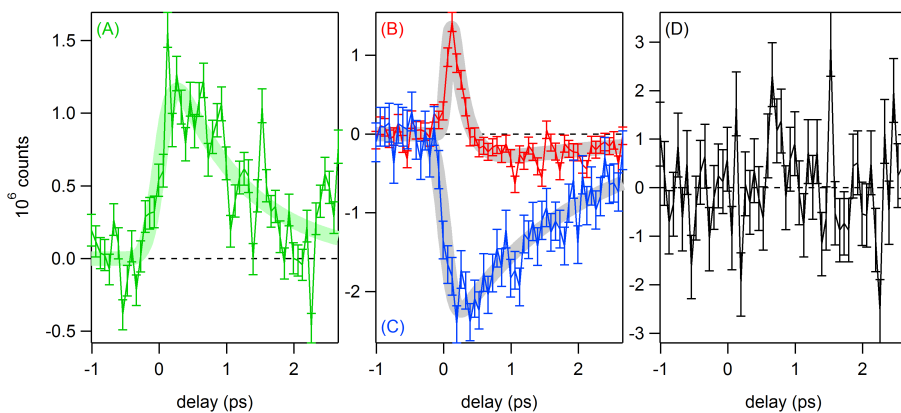


Figure 5.4: Energy- and momentum-resolved carrier dynamics in the WS₂/graphene heterostructure. Pump-probe traces as a function of delay obtained by integrating the photocurrent over the area indicated by the boxes in fig. 5.2b. The thick lines are exponential fits to the data. (A) Gain in the conduction band of WS₂. (B) Pump-probe signal of the π -band of graphene above the equilibrium chemical potential. (C) Pump-probe signal of the π -band of graphene below the equilibrium chemical potential. (D) Net pump-probe signal in the valence band of WS₂. The lifetimes are found to be 1.2 ± 0.1 ps in (A), 180 ± 20 fs (gain) and ~ 2 ps (loss) in (B), and 1.8 ± 0.2 ps in (C).

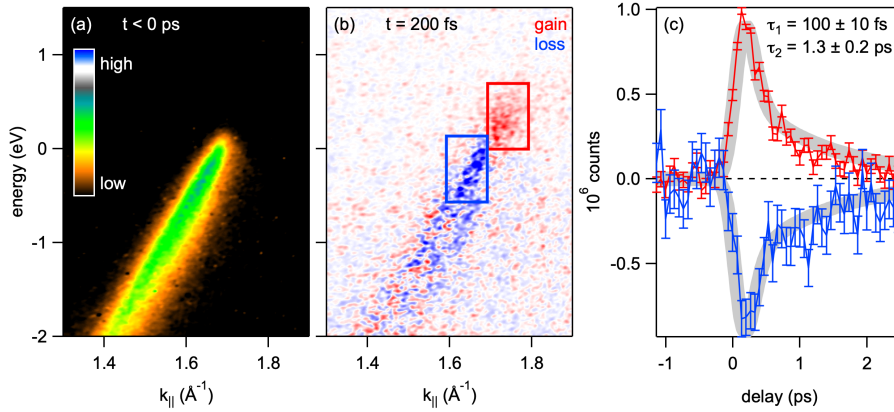


Figure 5.5: Photocurrent dynamics in uncovered QFMLG. (a) Photocurrent along the ΓK -direction for negative pump-probe delay. (b) Pump-induced changes to the photocurrent 200fs after photoexcitation at a pump photon energy of 2eV with a pump fluence of 2mJ/cm². (c) Pump-probe traces as a function of delay obtained by integrating the photocurrent over the area indicated by the red and blue boxes in panel (b). Thick gray lines are double-exponential fits to the data.

in fig. 5.4B is found to turn into loss at $t=400$ fs with a lifetime of ~ 2 ps. This asymmetry between gain and loss is found to be absent in the pump-probe signal of uncovered monolayer graphene (QFMLG) under identical excitation conditions (see fig. 5.5), indicating that the asymmetry is a consequence of interlayer coupling in the WS₂/graphene heterostructure.

The observation of a short-lived gain and long-lived loss above and below the equilibrium chemical potential, respectively, indicates that electrons are efficiently removed from the graphene layer upon photoexcitation of the heterostructure. As a result the graphene layer becomes positively charged which is consistent with the increase in binding energy of the π -band found in fig. 5.3b. Further, the down-shift of the π -band removes the high-energy tail of the equilibrium Fermi-Dirac distribution from above the equilibrium chemical potential which partly explains the change of sign of the pump-probe signal in fig. 5.4B. It will be shown below that this effect is further enhanced by the transient loss of electrons in the π -band.

This scenario is supported by the net pump-probe signal of the WS₂ valence band in fig. 5.4D. This data was obtained by integrating the photocurrent over the area given by the black box in fig. 5.2b that captures the valence band at all pump-probe delays independently of the transient peak shift. Within the experimental error bars no indication for the presence of holes in the valence band of WS₂ is found for any pump-probe delay. This indicates that, after photoexcitation, these holes are rapidly refilled on a time scale short compared to the temporal resolution.

In order to provide final proof for the hypothesis of ultrafast charge separation in the WS₂/graphene heterostructure the number of transferred holes in the graphene layer is determined. For that purpose, energy distribution curves capturing the graphene π -band were fitted in the vicinity of the equilibrium chemical potential by Fermi-Dirac distributions for all pump-probe delays. These fits describe the transient electronic distribution well at all times, indicating a rapid thermalization of the photoexcited carriers in the π -band in excellent agreement with literature [1, 29, 86]. The resulting shift of the chemical potential referenced with respect to the vacuum level $\mu_{e(vac)}$ and the transient electronic temperature T_e are shown in figs. 5.6a and b, respectively. The transient shift of the chemical potential referenced with respect to the graphene Dirac point $\mu_{e(ED)}$ (fig. 5.6c) is then calculated by subtracting the graphene band shift in fig. 5.3b from the shift of $\mu_{e(vac)}$ in fig. 5.6b. The transient values of $\mu_{e(ED)}$ and T_e in figs. 5.6b and c then allow for a direct calculation of the change of the total number of electrons in the graphene layer (fig. 5.6d) via

$$\Delta n_e(t) = \int_{-\infty}^{\infty} dE \rho(E) [f_{FD}(E, \mu(t), T(t)) - f_{FD}(E, \mu_0, T_0)]$$

where $\rho(E) = \frac{2A_c}{\pi} \frac{|E|}{\hbar^2 v_F^2}$ with the unit cell area $A_c = \frac{3\sqrt{3}a^2}{2}$ and the lattice constant $a = 1.42 \text{ \AA}$. The equilibrium chemical potential $\mu_0 = -0.3 \text{ eV}$ was obtained from the high-resolution photoemission spectrum in fig. 5.1. The transient chemical potential is given by $\mu(t) = \mu_0 + \Delta\mu_{e(ED)}(t)$. The equilibrium temperature is $T_0 = T(t < 0 \text{ ps}) = 300 \text{ K}$.

It is found that a total number of $\sim 5 \times 10^{12}$ holes per cm^2 are transferred from WS₂ to graphene with an exponential lifetime of $1.5 \pm 0.2 \text{ ps}$ (fig. 5.6d).

5.3 Discussion

From the findings in figs. 5.3-5.6 the following microscopic picture for the ultrafast charge transfer in the WS₂/graphene heterostructure emerges (see sketches in fig. 5.7a and b). Photoexcitation of the WS₂/graphene heterostructure at 2eV dominantly populates the A-exciton in WS₂ (fig. 5.7a). Additional electronic excitations across the Dirac point in graphene as well as between WS₂ and graphene bands are energetically possible but considerably less efficient. The photoexcited holes in the valence band of WS₂ are refilled by electrons originating from the graphene π -band on a timescale short compared to the temporal resolution which explains the absence of a net pump-probe signal of the WS₂ valence band (fig. 5.4D) and the asymmetry between gain and loss in the pump-probe signal of the graphene π -band (fig. 5.4B and C). The photoexcited electrons in the con-

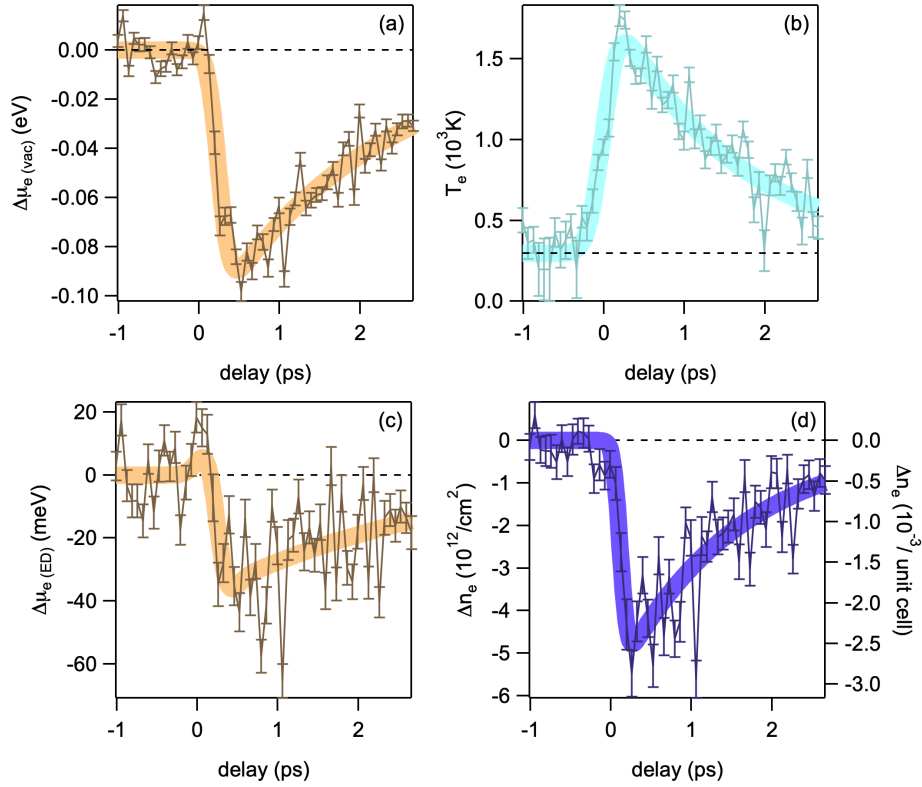


Figure 5.6: Result of Fermi-Dirac fits for graphene π -band. (a) Change of the chemical potential referenced to the vacuum level $\mu_{e(vac)}$ as a function of pump-probe delay. (b) Electronic temperature as a function of pump-probe delay. Thick lines in (a) and (b) are exponential fits with lifetimes of 2.0 ± 0.2 ps and 1.5 ± 0.1 ps, respectively. (c) Shift of the chemical potential referenced to the Dirac point $\mu_{e(ED)}$ obtained by subtracting the π -band shift from fig. 5.3b from $\mu_{e(vac)}$ in panel (a). (d) Change of the number of electrons in the π -band as a function of pump-probe delay together with exponential fit yielding a lifetime of 1.5 ± 0.2 ps.

duction band of WS_2 have a lifetime of $\sim 1\text{ps}$ (fig. 5.7b). However, it takes $\sim 2\text{ps}$ to refill the holes in the graphene π -band (fig. 5.7b). This indicates that, aside from direct electron transfer between the WS_2 conduction band and the graphene π -band, additional relaxation pathways — possibly via defect states [156] — need to be considered to understand the full dynamics.

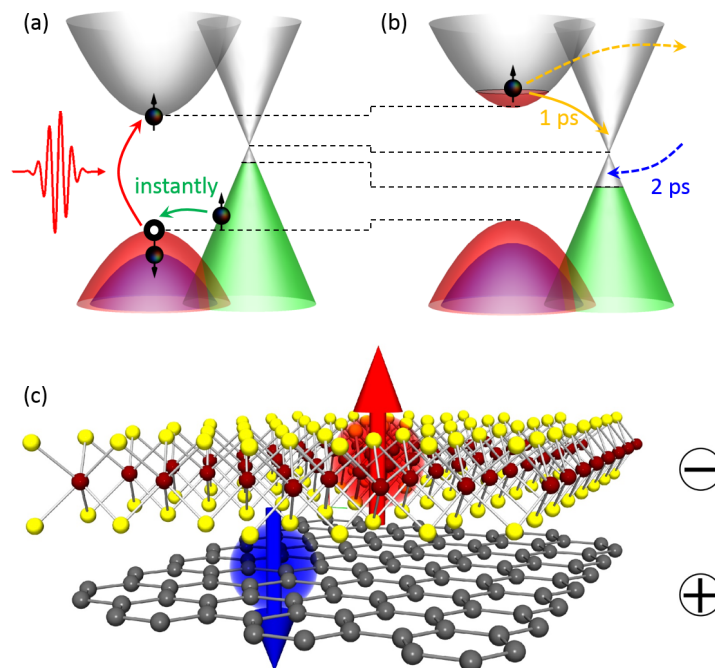


Figure 5.7: Sketch of ultrafast charge transfer deduced from tr-ARPES data. (a) Photoexcitation at resonance to the WS_2 A-exciton at 2eV injects electrons into the conduction band of WS_2 . The corresponding holes in the valence band of WS_2 are instantly refilled by electrons from the graphene π -band. (b) The photoexcited carriers in the conduction band of WS_2 have a lifetime of $\sim 1\text{ps}$. The holes in the graphene π -band live for $\sim 2\text{ps}$, indicating the importance of additional scattering channels indicated by dashed arrows. Black dashed lines in (a) and (b) indicate band shifts and changes in chemical potential. (c) In the transient state the WS_2 layer is negatively charged while the graphene layer is positively charged. For spin-selective excitation with circularly polarized light the photoexcited electrons in WS_2 and the corresponding holes in graphene are expected to show opposite spin polarization.

In the transient state after photoexcitation the photoinduced electrons reside in the conduction band of WS_2 while the photoinduced holes are located in the valence band of graphene (see sketch in fig. 5.7c). This means that the WS_2 layer is negatively charged and the graphene layer is positively charged. This accounts for the transient peak shifts reported in fig. 5.3 and the decrease of electron density in the graphene π -band (fig. 5.6d). The lifetime of this charge-separated state is $\sim 1\text{ps}$.

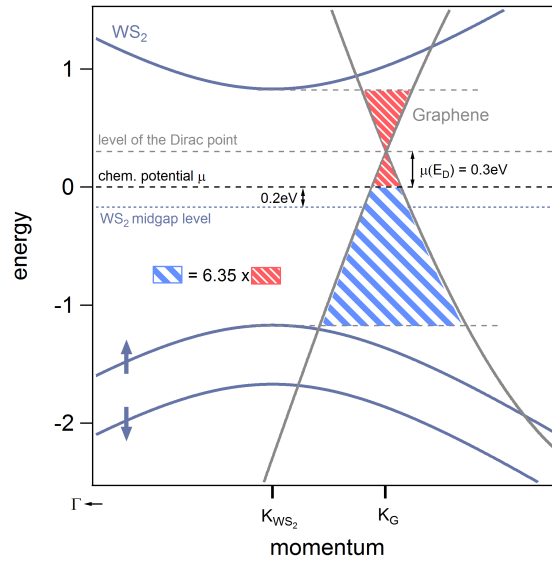


Figure 5.8: Scattering phase space for interlayer tunneling. The WS₂ and graphene band structures are shown in blue and gray, respectively. The number of available electronic final states for electron and hole transfer are illustrated by red and blue areas, respectively.

Similar charge-separated transient states were observed in related van-der-Waals heterostructures made up of two direct-gap semiconductors with type II band alignment corresponding to staggered band gaps [157–162]. After photoexcitation the electrons and holes were found to rapidly move to the bottom of the lower conduction band and to the top of the upper valence band, respectively, which are located in different layers of the heterostructure [157–162]. In this case, the charge-separated transient state has been attributed to a charge transfer exciton rather than a free electron-hole pair [157–162].

In the case of the WS₂/graphene heterostructure the energetically most favorable location for both electrons and holes is at the Fermi level in the metallic graphene layer. Therefore, one would expect that both electrons and holes rapidly transfer to the graphene π -band. However, the measurements clearly show that hole transfer (<200 fs) is much more efficient than electron transfer (~ 1 ps). This is attributed to the relative band alignment between WS₂ and graphene bands as revealed in fig. 5.1a that offers a larger number of available electronic final states for hole transfer compared to electron transfer (see fig. 5.8). Any deviation from the hypothetical case where both the equilibrium chemical potential and the Dirac point are located in the middle of the WS₂ band gap breaks electron-hole symmetry and thus favors either electron or hole transfer. In the present case, assuming a ~ 2 eV band gap, the Dirac point and equilibrium chemical potential are located ~ 0.5 eV above and ~ 0.2 eV above the middle of the WS₂ band gap, respectively. For that reason the number of available final states for hole transfer is ~ 6 times bigger than for electron

transfer which is why hole transfer is expected to be faster than electron transfer.

A complete microscopic picture of the observed ultrafast asymmetric charge transfer should, however, also consider the overlap between the orbitals that constitute the A-exciton wavefunction in WS₂ and the graphene π -band, respectively, different electron-electron and electron-phonon scattering channels including the constraints imposed by momentum, energy, spin, and pseudospin conservation, as well as the role of a possible displacive excitation of coherent phonon oscillations that might mediate the charge transfer [163, 164]. Also, one might speculate whether the observed charge transfer state consists of charge transfer excitons or free electron-hole pairs. As shown in fig. 2.15 in sec. 2.3.2 the samples consist of triangular WS₂ islands on top of the graphene layer with a total coverage of 40% and a spacing between WS₂ islands of 1 – 10 μm . Due to the extreme surface sensitivity of ARPES only the graphene layer in the areas where it is uncovered is probed. Furthermore, the trARPES measurements average over the area of the XUV spot with a diameter of $\sim 300\mu\text{m}$. From the fact that the pump-probe signal of the graphene π -band of the WS₂/graphene heterostructure is clearly different from the one of pure graphene (fig. 5.5) it is concluded that all or a significant part of the holes that are transferred from WS₂ to graphene are rapidly delocalized over the complete graphene layer. This infers free electron-hole pairs rather than charge transfer excitons. Further theoretical investigations that go beyond the scope of the current work are required to clarify these issues.

In summary, trARPES was used to study ultrafast interlayer charge transfer in an epitaxial WS₂/graphene heterostructure. It was found that, when excited at resonance to the exciton of WS₂ at 2eV, the photoexcited holes rapidly transfer into the graphene layer while the photoexcited electrons remain in the WS₂ layer. This is attributed to the fact that the number of available final states for hole transfer is bigger than for electron transfer. The lifetime of the charge-separated transient state is found to be $\sim 1\text{ps}$. In combination with spin-selective optical excitation using circularly polarized light [165–167] the observed ultrafast charge transfer might be accompanied by spin transfer. In this case, the investigated WS₂/graphene heterostructure might be used for efficient optical spin injection into graphene resulting in novel optospintronic devices.

CHAPTER 6

Practical Limitations of Floquet Topological Insulators

The experimental investigation described in this chapter is based on unpublished results.

6.1 Introduction

In 1988 F. D. M. Haldane introduced a model system, which gives rise to an anomalous quantum Hall effect in the absence of a magnetic field [168]. His model is based on the honeycomb lattice with complex next-nearest neighbor hopping elements which break the time-reversal symmetry of the system. By exploring different parameter regimes, he found that the transverse conductance becomes quantized as $\pm e^2/h$ when a band gap is introduced due to broken time-reversal symmetry, but stays zero if inversion symmetry is broken instead. A physical realization of the model, however, was believed to require magnetic ordering and seemed unlikely.

In the past years, a new route of activating novel states of matter has arisen in solid state physics. The concept, known as *Floquet engineering*, is based on driving a quantum system by external fields, or mechanically deforming it in a periodic fashion, in order to generate effective Hamiltonians hosting new quantum states which might even be unreachable in fabricated static systems [169] (see appendix D for some details on Floquet theory).

Applying the techniques of the Floquet formalism, Takashi Oka and Hideo Aoki predicted in 2009, that graphene, a topologically trivial material, undergoes a phase transition to a topological insulator when being subject to strong circularly polarized light [63] (see appendix A.3.5). This insulating phase serves as a true realization of the original Haldane model [168], it is predicted to host one-dimensional metallic edge-states and to give rise

to a half-integer quantum Hall effect in the absence of a magnetic field. However, the necessity for strong field strengths and long wavelengths make the physical realization of the Haldane model in graphene technically demanding.

Three different, complementary experimental methods serve as ideal pathways to demonstrate and prove a physical realization of the predicted *Floquet topological insulating* phase of graphene. Firstly, a photoinduced transport experiment would favorably show a quantized Hall conductance of $\pm e^2/h$ depending on the handedness of the circular polarization of the light. Secondly, trARPES serves as the best tool to verify predicted changes to the bandstructure. These include the stabilization of Floquet replica bands, also known as Floquet sidebands (see appendix D), and a gap opening at the Dirac point under circularly polarized light. A third, more indirect method was proposed in the form of an all optical pump-probe experiment by observing the Faraday effect induced by circularly polarized light in absence of a magnetic field [170].

The Haldane model has been observed in optical lattices [171] by a circular *shaking* of the lattice potential. Furthermore, a similar effect of the Floquet topological insulator in graphene has been observed with trARPES on the surface state of the topological insulator Bi_2Se_3 , where a band gap opening was found for circularly polarized light [172, 173]. Very recently, McIver et al. have observed a photoinduced Hall-effect in graphene in the absence of a magnetic field which shows several signatures that are consistent with Floquet predictions [174].

This study aims at confirming these indications with trARPES and providing further proof for the generation of the Haldane state in graphene. The main focus was to investigate under which circumstances Floquet replica bands can be created and comparing observed photoemission spectra with predictions from Floquet theory.

In the experiments, careful attention was paid on pulse durations and wavelengths in order to reach the so-called *Floquet limit*. Basic Floquet theory is built around a time-periodic Hamiltonian where the driving persists on an infinite timescale. Evidently, this condition is not fulfilled by pulsed pump lasers which are on the other hand required to achieve the necessary field strengths. However, in the limit of the following condition to the pulse durations and driving frequency the suitability of Floquet theory can be ensured nonetheless [175]:

$$\sigma_{\text{pump}} \gg \sigma_{\text{probe}} \gg T_{\text{pump}} \tag{6.1}$$

where σ_{pump} and σ_{probe} are the pulse durations of pump and probe, respectively, and T_{pump} represents the periodic time of the drive. As pump pulses represent the *infinite* time-periodic drive, they are required to provide the longest time-scales of all. Most importantly, for the stabilization of Floquet states, which are stationary states of the

time-periodic Hamiltonian, the pump pulse duration needs to cover many time periods of the drive. Furthermore, for the observation of quasi-static Floquet states, the experimental probing, which happens over the course of the probe pulse duration, also needs to cover several cycles of the drive, in order to avoid an observation of micromotions.

In the experiments, Floquet replica bands are observed for bulk WSe₂ (a transition metal dichalcogenide material), but not in graphene. A possible explanation lies in the much faster decoherence taking place in graphene, for shorter electron scattering times. The results reveal difficulties that need to be overcome for the realization of general theoretical predictions from the Floquet formalism. They demonstrate that more realistic Floquet model systems should be extended by taking in account heating effects, interactions and more.

6.2 Experiment

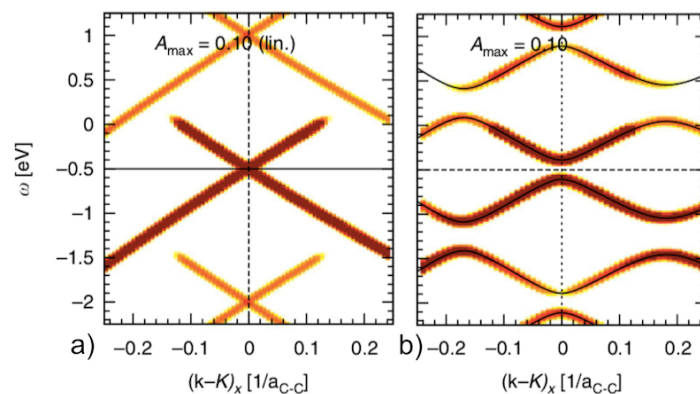


Figure 6.1: Simulated ARPES spectra of graphene under strong irradiation with linearly (a) and circularly (b) polarized light at 800nm wavelength from [175]. Floquet sidebands at pump photon energy $\hbar\omega = 1.55eV$ above and below the original Dirac bands appear. In the case of circular polarization, a non-trivial gap at the Dirac point is created and avoided crossings are induced.

In [175], simulations of a trARPES experiment on graphene being subject to a strong laser beam at 800nm wavelength (see fig. 6.1) were carried out. Here, the pump laser beam serves as the periodic driving mechanism of the system. Under linear polarization (fig. 6.1a), the appearance of Floquet sidebands is predicted (see appendix D for details). These side bands are caused by the coherent interaction of the electronic states and the photon field and appear in form of replica bands at the photon energy ($800nm \hat{=} 1.55eV$) above and below from the original bands. In the case of circularly polarized light, aside from side bands, the previously discussed topologically non-trivial band gap appears at

the Dirac point (fig. 6.1b), and avoided crossings arise at the points where the side bands would cross the original bands.

The aim of the current study is the observation of the theoretically-predicted spectra mentioned above. One main focus lies on observing Floquet sidebands, whose occurrence provide evidence for achieving the Floquet limit under the given experimental conditions. As a further step, the possibility of a band gap opening at the Dirac point is investigated, when using circularly polarized pump pulses. In contrast to the simulations, the pump laser wavelength was chosen in the mid-infrared spectral range, where the Floquet effects are predicted to be much stronger¹.

The experiments were carried out at the ARPES laboratory at the Max-Planck Institute for the Structure and Dynamics of Matter in Hamburg. Technical details of the setup are described in sec. 2.2.2. The experiment was designed as such to reach optimum settings for enhancing Floquet effects, i.e. long pump wavelengths, and ensuring that prospective sidebands can be distinguished from the main bands with the given energy resolution. The latter results in an upper limit to the pump wavelength. For pushing the barriers on this limitation, a slight modification to the HHG (see sec. 2.2.2) led to an improved bandwidth of XUV pulses. The resulting probe pulses at $\sim 21.97\text{eV}$ had pulse durations of $\sim 120\text{fs}$ and yielded an energy resolution of $\sim 140\text{meV}$ in the photoemission spectra.

This allowed to utilize pump pulses at a wavelength of $4.45\mu\text{m} \hat{=} 280\text{meV}$ with pulse energies of $\sim 5\text{-}20\mu\text{J}$ at the sample position. In order to ensure long pump pulse durations and reach the Floquet limit given by eq. 6.1, a CaF_2 lens was employed in the laser beam path for pulse stretching by introducing a chirp.

TDMLG samples were grown by the group of Camilla Colleti at Pisa, Italy, as described in section 2.3.1. Due to the silicon carbide substrate, these graphene samples are intrinsically n-doped with the chemical potential $\sim 0.4\text{eV}$ above the Dirac point. In addition, for comparison, bulk 2H-WSe₂ samples, which belong to the family of transition metal dichalgonides and posses an optical band gap of $\sim 1\text{eV}$, were investigated. The WSe₂ samples were grown by the group of Kai Roßnagel at the university of Kiel, Germany, as described in sec. 2.3.3.

¹It is noted that the color-code in fig. 6.1 is logarithmic, hence, the sidebands at realistic photon fluxes are barely visible at this wavelength. A set of experiments previously performed with pump photon energies at 800nm (not shown) did not display replica bands. The intensity of sidebands is predicted to be much stronger at longer wavelengths in the mid-infrared spectral range [176].

Floquet Sidebands vs. Laser-Assisted Photoemission

Floquet replica bands are also called photodressed states, since they appear due to the coherent coupling of photons to the electronic states of the solid. Photodressing is also known to occur due to the coupling of photons to photoelectrons. The second process, also known as the Volkov process or, alternatively, laser-assisted photoemission (LAPE), is described in sec. 2.2.4. For this experiment, it is of crucial importance to separate the two processes which appear in photoemission spectra identically in the form of sidebands with separations given by the photon energy. In the given experiment, the LAPE does not alter the electronic states of the solid, and is therefore unwanted.

In the given geometry, LAPE is completely suppressed when the polarization of the pump pulses is vertical (VP)². In that case, the pump electric field is perpendicular to the direction in which the photoemission occurs ($\vec{E}_{\text{pump}} \perp \vec{k}_f$), thus, leading to a vanishing LAPE coupling element (eq. 2.6 in sec. 2.2.4). However, in case of horizontal polarization (HP), LAPE sidebands are expected, since the polarization does allow for coupling between pump photons and photoelectrons ($\vec{E}_{\text{pump}} \cdot \vec{k}_f \neq 0$). The same holds for circular polarization (CP), for which the intensity of the LAPE sidebands is expected to be half³, as compared to the HP driving condition.

On the contrary, since the pump beam is impinged on the sample at normal incidence, the strength of the Floquet sidebands is expected to be independent of the polarization of the pump pulses.

Experimental Results

In a first set of experiments, bulk WSe₂ samples were investigated in view of Floquet and LAPE sidebands. For this purpose the photoinduced change of the bandstructure under vertical and horizontal pump polarization at 4.45 μm was measured. For negative time-delays, before the arrival of pump pulses, ARPES spectra show the spin-split valence band at the K point, as seen in the snapshot in fig. 6.2 at $t \ll 0$. Around the peak of the signal at $t=0$, the spectra show clear signatures of first order replica bands under both polarizations.

Figure 6.2 shows the respective spectra for vertical polarization where LAPE is prevented as argued above. The observed sidebands are therefore considered as pure Floquet-Bloch states.

²The pump beam is impinged on the sample approximately at normal incidence, thus, making s- and p-polarization ill-defined. LAPE and Floquet sidebands are therefore discussed in terms of vertical and horizontal polarization.

³in case of moderate field strengths and according to eq. 2.7

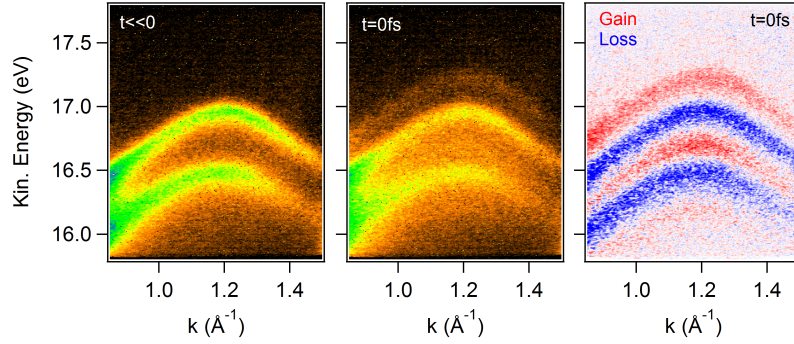


Figure 6.2: Bulk WSe₂ under irradiation with vertically polarized laser pulses at $4.5\mu\text{m}$: ARPES snapshot at negative time delays shows the fully occupied spin-split valence bands at the K-point. At the peak of the signal ($t=0\text{fs}$), first order Floquet replica bands are apparent.

By integrating the photo-current from 1.16\AA^{-1} to 1.23\AA^{-1} , energy distribution curves (EDCs) at the K point are obtained from the spectra (fig. 6.3b). Satisfactory fits to the data were achieved with 2 ($t<0$) or 5 ($t=0$) gaussians and a Shirley background. In these curves sidebands appear in terms of additional peaks above and below the original spin-split valence band states. The separation is consistent with the pump photon energy of $\hbar\omega=280\text{meV}$. The temporal evolution of the sideband's intensity, obtained by integrating the change in photocurrent at the emergent peak at 17.21eV , is shown in fig. 6.3b. The time trace follows a gaussian lineshape, thus, favoring the conclusion that the sidebands show no finite lifetime and only appear when the pump laser is present. The full width at half maximum of $397\text{fs}\pm 21\text{fs}$ of the fitted gaussian serves as a good estimate of the pump probe cross correlation. Under horizontal polarization, where the replica bands are expected to be a combination of Floquet and LAPE sidebands, the EDCs and the temporal evolution of the sidebands show qualitatively the same results.

The same set of experiments and analysis was carried out with n-doped graphene samples (TDMLG). All experimental parameters were kept unchanged from the measurements on WSe₂, including the pump laser wavelength, pulse duration, and fluence.

Starting out with horizontally polarized pump pulses where the LAPE is permitted, it was checked whether the energy resolution of the setup sufficed for resolving replicas of the highly dispersive π -bands of graphene. Fig. 6.4a shows respective ARPES snapshots from TDMLG samples. For $t\ll 0$, the spectra show the left branch of the Dirac spectrum while the other branch is dark due to the photoemission matrix element (see sec. 2.1.1). Around $t=0$, first order replica bands appear in the spectra. These arise as additional peaks in EDCs (light-gray lines in fig. 6.4b), best seen at the Fermi wavevector⁴. Additionally,

⁴The peaks at 17.29eV and at 17.68eV represent the conduction band and its first order sideband which occurs due to absorption of one pump photon. The low intensity peak at negative delays (black

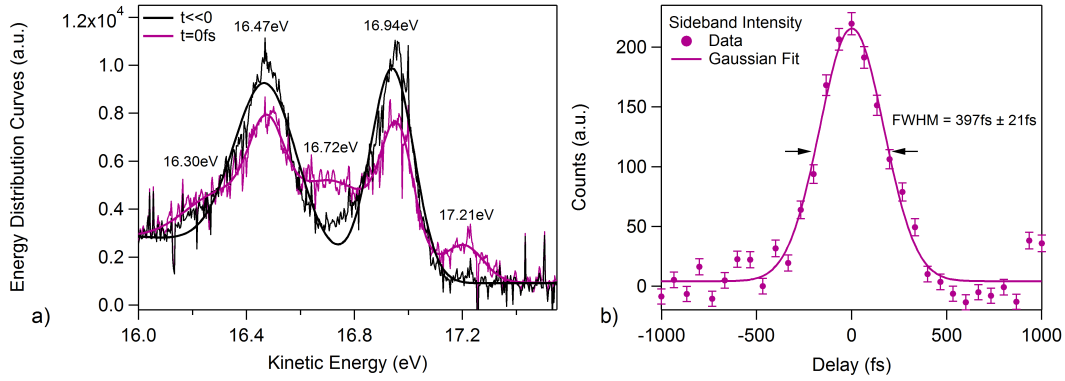


Figure 6.3: Bulk WSe₂ under irradiation of vertically polarized laser pulses at $4.5\mu\text{m}$: a) Energy distribution curves (EDCs) at $k \approx K$ show clear signatures of first order sidebands with separations consistent with the pump photon energy, b) Temporal evolution of the sideband's intensity (additional peak at 17.21eV in (a)) is given by the pump-probe pulse cross correlation.

heating of carriers is observed in the form of a thermalized hot carrier distribution. Since the pump photon energy does not exceed twice the doping level, the heating can be traced back to intraband free carrier absorption. While the sidebands are found to appear only while the pump pulse is present, the hot carriers persist after the excitation and show a decay behavior with similar timescales as observed in other studies [25–47].

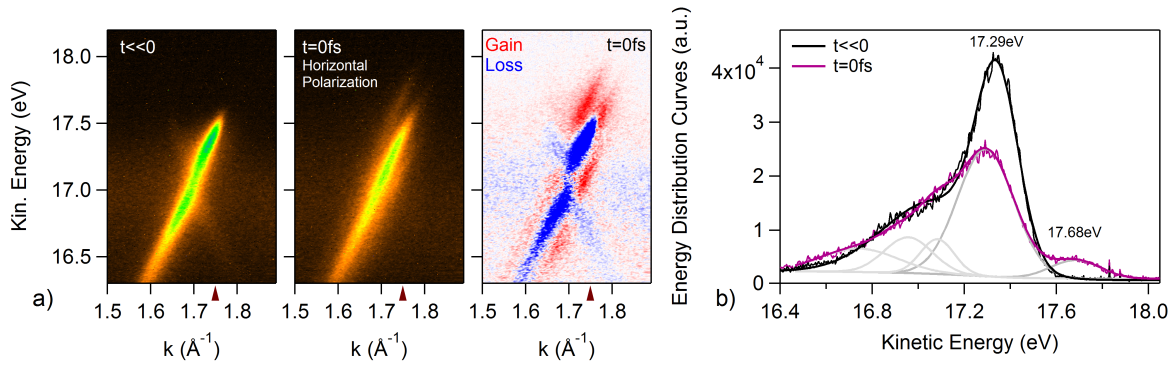


Figure 6.4: Graphene under irradiation of horizontally polarized laser pulses at $4.5\mu\text{m}$: a) ARPES snapshots and b) Energy distribution curves (EDCs) at $k \approx k_F$ indicated by triangles on the x-axis in (a): At the peak of the signal ($t=0\text{fs}$) first order replica bands are observed. Including a Shirley background, 5 individual gaussians are combined to fit the data at $t=0$ and are displayed in light-gray, representing main and replica electron states.

Fig. 6.5 shows the according spectra and EDCs in the case of vertically polarized pump

curve) represents the valence band of the (partly visible) *invisible* branch. The valence band state and various sidebands appear within a small energy window making a separation of all peaks within the range from $E_{kin} = 16.4\text{eV} - 17.2\text{eV}$ impossible.

pulses, corresponding to the situation where the LAPE mechanism is suppressed. In contrast to horizontal polarization, no sidebands are observed. A strong broadening of the equilibrium bands occurs during the presence of the pump pulses instead, hence, transient EDCs (fig. 6.5b) are characterized by broadened electronic states and show no indication of emergent replica states.

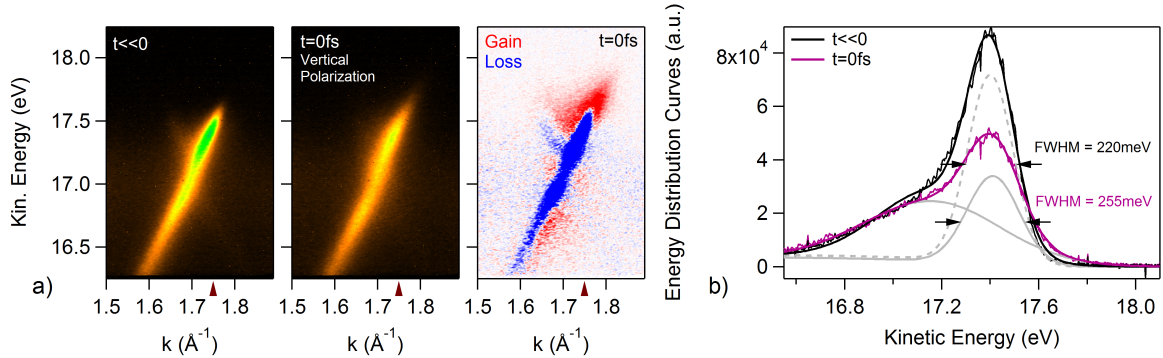


Figure 6.5: Graphene under irradiation of vertically polarized laser pulses at $4.5\mu\text{m}$: a) ARPES snapshots and b) Energy distribution curves (EDCs) at $k \approx k_F$ indicated by triangles on the x-axis in (a): At the peak of the signal ($t=0$ fs) broadening of Graphene π -bands is observed. Including a Shirley background, 2 individual gaussians are combined to fit the data at $t \ll 0$ and $t=0$ and are displayed in light-gray, representing the main electron states. Replica states are not observed.

Under circularly polarized pump pulses (fig. 6.6) a combination of the situations at horizontal and vertical polarization is observed. Broadening of bands and the appearance of sidebands are found to arise concurrently, but to a weaker extent than in the individual cases.

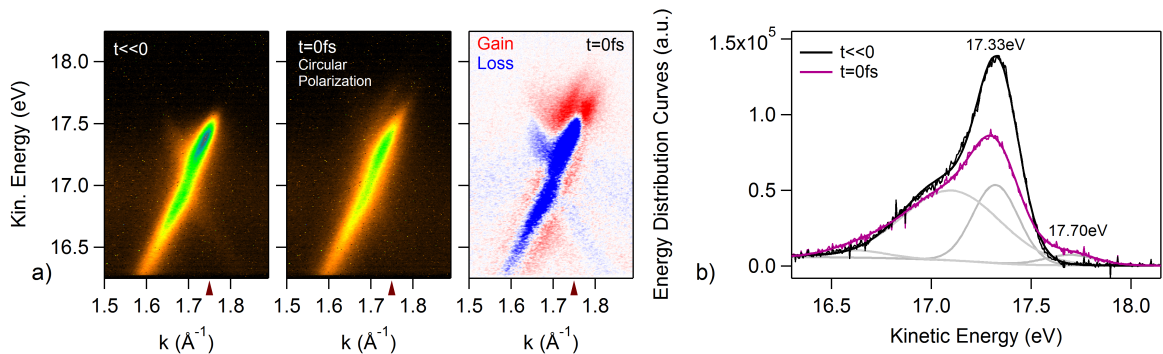


Figure 6.6: Graphene under irradiation of circularly polarized laser pulses at $4.5\mu\text{m}$: a) ARPES snapshots and b) Energy distribution curves (EDCs) at $k \approx k_F$ indicated by triangles on the x-axis in (a): At the peak of the signal ($t=0$ fs) a combination of first order replica bands and broadening of bands is observed. Including a Shirley background, 4 individual gaussians are combined to fit the data at $t=0$ and are displayed in light-gray, representing main and (combined) replica electron states.

The energy distribution curve at $k=K$ through the Dirac point is shown in fig. 6.7 and displays no indication for a band gap opening.

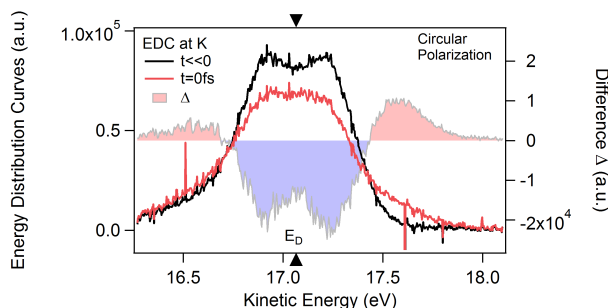


Figure 6.7: Graphene under irradiation of circularly polarized laser pulses at $4.5\mu\text{m}$: Energy distribution curves (EDCs) at $k \approx K$ show no sign of a gap opening within the energy resolution of $\sim 140\text{meV}$.

6.3 Discussion

The described experiments demonstrate the successful creation of Floquet-Bloch states in bulk 2H-WSe₂ by mid-infrared pump laser pulses with photon energies smaller than the band gap. Vertical polarization leads to complete suppression of the Volkov process (LAPE), establishing pure Floquet sidebands, while horizontal driving is found to generate a mixture of the two processes.

LAPE sidebands were created in n-doped epitaxial graphene samples under horizontal polarization. For vertical polarization, no sidebands were generated in graphene. Instead, broadening of the Dirac bands during the presence of the pump laser was observed. In graphene under irradiation with circularly polarized pump pulses, no sign for a gap opening was observed within the experimental energy resolution of $\sim 140\text{meV}$.

From the experimental observations it is concluded that no effects related to Floquet theory are taking place in the given graphene measurements. These results disclose limits to the applicability of Floquet theory.

One requirement for the validity of the Floquet formalism was already discussed in terms of eq. 6.1 and concerns the pulse durations of the laser pulses. These considerations were taken in account beforehand, the given timescales are $T = 14.8\text{fs}$, $\sigma_{\text{probe}} \sim 120\text{fs}$, and $\sigma_{\text{pump}} \sim 380\text{fs}$. It is noted that the pump pulse duration was estimated from the lifetime of the first order sideband in fig. 6.3b, which is interpreted as the pump-probe cross correlation.

From the successful creation and observation of Floquet sidebands in WSe₂, it is inferred

that the experimental requirements for reaching the Floquet limit were fulfilled. Thus, the electronic system itself is seemingly responsible for the the absence of Floquet effects in epitaxial graphene.

Several theoretical studies discussed limits when applying Floquet theory to realistic quantum systems. Interactions, which are typically neglected in Floquet simulations, are known to generate new terms in the high-frequency expansion [177]. Floquet theory is even more severely challenged due to decoherence by collisions. In the first study that introduces the concept of dynamical localization - an effect occurring in time-periodic systems that is well-understood within the Floquet formalism - the authors presume that the resulting impact is smeared out by collision, unless for long scattering times, fulfilling the condition: $\tau\Omega > 1$, where τ represents the collision or decoherence time and Ω the angular frequency of the drive.

It is assumed, that the appearance of Floquet effects in the WSe₂ can be explained by the fully occupied valence band, nonexistence of electron-hole pairs and therefore absence of dynamical effects on the electronic distribution function of any kind due to vanishing scattering phase space. In n-doped epitaxial graphene samples the scattering time of carriers⁵ is found to be $\tau \sim 60$ fs at room temperature. Due to the strong heating of the electronic system, as observed in the experiment, the scattering time is further reduced to the tens of fs range (see chapter 3 on thermalization dynamics and timescales), which can lead to decoherence on timescales shorter than even a single cycle of the driving field.

⁵Average electron scattering time $\langle \tau \rangle$, as obtained from Hall-conductance measurements in [178] following the Boltzmann relation for mobility and scattering time in monolayer graphene $\mu = ev_F^2 \langle \tau \rangle / E_F$ [179]

Concluding Remarks and Outlook

The experimental studies described in this work have been dedicated to the investigation of fundamental electron scattering dynamics in graphene and other two-dimensional materials. The majority of the investigations were performed with time- and angle-resolved photoemission spectroscopy (trARPES) - the ideal tool for tracking time dependent electronic distributions in energy and momentum. The trARPES technique provides a direct view on scattering channels of electrons in solids.

The described experiments gained new insights into the thermalization dynamics of photoexcited graphene (chapters 3 and 4) and WS₂/Graphene heterostructures (chapter 5). The experiment in chapter 6 revealed difficulties for the experimental realization of a theoretically predicted Floquet topological insulating phase in graphene, and proposed alternative approaches towards overcoming such constraints.

Proof for Auger Scattering and Dominance of Impact Ionization over Auger Recombination

Auger processes are two-electron scattering events where one electron switches from the conduction band to the valence band or vice versa and therefore leads to a change of the total number of electrons within individual bands. Auger processes, in particular impact ionization, are interesting from a technological standpoint because their occurrence can trigger carrier multiplication where a single photon leads to the generation of multiple electron-hole pairs. Carrier multiplication is expected to dramatically enhance the performance of graphene-based optoelectronic devices such as photodetectors, solar cells, and THz laser amplification.

The cross section of Auger processes in graphene is highly non-trivial and remains an

unresolved issue in theoretical physics. While energy and momentum conservation, in combination with the linear band structure, forces Auger scattering to only occur in a collinear fashion, the correct formal description that is required exceeds standard techniques. The most advanced theories existing so far follow the GW-RPA approach and predict a complete prevention of Auger processes by dynamical screening [51].

Based on estimates for the absorbed number of photons, two experiments claim the indirect observation of carrier multiplication [86, 87], indicating the occurrence of impact ionization and therefore Auger scattering in general. However, Auger processes in graphene remained disputable [51, 52], the occurrence is apparently highly susceptible to dynamical screening, which in turn depends on many parameters, such as static screening and the electronic distribution.

In the experiment presented in chapter 3 signatures for impact ionization were found, hence, providing further evidence for the occurrence of Auger scattering in graphene. Employing pulse compression, the shortest temporal resolution ($<10\text{fs}$) of a trARPES study performed on graphene up to date was achieved. This allowed observing the primary (intraband) thermalization dynamics of graphene. A simultaneous increase of the total number of electrons in the conduction band and decrease of the average kinetic energy of electrons in the conduction band were identified as a clear signature for impact ionization, inexplicable by any other scattering mechanism.

Besides proving the appearance of Auger events in general, the experimental results show that impact ionization dominates over Auger recombination during the first 30fs after photoexcitation in graphene.

Dominance of Collinear Scattering over Non-Collinear Scattering

Other two-electron scattering events in graphene are intraband and interband scattering. Both conserve the total number and average kinetic energy within individual bands. In contrast to Auger scattering, electron and momentum conservation allow scattering in any direction in two-dimensional k -space, i.e. permitting both collinear and non-collinear intraband and interband scattering.

Collinear scattering in graphene is subject to the so-called forward scattering resonance [48, 69] which can be understood as follows: due to the linear band dispersion, electrons that are moving in the same direction also move at the same velocity, which leads to infinite scattering time, thus, strongly enhancing the scattering cross section of forward scattering⁶. In contrast to Auger scattering where dynamical screening leads to a com-

⁶Collinear scattering includes forward scattering and backscattering. The forward scattering resonance does not apply to backscattering, in fact backscattering in graphene is prevented by pseudo-spin

plete cancelation of the scattering amplitude on the RPA level (as mentioned above), the forward-scattering cross section for intraband and interband scattering remains finite on the same level [51].

The experiment described in chapter 4 investigated the relative importance of collinear scattering (combining Auger scattering and collinear interband and intraband scattering) versus non-collinear scattering (combining non-collinear interband and intraband electron-electron scattering and electron-phonon scattering) by studying the relaxation dynamics of anisotropic electron-hole excitations. It was found that the staggering dominance of collinear scattering in graphene establishes a quasi-thermal equilibrium with anisotropic temperature. The effect can potentially be applied to the construction of polarization sensitive photodetectors and other optoelectronic devices.

Ultrafast Charge-Transfer in WS₂/Graphene Heterostructure

Heterostructures made up of a big variety of available two-dimensional materials such as graphene, hexagonal Boron-Nitride, and transition metal dichalcogenides (TDMCs) serve as promising building blocks for future technology in electronics and optoelectronics. Prototype devices such as field-effect transistors [151], photodetectors [11] and laser amplification stages [152] have been built in the past years.

In the experiment described in chapter 5, the relaxation dynamics of a photoexcited epitaxial WS₂/Graphene heterostructure grown on a SiC substrate was studied. With an excitation wavelength resonant to the WS₂ A-exciton, a fast interlayer charge transfer was observed. The resulting transient state with electrons remaining in the WS₂ conduction band and holes residing in the graphene π -bands shows a ~ 1 ps lifetime. The electron-hole-asymmetry of the interlayer transfer rate was attributed to the higher number of available electronic final states for hole transfer compared to electron transfer.

Difficulties with the Physical Realization of Floquet Topological Insulators

Graphene is predicted to undergo a phase transition to a topological insulator when being subject to irradiation with circularly polarized light, due to breaking of time-reversal symmetry [63]. The effect goes by the name of *Floquet topological insulator* and serves as a prominent example of the emerging field of *Floquet engineering*. The state which serves as a true realization of the well-known model system by F. D. M. Haldane [168], is characterized by a non-trivial band gap in the Dirac spectrum of graphene, one-dimensional metallic edge states and an anomalous quantum Hall effect in the absence of a magnetic

conservation.

field.

The effect has been observed in hexagonal optical lattices induced by circular *shaking* of the lattice potential [171]. A similar effect has been observed on the surface state of the topological insulator Bi_2Se_3 , where a band gap opening was found for circularly polarized light [172, 173]. The experimental proof for a (non-trivial) band gap opening in graphene is still missing.

The experiment in chapter 6 aimed at the observation of the *Floquet topological insulator* in graphene with trARPES induced by circularly polarized pump pulses in the mid-infrared spectral range. The main objective was the observation of a band gap opening at the Dirac point, additionally the stabilization of Floquet sidebands was investigated. While Floquet sidebands were observed in bulk WSe_2 , no Floquet effects were found in epitaxial monolayer graphene. The reason was attributed to fast decoherence, given by short electron scattering times in graphene which are comparable to the timescale of a single time period of the driving pump laser beam.

The study revealed general limitations for the physical realization of Floquet predictions in solid state systems which are commonly overlooked. The crucial requirement of long decoherence times translates to a grand demand for sample quality. The problem is particularly severe, when the periodic drive inevitably leads to electronic excitations, as it is the case in graphene.

Outlook on Future Research Directions

The experimental results from this work gave a few insights into the understanding of the dynamical properties of graphene and the $\text{WS}_2/\text{Graphene}$ heterostructure. There are still many open questions to the scattering mechanisms at work and further investigations are needed to clarify these questions. Some ideas for future experiments are listed here.

Unresolved Issue: Auger-Scattering vs. Other Collinear Electron-Electron Scattering Channels

While the experiments in chapter 3 and 4 reveal the dominance of collinear electron-electron scattering over non-collinear scattering of any kind, these experiments allow for no conclusion on the relative importance of Auger scattering (naturally collinear) versus collinear intraband and interband electron-electron scattering. The author is not aware of any study where this matter has been explored.

For technological perspectives, an enhancement of Auger scattering (impact ionization) or respectively weakening of collinear intraband and interband scattering would be of interest. For that purpose it is of fundamental interest to understand the mechanism that opens the Auger channels against the prevention by dynamical screening for which theoretical approaches beyond RPA are needed.

Manipulating Dynamical Screening and Electron-Plasmon Scattering

In contrast to past studies which mainly focused on the analysis of scattering processes in terms of phase space arguments, manipulating the dynamical screening is a new method for controlling scattering dynamics in graphene. A possible route for the modification of dynamical screening properties could be given by employing various pump photon energies and fluences in combination with different static doping and substrate dielectric screening. In order to fully understand the role of dynamical screening, it is also necessary to investigate electron-plasmon scattering further as both effects are very closely intertwined. Recent studies even suggest that plasmon emission has been underestimated in the relaxation dynamics of photoexcited graphene so far [53,54]. Following the plasmon dispersion, plasmon emission could particularly contribute to the decay of population inversion between the conduction and valence band.

In the pursuit of finding signatures for electron-plasmon scattering in the relaxation dynamics of photoexcited graphene, a trARPES study of highly doped ($\sim 1\text{eV}$) graphene is desirable: in these samples, high-resolution static ARPES measurements have already demonstrated strong electron-plasmon coupling in the form plasmon satellites in the band structure [111].

Further Experiments at Extreme Time-Scales (Sub 10fs Resolution)

In chapter 3 the primary thermalization dynamics of photoinduced electron-hole pairs has been investigated by trARPES with sub 10fs temporal resolution. Other experiments at such extreme timescales are tempting:

- **Subcycle dynamics of intraband absorption:** With pump photon energies $\hbar\omega < 2|\mu|$ interband absorption is prevented due to Pauli blocking. However, free electron intraband absorption occurs. With subcycle temporal resolutions, the intraband absorption mechanism could be studied. Observing an expected *sloshing* behavior of the electronic distribution induced by the oscillating pump electric field would additionally require Carrier Envelope Phase (CEP) stability. Such a sloshing behavior becomes particularly strong in the ballistic regime and was recently observed on the surface state of a topological insulator by using THz pump pulses and 100fs probe pulses [180]. In order to surpass the diffusive limit and achieve ballistic

charge accelerations in epitaxial graphene, pump wavelengths in the MIR spectrum and sub 10fs probe pulses are needed.

- **Observation of Rabi oscillations:** At high pump fluences Rabi oscillations are predicted in graphene [88]. Due to the decaytimes of excited electrons in the tens of femtosecond range, Rabi oscillations - whose frequencies are fluence dependent - only occur with fluences above $5\text{mJ}/\text{cm}^2$ and at sub 10fs periodic times in graphene [88].
- **Micromotions:** In the context of Floquet engineering, subcycle temporal resolution gives access to the opposite limit to the Floquet limit. This allows studying the subcycle micromotions which are *averaged out* when probing over many cycles in the Floquet limit⁷. A long term goal would be to study the microscopic buildup phase when stabilizing stationary Floquet states.

Charge-Transfer Exciton and Spin Injection in WS_2 /Graphene Heterostructure

The study of photoexcited WS_2 /graphene heterostructures (chapter 5) leaves many open questions: is the transient charge separation attributed to a charge transfer exciton or to free electron-hole pairs? Also the microscopic excitation and relaxation mechanism which results in the ultrafast charge transfer state is very unclear: do 2eV photons populate the intralayer exciton or free electron hole pairs within the WS_2 layer? How stable is the intralayer exciton in the presence of the graphene layer? What is the predominant charge transfer mechanism? Is the interlayer tunneling accomponied by electron-hole pair creation or phonon-emission? How do the constraints imposed by energy, momentum, spin, and pseudospin conservation, and a possible displacive excitation of coherent phonon oscillations [163, 164] influence the charge transfer?

In order to distinguish excitonic states from free electron-hole pairs and clarify their roles, a trARPES experiment with above gap excitation is planned by using pump photon energies of 3eV. Concerning the charge transfer mechanism, an experiment with better temporal resolution is desirable. Employing different fluences could potentially reveal microscopic scattering events which are responsible for interlayer tunneling.

By applying circular polarized pump pulses, the intralayer excitation is expected to be spin-polarized [165]. Hence, the ultrafast charge transfer might cause an ultrafast spin transfer from the WS_2 to the graphene layer allowing for efficient optical spin-injection into graphene. A spin-resolved trARPES study on the epitaxial WS_2 /graphene heterostructure

⁷see appendix D for details on Floquet theory, including the concept of micromotions.

was performed at the ARTEMIS facility in Harwell (UK) earlier this year. Technical difficulties and low count rates of the spin signal led to no interpretable results, repeating these measurements is highly desirable.

Overcoming Constraints for Floquet Engineering

Overcoming the decoherence problem for the observation of a Floquet topological insulator in graphene with trARBES seems challenging. The experimental parameters regarding the pulse durations and wavelength of the pump pulses have already been carefully chosen and are believed to be optimally placed. Some margin is believed to be given by further improving the energy resolution or replacing the epitaxial monolayer graphene by alternative more pristine graphene samples with longer free electron scattering times.

Alternatively, there are related proposals to initiate topological phase transitions in monolayer transition metal dichalcogenides (TMDCs) [181]. Photoinduced band inversion by the generation of Floquet sidebands in these systems is also predicted to generate conductive topologically protected chiral edge modes. The mechanism could be more feasible than in graphene as the decoherence time in semiconducting monolayer TMDCs is much longer⁸.

⁸The proposed mechanism from [181] could potentially suffer from decoherence due to inevitably created concurrent electron hole pairs which would lead to (accelerated) decoherence times by intraband relaxation. Due to the high pump photon energies needed for the effect, the constraint for coherence times is far less demanding since periodic times are of the order of only 2-3fs. The mechanism is however further challenged by a need for rather high pump fluences in order to create Floquet sidebands of required intensity at such short pump wavelengths.

Appendices

APPENDIX A

Details on Electronic Properties of Graphene

A.1 Tight-Binding Model of Graphene

The bandstructure of graphene, and therefore many of its extraordinary properties, is well described by a simple tight-binding approach taking into account only nearest-neighbor hopping. Since the honeycomb lattice of graphene consists of two atoms per unit cell, one can use Bloch's theorem and write down the eigenstates of the lattice Hamiltonian as linear combinations of atomic wavefunctions ($2p_z$ orbitals) on the two lattice sites.

$$\Psi^{\vec{k}} = \frac{1}{\sqrt{N}} \sum_j \left(e^{i\vec{k}\vec{R}_j^A} C^A(\vec{k}) \phi_{2p_z}(\vec{r} - \vec{R}_j^A) + e^{i\vec{k}\vec{R}_j^B} C^B(\vec{k}) \phi_{2p_z}(\vec{r} - \vec{R}_j^B) \right) \quad (\text{A.1})$$

where $\vec{R}_j^A = \vec{R}_j$, $\vec{R}_j^B = \vec{R}_j + \vec{\delta}_3$. Note that different basis exist, of how the the Blochwaves are constructed attributing different phase factors to the two sublattice Blochwaves [182]. Here the same basis as in the original paper by P. R. Wallace [64] is used.

The tight-binding Hamiltonian in second quantization reads:

$$H = -t \sum_{\langle i,j \rangle} (a_i^\dagger b_j + h.c.) \quad (\text{A.2})$$

where the Wannier operators a_i^\dagger and b_i^\dagger correspond to creating electrons on the sublattice A and B at sites \vec{R}_i^A and \vec{R}_i^B . Since we have a translational invariant system, it is a good idea to transform to momentum space ($a_i = \sum_{\vec{k}} \frac{1}{\sqrt{N}} e^{i\vec{k}\vec{R}_i} a_{\vec{k}}$). Defining $\hat{\psi}(\vec{k}) = (a_{\vec{k}}, b_{\vec{k}})^T$ the tight-binding Hamiltonian then reads:

$$H = \sum_{\vec{k}} \begin{pmatrix} a_{\vec{k}}^\dagger & b_{\vec{k}}^\dagger \end{pmatrix} \underbrace{\begin{pmatrix} 0 & f(\vec{k}) \\ f^*(\vec{k}) & 0 \end{pmatrix}}_{=h(\vec{k})} \begin{pmatrix} a_{\vec{k}} \\ b_{\vec{k}} \end{pmatrix} = \hat{\psi}^\dagger(\vec{k}) h(\vec{k}) \hat{\psi}(\vec{k}) \quad (\text{A.3})$$

where $f(\vec{k}) = -t \sum_{i=1..3} e^{i\vec{k}\vec{\delta}_i} = -t (e^{k_x a} + 2e^{ik_x a/2} \cos(k_y a \sqrt{3}/2)) \equiv |f(\vec{k})| e^{-i\phi(f(\vec{k}))}$ and h is called the Bloch Hamiltonian. There are two solutions to the single-particle Schroedinger equation $h(\vec{k})\vec{\psi}_\nu(\vec{k}) = \epsilon_\nu \vec{\psi}_\nu(\vec{k})$ with the eigenstates

$$\vec{\psi}_\nu(\vec{k}) = \frac{1}{\sqrt{2}} \begin{pmatrix} 1 \\ \nu e^{i\phi(f(\vec{k}))} \end{pmatrix} \quad (\text{A.4})$$

and respective eigenenergies

$$\epsilon_{\nu=\pm 1} = \nu |f(\vec{k})| = \nu t \sqrt{3 + 2 \cos(\sqrt{k_y a}) + 4 \cos(\frac{\sqrt{3}}{2} k_y a) \cos(\frac{3}{2} k_x a)} \quad (\text{A.5})$$

The two solutions correspond to the conduction band ($\nu = +1$) and valence band ($\nu = -1$), which form the tight-binding band structure (see fig. 1.1) as found by [64].

A.2 Low Energy Theory and Dirac Hamiltonian

As seen in fig. 1.1 the conduction and valence band touch at the K and K' points in the Brillouin zone. Since graphene (at neutral doping) has one electron per atom, taking in account spin-degeneracy, one finds that the valence band is exactly filled. For that reason, in cases where physics concerning only small excitations is taking place, the electronic excitations and all relevant processes happen close to the touching points at K and K'. For many practical purposes, it is sufficient to describe graphene by a low energy theory in the vicinity of the two valleys K and K'.

With \vec{k} -vectors close to the K-point, the Hamiltonian can be expanded. Rewriting $\vec{k} \rightarrow \vec{K} + \vec{k}$ and using $f(\vec{K} + \vec{k}) \approx \underbrace{-\frac{3ta}{2}}_{v_F} e^{i2\pi/3} (k_x - ik_y)$, absorbing the phase-factor in the operators, the Hamiltonian at K can be written as:

$$H(\vec{k}) = \hat{\psi}^\dagger(\vec{k}) h(\vec{k}) \hat{\psi}(\vec{k}) \quad (\text{A.6})$$

with the reduced Bloch Hamiltonian

$$h(\vec{k}) = v_F \vec{\sigma} \vec{k} = v_F k \begin{pmatrix} 0 & e^{-i\phi_k} \\ e^{i\phi_k} & 0 \end{pmatrix} \quad (\text{A.7})$$

with the Pauli matrix vector $\vec{\sigma} = (\sigma_x, \sigma_y)^T$ and $\hat{\psi}(\vec{k}) = (a_{\vec{K}+\vec{k}}, b_{\vec{K}+\vec{k}})^T$. In the same manner, the Bloch Hamiltonian at K' reduces to $h_{\text{K}'}(\vec{k}) = -v_F \vec{\sigma}^* \vec{k}$.

The low-energy Hamiltonian is equal to the two-dimensional version of the massless Dirac Hamiltonian, known from high-energy physics, and describes free relativistic fermions. The speed at which the electrons in graphene move, however, is about 300 times less than the actual speed of light. Graphene therefore exhibit several relativistic properties from this peculiar situation of its quasiparticles obeying to Dirac-physics. Some of the basic properties are listed here:

A.2.1 2D Dirac Equation and its Solutions

The single-particle Dirac equation reads:

$$h(\vec{k}) \vec{\Psi}(\vec{k}) = v_F \vec{\sigma} \vec{k} \vec{\Psi}(\vec{k}) = \epsilon(\vec{k}) \vec{\Psi}(\vec{k}) \quad (\text{A.8})$$

There are two solutions:

$$\vec{\Psi}_{\nu=\pm 1}(\vec{k}) = \frac{1}{\sqrt{2}} \begin{pmatrix} 1 \\ \nu e^{i\phi_{\vec{k}}} \end{pmatrix} \quad (\text{A.9})$$

With the energy-eigenvalues $\epsilon_{\nu} = \nu v_F k$ corresponding to upper and lower Dirac cone.

A.2.2 2D Dirac Equation in 2nd Quantization

Following the single-particle solution of the Dirac equation, the Dirac field operator can be written as:

$$\hat{\psi}(\vec{k}) = \begin{pmatrix} a_{\vec{k}} \\ b_{\vec{k}} \end{pmatrix} = \sum_{\nu=\pm 1} c_{\nu}(\vec{k}) \vec{\Psi}_{\nu}(\vec{k}) \quad (\text{A.10})$$

while $c_{\nu}^{\dagger}(\vec{k})$ and $c_{\nu}(\vec{k})$ are the creation and annihilation operator of a Dirac state in the upper ($\nu = +1$) or lower ($\nu = -1$) cone and $\vec{\Psi}_{\nu}(\vec{k})$ is given by eq. A.9.

The Hamiltonian then reads:

$$H(\vec{k}) = \hat{\psi}^{\dagger}(\vec{k}) h(\vec{k}) \hat{\psi}(\vec{k}) = \sum_{\nu=\pm 1} c_{\vec{k},\nu}^{\dagger} c_{\vec{k},\nu} \epsilon_{\nu}(\vec{k}) \quad (\text{A.11})$$

Following text-book calculations the bare Green's functions [183] (non-interacting case) of graphene in the low-energy expansion read as follows:

Bare retarded and advanced Green's function:

$$G_0^{R/A}(\epsilon, \vec{k}) = ((\epsilon \pm i0)1 - v_F \vec{\sigma} \cdot \vec{k})^{-1} = \underbrace{\frac{1 + \vec{\sigma} \hat{k}}{2}}_{P_+(\hat{k})} \frac{1}{\epsilon \pm i0 - v_F k} + \underbrace{\frac{1 - \vec{\sigma} \hat{k}}{2}}_{P_-(\hat{k})} \frac{1}{\epsilon \pm i0 + v_F k} \quad (\text{A.12})$$

bare lesser Green's function and spectral function:

$$G_0^<(\epsilon, \vec{k}) = i \sum_{\nu=\pm 1} P_\nu(\hat{k}) f(\epsilon) 2\pi \delta(\epsilon - \epsilon_\nu(\vec{k})) \quad (\text{A.13})$$

$$\mathcal{A}_0(\epsilon, \vec{k}) = 2\pi \sum_{\nu=\pm 1} P_\nu(\hat{k}) \delta(\epsilon - \epsilon_\nu(\vec{k})),$$

with the fermionic distribution functions $f(\epsilon)$. The Green's functions are written out in a convenient form where the 2D pseudo-spin texture (expressed by the sublattice indices $\alpha, \beta = A, B$ in $G_{\alpha, \beta}$) is separated from the analytical part. The entire pseudo-spin texture is expressed by $P_\nu(\hat{k}) = \vec{\Psi}_\nu(\vec{k}) \vec{\Psi}_\nu^*(\vec{k}) = \frac{1 + \nu \vec{\sigma} \hat{k}}{2}$.

A.2.3 Diagonalizing the Dirac Hamiltonian within the Chiral Basis

Following the tight-binding approach one naturally ends up in the basis where the 2D indices are given by sublattice indices $\alpha, \beta = A, B$. It can be useful to change the basis from the sublattice basis to a *chiral* basis where the 2D indices are replaced by cone-indices $\nu_1, \nu_2 = \pm 1$. The advantage is that in this basis the Hamiltonian becomes diagonal. The unitary matrix which diagonalizes the Hamiltonian is made up of the two eigenvectors:

$$U(\vec{k}) = \frac{1}{\sqrt{2}} \begin{pmatrix} 1 & 1 \\ e^{i\phi_k} & -e^{i\phi_k} \end{pmatrix} \quad (\text{A.14})$$

The Hamiltonian can be rewritten:

$$H(\vec{k}) = \hat{\psi}^\dagger(\vec{k}) h(\vec{k}) \hat{\psi}(\vec{k}) = \underbrace{\hat{\psi}^\dagger(\vec{k}) U}_{\tilde{\psi}^\dagger(\vec{k})} \underbrace{U^\dagger h(\vec{k}) U}_{\tilde{h}(\vec{k})} \underbrace{U^\dagger \hat{\psi}(\vec{k})}_{\tilde{\psi}(\vec{k})} \quad (\text{A.15})$$

In the new basis the Bloch Hamiltonian and the field operators are given by

$$\begin{aligned}\tilde{h}(\vec{k}) &= \begin{pmatrix} v_F k & 0 \\ 0 & -v_F k \end{pmatrix} \\ \tilde{\psi}(\vec{k}) &= \begin{pmatrix} c_{\nu=+1}(\vec{k}) \\ c_{\nu=-1}(\vec{k}) \end{pmatrix}\end{aligned}\tag{A.16}$$

Above, the sublattice operators $a_{\vec{k}}$ and $b_{\vec{k}}$ were expressed in terms of the Dirac operators $c_{\nu}(\vec{k})$. From the relation $\tilde{\psi}(\vec{k}) = U^\dagger \hat{\psi}(\vec{k})$ one finds the inverse relation:

$$c_{\nu}(\vec{k}) = \frac{1}{\sqrt{3}}(a_{\vec{k}} + \nu e^{-i\phi_{\vec{k}}} b_{\vec{k}})\tag{A.17}$$

In the chiral basis the bare Green's function become diagonal as well. The transformation is performed according to $\tilde{G} = U^\dagger G U$:

$$\tilde{G}_0^{R/A}(\epsilon, \vec{k}) = \delta_{\nu_1, \nu_2} \frac{1}{\epsilon - \epsilon_{\nu_1}(\vec{k}) \pm i0} = \begin{pmatrix} 1/(\epsilon - v_F k \pm i0) & 0 \\ 0 & 1/(\epsilon + v_F k \pm i0) \end{pmatrix}\tag{A.18}$$

$$\tilde{G}_0^<(\epsilon, \vec{k}) = i f(\epsilon) \begin{pmatrix} 2\pi\delta(\epsilon - v_F k) & 0 \\ 0 & 2\pi\delta(\epsilon + v_F k) \end{pmatrix}$$

$$\tilde{\mathcal{A}}_0(\epsilon, \vec{k}) = \delta_{\nu_1, \nu_2} 2\pi\delta(\epsilon - \epsilon_{\nu_1}(\vec{k})) = 2\pi \begin{pmatrix} \delta(\epsilon - v_F k) & 0 \\ 0 & \delta(\epsilon + v_F k) \end{pmatrix}$$

A.3 Topology of Graphene and other 2D Dirac Systems

Topology is a well-established branch of mathematics which deals with global properties of geometrical objects which are preserved under continuous deformations such as stretching and bending, but not tearing or gluing. The concepts can be applied to band theory of solid state physics which has implications on the physical properties of materials and can cause effects which are a result of the topological property of its band structures. One example is the (integer) quantum Hall effect, discovered in 1980 [184]: The quantized Hall conductance of 2D electron gases at low temperatures is a result of topological ordering.

During the last decade, there has been a growing interest in materials which inherit topologically non-trivial electronic bands. Topological insulators such as Bi_2Se_3 are three-dimensional insulators with non-trivial topology due to band-inversion stemming from

strong spin-orbit coupling. Non-trivial means that the topology is different from the vacuum surrounding the bulk material. This implies the existence of metallic spin-polarized edgestates on the two-dimensional surface of the crystal.

Graphene's topological properties are a consequence of the electrons behaving like Dirac fermions in the low-excitation regime. Massless Dirac fermions are known to be chiral, they have well-defined helicity which are opposite for the particle and the antiparticle states. The Dirac point, the touching point of the two cones, serves as a topological defect with four-fold degeneracy due to valley and spin degeneracy. The topological properties of Dirac fermions in combination with the linear spectrum give rise to an anomalous quantum Hall effect [155, 185]. The existence of a zero-energy Landau level leads to a "half-integer" quantization of the Hall conductivity, instead of an "integer" quantization [186]. The concept of pseudo-spin can be applied to graphene, which has consequences for electron-electron scattering (see sec. 1.2.1), including Klein tunneling through potential barriers, but also to photoemission cross sections (see sec. 2.1.1).

The persistence of the Dirac point, in other words, the absence of a band gap, is very rigid because it is protected by symmetry. Graphene's Hamiltonian is symmetric under parity (inversion) operation and time-reversal operation. As long as both are present, any perturbations, these could be many body interactions, defects, electron-phonon scattering, are not able to open a band gap.

A.3.1 Details on Pseudo-Spin of Graphene

As shown in section A.2, graphene's electron in the low-excitation regime are described by 2D massless Dirac fermions. For that reason they behave like relativistic spin $\frac{1}{2}$ -particles. While graphene electrons are degenerate in respect of the actual spin - spin-orbit coupling is known to be very weak - the "effective" spin of the quasi-particles arising from the Dirac equation is called pseudo-spin. In this section the origin and the property of the pseudo-spin will be discussed and a physical meaning for it will be given.

Pseudo-Spin in the Vicinity of the Dirac Points

The low-energy single-particle Schroedinger equation was given in eq. A.8. The respective eigenstates (eq. A.9) are called spinors, for their property of describing a spin- $\frac{1}{2}$ particle. The pseudo-spin operator is given by the sigma matrices $\hat{s} = \frac{\hbar}{2}(\sigma_x, \sigma_y, \sigma_z)^T$. Furthermore, the helicity is given by the projection of the pseudo-spin onto the direction of momentum $\hat{h} = \hat{s} \cdot \hat{k}$. In case of spin- $\frac{1}{2}$ particles, the helicity can either be $\pm\hbar/2$. Clearly, the

Hamiltonian, given by $h = v_F \vec{\sigma} \vec{k}$ commutes with \hat{h} making the helicity a good quantum number. One can easily show that

$$\hat{h} \vec{\Psi}_\nu(\vec{k}) = \nu \frac{\hbar}{2} \vec{\Psi}_\nu(\vec{k}). \quad (\text{A.19})$$

It becomes evident that the pseudo-spin is coupled to the Dirac state of the electron. In fact it points in the direction of the k-vector away from the Dirac point in case of the conduction band ($\nu = +1$) and towards the Dirac point in case of the valence band ($\nu = -1$). It is instructive to build spin- $\frac{1}{2}$ states with the help of the Bloch-sphere concept. The Bloch-state corresponding to a spin pointing in the direction $\hat{n} = (\sin \theta \cos \phi, \sin \theta \sin \phi, \cos \theta)^T$ is given by:

$$|\psi\rangle = \begin{pmatrix} \cos(\theta/2) \\ e^{i\phi} \sin(\theta/2) \end{pmatrix} = \cos(\theta/2) \Psi_A(\vec{k}) + e^{i\phi} \sin(\theta/2) \Psi_B(\vec{k}) \quad (\text{A.20})$$

where the Bloch state has been written out explicitly in the form of the Bloch waves on the two sublattices. The respective sublattice Blochwaves $\Psi_{A/B}(\vec{k})$ were defined in eq. A.1. The physical meaning of the pseudo-spin becomes evident: while the in-plane direction of the pseudo-spin leads to a phase-factor $e^{i\phi}$ between the two Bloch waves on sublattice A and B, the out-of plane component leads to a weighting factor in between the two Bloch waves. Pseudo-spin pointing to the north pole ($\hat{n} = \hat{e}_z$) corresponds to an electron living only on sublattice A, while pseudo-spin pointing to the south pole ($\hat{n} = -\hat{e}_z$) corresponds to an electron living only on sublattice B. As the eigenstates to the 2D Dirac equation are only given by spinors with pseudo-spin pointing in-plane, the electronic states in equilibrium graphene always correspond to Bloch waves with equal contribution on the two sublattices.

Pseudo-Spin over the whole Brillouin Zone

Away from the Dirac point the helicity is not a good quantum number anymore, the pseudo-spin therefore is not locked to the direction of the k-vector in respect to the K and K' points anymore. However, the concept of the pseudo-spin can be applied in a more abstract form to the whole Brillouin zone of graphene, far away from the K and K' points, where the electrons don't behave like Dirac electrons anymore. In fact, the pseudo-spin concept can be applied to any 2-component wavefunction.

Any (2x2) Hamiltonian¹ can be expressed in terms of $h = h_x \cdot \sigma_x + h_y \cdot \sigma_y + h_z \cdot \sigma_z = |h| \hat{h} \vec{\sigma}$.

¹The σ -matrices don't form a complete basis set for hermitian (2x2) matrices. For the discussion a possible diagonal term $h_i \hat{I}$ has been neglected for the Hamiltonian. The presence of such a term would lead to energy bands $\epsilon = h_i \pm \sqrt{h_x^2 + h_y^2 + h_z^2}$, and would therefore not change the energy difference of

With $\hat{h} = (\sin \theta \cos \phi, \sin \theta \sin \phi, \cos \theta)^T$ the 2D eigenstates take the form of spinors: $|u_{+1}\rangle = (\cos \frac{\theta}{2}, \sin \frac{\theta}{2} e^{i\phi})^T$ (conduction band) and $|u_{-1}\rangle = (\sin \frac{\theta}{2}, -\cos \frac{\theta}{2} e^{i\phi})^T$ (valence band), which correspond to pseudo-spins pointing in the direction of \hat{h} and $-\hat{h}$. The respective eigenenergies are $\epsilon = \pm |h| = \pm \sqrt{h_x^2 + h_y^2 + h_z^2}$.

In graphene, at equilibrium, where inversion and time-reversal symmetry are present, the tight-binding Hamiltonian only consists of h_x and h_y terms. The pseudo-spin of graphene at equilibrium is therefore pointing purely within the x-y-plane, implying that all electronic states have equal contribution on the two sublattices. This is reasonable since the sublattices are equal, thus no energetic preference for either one is given.

From the eigenstates of the tight-binding Bloch Hamiltonian (eq. A.4) one can read off that the in-plane direction of the pseudo-spin is directly set by the k-dependent phase factor $\phi(f(\vec{k})) = -\arg(f(\vec{k}))$.

As pointed out in [182], the pseudo-spin direction is not unique, it depends on the choice of the basis for how Bloch states are constructed. Different basis acquire additional phasefactors in $\phi(f(\vec{k}))$. The pseudo-spin direction plotted over the whole Brillouin zone in fig. 1.3 uses the same basis which was used in the paper by Wallace on the band structure of graphite [64].

A.3.2 Berry-Phase and Berry Curvature

The most elegant view on the origin of topological effects is probably based on the concept of Berry phase. To large extents, simple band theory is very successful in describing electronic properties of materials. Disregarding the nature of the eigenstates, the band dispersion alone governs the way quasiparticles interact, scatter and move within that band structure. It was until 1984 when Michael Berry realized that electrons acquire an additional non-zero geometrical phase, when electrons are driven through parameter space which depends on the property of the eigenstates themselves [187]. Since then it was gradually realized that this geometrical phase, now going by the name of Berry phase, can have profound effects on material properties and is responsible for a wide range of phenomena, such as orbital magnetism, various quantum, anomalous, or spin Hall effects, and quantum charge pumping [188].

Following the original paper by Berry [187] and the review article in [188] a brief introduction of Berry phase and the closely related Berry connection and curvature will be given, focusing on the special case of two-dimensional two-level systems:

the two bands.

In general, a Hamiltonian is considered which depends on time through an arbitrary set of parameters (R_1, R_2, \dots) that are here chosen to be the in-plane k-vectors $\vec{k} = (k_x, k_y)$, so that $h = h(\vec{k}(t))$. The Berry phase arises during the adiabatic evolution of a quantum state when it is moved slowly along a path C in parameter space. For this purpose it is useful to introduce an instantaneous orthonormal basis of eigenstates $|u_n(\vec{k})\rangle$ at each value of the parameters, which are the solutions to the time-independent Schroedinger equation:

$$h(\vec{k})|u_n(\vec{k})\rangle = \epsilon_n|u_n(\vec{k})\rangle \quad (\text{A.21})$$

According to the quantum adiabatic theorem, preparing the system initially in one eigenstate $|u_n(\vec{k}(t=0))\rangle$ it will stay as an instantaneous eigenstate of the varying Hamiltonian throughout the process. It will however acquire a phase. Being subject to the time-dependent Schroedinger equation

$$h(\vec{k}(t))|\Psi_n(\vec{k}(t))\rangle = i\partial_t|\Psi_n(\vec{k}(t))\rangle \quad (\text{A.22})$$

it is found that the state at a given time t and position $\vec{k}(t)$ reads

$$|\Psi_n(t)\rangle = e^{i\gamma_n(t)} e^{-\frac{i}{\hbar} \int_0^t dt' \epsilon_n(\vec{k}(t'))} |\Psi_n(\vec{k}(t))\rangle \quad (\text{A.23})$$

The second exponential is known as the dynamical phase factor. The first exponential is an additional geometrical phase that the state acquired during the adiabatic evolution. Inserting the state into the time-dependent Schroedinger equation and multiplying it with $\langle \Psi_n(\vec{k}(t)) |$ from the left, one finds that it can be expressed as a path integral in parameter space (see eq. A.24). This geometrical phase is not gauge invariant. Attributing phase factors to the eigenstates $|u_n(\vec{k})\rangle \rightarrow e^{i\xi(\vec{k})}|u_n(\vec{k})\rangle$ the geometrical phase yields arbitrary numbers, which is the reason why this phase has usually been neglected in theoretical time-dependent calculations. The situation changes for closed loops in parameter space where $\vec{k}(T) = \vec{k}(t=0)$. For a closed path the geometrical phase becomes an invariant since the requirement for single-valuedness fixes the gauge, i.e. the phase choice of the eigenstates is fixed up to integer value of 2π .

Definition of Berry phase:

$$\gamma_n \equiv \oint_C d\vec{k} \cdot \underbrace{i\langle u_n(\vec{k}) | \nabla_{\vec{k}} | u_n(\vec{k}) \rangle}_{\equiv A_n(\vec{k})} = \iint_S d\vec{S} \cdot \underbrace{\left(\nabla_{\vec{k}} \times A_n(\vec{k}) \right)}_{\equiv \vec{\Omega}_n(\vec{k})} \quad (\text{A.24})$$

The (gauge-dependent) integrand of the Berry phase is called Berry connection $A_n(\vec{k})$. Using Stokes theorem the path-integral can alternatively be expressed as a surface integral

over the curl of the Berry connection, also called the Berry curvature, $\vec{\Omega}_n(\vec{k})$, which is a gauge-independent local property of a material (k -dependent). In the case of two-levels ($n = \nu = \pm 1$), the Berry curvature can also be rewritten in a more convenient form:

$$\vec{\Omega}_\nu = 2\nu \text{Im} \left(\frac{\langle u_{-1}(\vec{k}) | \partial_{k_x} h(\vec{k}) | u_1(\vec{k}) \rangle \langle u_1(\vec{k}) | \partial_{k_y} h(\vec{k}) | u_{-1}(\vec{k}) \rangle}{(\epsilon_1(\vec{k}) - \epsilon_{-1}(\vec{k}))^2} \right) \hat{e}_{k_z} \quad (\text{A.25})$$

A.3.3 Massless Dirac System

The tight-binding Hamiltonian of graphene with nearest and second nearest neighbor hopping² is invariant under the time-reversal and inversion symmetry operation. Any gap opening term is forbidden by the presence of the two symmetries, and the Dirac points, i.e. the touching points at K and K', are topologically stable (detailed discussion can be found in [189]).

In the vicinity of the Dirac points at K and K', the graphene Hamiltonian reduces to Dirac equations. In compact form the Hamiltonian in first quantization reads:

$$h = v_F(\tau_z \sigma_x k_x + \sigma_y k_y) \quad (\text{A.26})$$

where $\tau_z = \pm 1$ for K and K' respectively³. Written out explicitly

$$\begin{aligned} \text{K:} \quad & h = v_F \vec{\sigma} \cdot \vec{k} = v_F k \begin{pmatrix} 0 & e^{-i\phi_{\vec{k}}} \\ e^{i\phi_{\vec{k}}} & 0 \end{pmatrix} \\ \text{K':} \quad & h = -v_F \vec{\sigma}^* \cdot \vec{k} = v_F k \begin{pmatrix} 0 & -e^{i\phi_{\vec{k}}} \\ -e^{-i\phi_{\vec{k}}} & 0 \end{pmatrix} \end{aligned} \quad (\text{A.27})$$

The eigenstates are given by

²The second nearest neighbor-hopping leads to a term $t_q \sum_{i=1}^6 e^{i\vec{k} \cdot \vec{d}_i} \hat{I}_{2 \times 2}$. This term preserves time-reversal and inversion symmetry, and does not correspond to a mass term σ_z .

³In literature other forms of the Hamiltonian at K' can be found, e.g. $h = v_F \vec{\sigma}^* \vec{k}$ or $h = -v_F \vec{\sigma} \vec{k}$. These are obtained by absorbing different phasefactors in the Wannier state creation operators a^\dagger, b^\dagger leading to different directions of the pseudo-spin (see [182] for details on how different constructions of the Bloch waves lead to phasefactors in the pseudo-spin). The Hamiltonian above is obtained when absorbing the phasefactors in a^\dagger, b^\dagger consistently at K and K'.

$$\begin{aligned}
\text{K:} \quad & |u_\nu(\vec{k})\rangle = \frac{1}{\sqrt{2}} \begin{pmatrix} 1 \\ \nu e^{i\phi_k} \end{pmatrix} \\
\text{K':} \quad & |u_\nu(\vec{k})\rangle = \frac{1}{\sqrt{2}} \begin{pmatrix} 1 \\ -\nu e^{-i\phi_k} \end{pmatrix}
\end{aligned} \tag{A.28}$$

with respective eigenenergies $\epsilon_{\nu=\pm 1} = \nu v_F k$, forming a gapless Dirac spectrum. The respective pseudo-spins of the eigenstates are shown together with the energy spectrum in fig. A.1. Note that the pseudo-spins are identical to the ones in fig. 1.3 at the vicinity of the Dirac points.

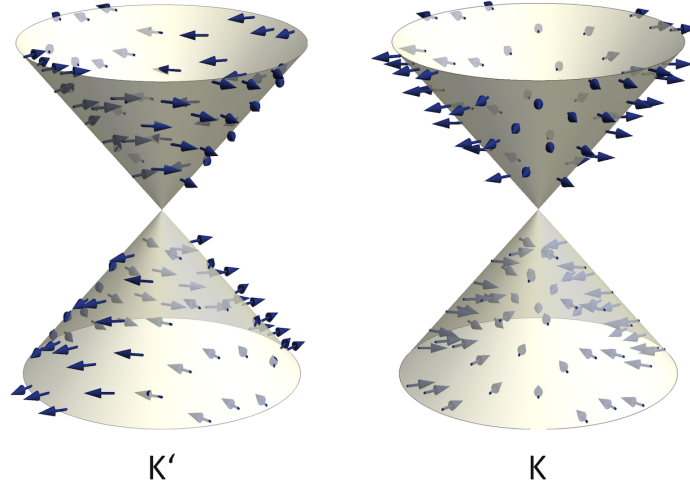


Figure A.1: Dirac cones at K and K': The pseudo-spin, shown by the arrows, point purely in the x-y-plane.

The topological property of the Dirac points can be characterized by the respective Berry phase when forming a loop around each of the Dirac points individually. With $\partial_{\phi_k} |u_\nu^K\rangle = \frac{i}{\sqrt{2}}(0, \nu e^{i\phi_k})^T$ and $\partial_{\phi_k} |u_\nu^{K'}\rangle = \frac{-i}{\sqrt{2}}(0, -\nu e^{-i\phi_k})^T$ and according to eq. A.24 the Berry phase is given by

$$\begin{aligned}
\text{K:} \quad & \gamma_\nu = i \int_0^{2\pi} d\phi_k \langle u_\nu | \partial_{\phi_k} | u_\nu \rangle = \frac{i^2 \nu^2}{2} \int_0^{2\pi} d\phi_k = -\pi \bmod 2\pi = \pi \\
\text{K':} \quad & \gamma_\nu = \frac{-i^2 \nu^2}{2} \int_0^{2\pi} d\phi_k = \pi \bmod 2\pi = \pi
\end{aligned} \tag{A.29}$$

Both Dirac points therefore exhibit a non-trivial Berry phase of π . Clearly, the Berry phase surrounding the full Brillouin zone on the other hand, enclosing both Dirac points,

yields a trivial Berry phase $\gamma_\nu = 0$, as the two parts cancel each other ⁴.

The topological properties of the system can also be characterized by the Berry curvature, which is a local property in k -space. According to eq. A.25 the Berry curvature is found to be zero everywhere in the Brilluin zone. Formally the Berry curvature possesses infinitesimal δ -peaks at the K and K' points of magnitude $\pm\pi$, which have opposite sign for the conduction and valence band (see fig. A.2), and give rise to Berry phases of π enclosing individual Dirac points [190]. Since conduction and valence band touch at the K and K' points the δ -functions of each band add up to zero.

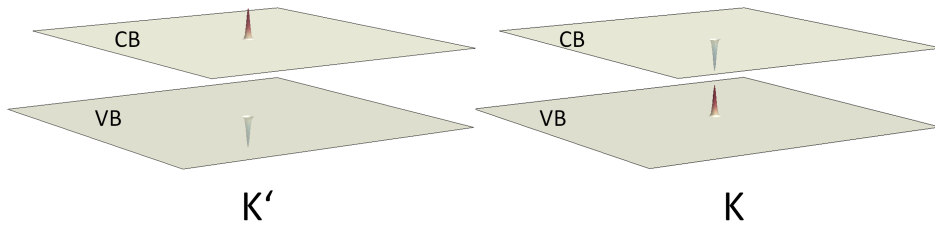


Figure A.2: Berry curvature for the conduction band (CB) and valence band (VB): The Berry curvature is zero everywhere except for sharp Delta-peaks $\pm\pi\delta(\vec{k} - \vec{K}^{(\prime)})$ at the K and K' points. Since CB and VB coincide at these points and signs are opposite, they cancel each other out.

The topological defects, characterized by non-trivial Berry-phases of π at individual valleys, cancel each other out, ending up with trivial Berry phase of zero surrounding the full Brillouin zone. Graphene (at equilibrium) therefore has the same topology as vacuum, and is therefore considered a topologically trivial material.

A.3.4 Honeycomb Lattice with Broken Inversion Symmetry

The easiest way to break the inversion symmetry of the honeycomb lattice tight-binding Hamiltonian is by introducing a mass term $m\sigma_z$, which is equal to breaking the sublattice symmetry of the system. This Hamiltonian gives an accurate description of hexagonal Boron Nitride (hBN) and the whole class of transition metal dichalcogenides (TMDC); other 2D materials, which have been extracted shortly after the first synthesis of graphene. These materials possess the same, or in case of the TMDC's similar hexagonal lattice structure as graphene, with the crucial difference that the two sublattices are made up of different atoms.

⁴The Berry phase is only defined modulo 2π . A Berry phase of π and $-\pi$ cannot be distinguished since the eigenstates can always be multiplied by phasefactors, preserving single-valuedness on the loop, and yielding an additional geometrical phase of 2π . For instance another choice for an eigenstate at K would be $\frac{1}{\sqrt{2}}(e^{-i\phi_k}, \nu)^T$ which would yield a phase of π instead of $-\pi$.

At the vicinity of the Dirac points at K and K', the tight-binding Hamiltonian of a honeycomb lattice system with broken sublattice symmetry reduces to Dirac equations with a mass term $m\sigma_z$:

$$h = v_F(\tau_z\sigma_x k_x + \sigma_y k_y) + \frac{\Delta}{2}\sigma_z \quad (\text{A.30})$$

The eigenstates of the conduction band ($\nu = +1$) and valence band ($\nu = -1$) read

$$\begin{aligned} \text{K:} \quad & |u_{\nu=+1}(\vec{k})\rangle = \begin{pmatrix} \cos \frac{\beta}{2} \\ \sin \frac{\beta}{2} e^{i\phi_k} \end{pmatrix} & |u_{\nu=-1}(\vec{k})\rangle = \begin{pmatrix} \sin \frac{\beta}{2} \\ -\cos \frac{\beta}{2} e^{i\phi_k} \end{pmatrix} \\ \text{K':} \quad & |u_{\nu=+1}(\vec{k})\rangle = \begin{pmatrix} \cos \frac{\beta}{2} \\ -\sin \frac{\beta}{2} e^{-i\phi_k} \end{pmatrix} & |u_{\nu=-1}(\vec{k})\rangle = \begin{pmatrix} \sin \frac{\beta}{2} \\ \cos \frac{\beta}{2} e^{-i\phi_k} \end{pmatrix} \end{aligned} \quad (\text{A.31})$$

with respective eigenenergies $\epsilon_\nu = \nu\sqrt{(\frac{\Delta}{2})^2 + v_F^2 k^2}$ forming the energy spectrum of a Dirac particle with non-zero rest mass $m = \Delta/2$. The angle β is defined by $\tan \beta = \frac{v_F k}{\Delta/2}$ restricted to the range $0 \leq \beta \leq \pi$. The respective pseudo-spin vectors of the eigenstates are shown in fig. A.3. While the in-plane pseudo-spin components are unchanged to the ones of graphene in fig. A.1 and fig. 1.3, they additionally obtain a z-component which is maximum at the Dirac point and become smaller when going further away from them. Within the valence band the z-component of the pseudo-spin is exclusively negative, corresponding to a larger B-sublattice content of the valence band eigenstates, while the situation is exactly switched for the conduction band.

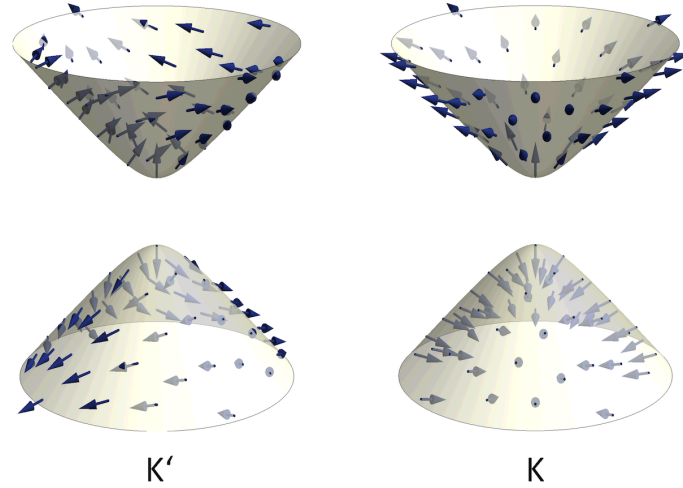


Figure A.3: Band structure and pseudo-spin structure of a honeycomb lattice system with broken inversion symmetry: The spectrum is given by massive Dirac cones at K and K' with a band gap of size Δ . The pseudo-spin, shown by the arrows, obtain a non-zero z-component which is maximum at the Dirac points and goes to zero far away. The valence band carries negative pseudo-spin z-components at both valleys, equal to more B-sublattice content.

The Berry phase can be calculated the same way as it was done for the massless Dirac case. For a honeycomb lattice system with broken inversion symmetry and a loop given by a circle around individual Dirac points, the Berry phase is given by:

$$\begin{aligned} \text{K: } \gamma_\nu &= -\pi(1 - \nu \cos \beta) \\ \text{K': } \gamma_\nu &= +\pi(1 - \nu \cos \beta) \end{aligned} \tag{A.32}$$

When restricting the Berry phase to the range $(-\pi, \pi]$, the Berry phase is always opposite switching from one valley to the other and from one band to the other. The Berry phase is now k-dependent (since $\beta = \beta(k)$). The bigger the radius of the loop around each Dirac point, the larger the absolute value of the Berry phase becomes.

Berry curvature can be calculated according to eq. A.25 and is shown in fig. A.4.

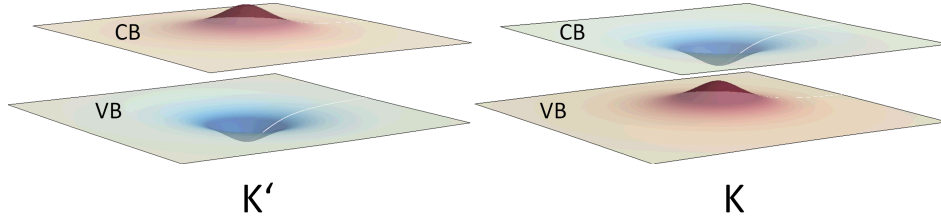


Figure A.4: Berry curvature for the conduction band (CB) and valence band (VB) of a Dirac system with broken inversion symmetry: Within one band, Berry curvature of equal magnitude but opposite sign is created in the vicinity of the Dirac points at the K and K' valley.

In contrast to the gapless Dirac case where Berry curvature is zero everywhere, Berry curvature is created at the vicinity of K and K'. The magnitude of created Berry curvature at the two valleys is the same but the sign is opposite. This way, the Berry phase and the Berry curvature within one band cancel each other at the two valley. Thus, Berry curvature becomes zero when integrating over the full Brillouin zone. Honeycomb lattice systems with broken inversion symmetry, such as hBN and TMDC's, are therefore topologically trivial materials.

A.3.5 Honeycomb Lattice with Broken Time-Reversal Symmetry

One way to break the time-reversal symmetry of graphene is by the presence of a magnetic field. It has been predicted and observed experimentally that graphene in a magnetic field features an anomalous quantum Hall effect [185]. Long before that, even before the first synthesis of graphene [5], in 1988 F. D. M. Haldane realized that a magnetic field is not needed for the occurrence of a quantum Hall effect, breaking the time-reversal symmetry is sufficient [168]. He proposed a complex tight binding model, based on the honeycomb lattice structure, and chiral intra-sublattice hopping due to a special configuration of staggered magnetic fields which sum up to zero within one unit cell of the lattice structure.

While Haldane himself believed that a physical realization of his model was unlikely, it was 2009 when T. Oka and H. Aoki⁵ proposed that graphene under irradiation of circular polarized light exhibits a quantum Hall effect [63]. They employed the ‘‘Floquet mechanism’’ (see sec. D) to realize that a nonlinear effect of the circularly polarized light, which breaks the time-reversal symmetry, can open a gap in the Dirac spectrum, and leads to a photoinduced dc Hall current. A vast number of theoretical studies [63, 175, 177] draw the conclusion that circular polarized light turns graphene into a topologically non-trivial

⁵The second author Hideo Aoki is not to be confused with Steve Aoki, rather an expert in the field of electronic music than electronic bandstructures.

insulator which hosts one-dimensional metallic edge-states, sometimes referred to as “Floquet topological insulator”.

Following the Floquet approach, the lowest order correction term to the Hamiltonian of graphene under irradiation of circularly polarized light is given by a mass term $m\sigma_z$ to the Dirac equation at K and K' [191]. In contrast to the situation of broken inversion symmetry, the mass term has opposite sign at the two valleys:

$$h = v_F(\tau_z\sigma_x k_x + \sigma_y k_y) + \tau_z \frac{\Delta}{2} \sigma_z \quad (\text{A.33})$$

where $\tau_z = +1$ at K and $\tau_z = -1$ at K'. The mass term $\frac{\Delta}{2} = \pm \frac{(eE_0 v_F)^2}{\hbar \Omega^3}$ grows with the field strength E_0 and inverse of the driving frequency Ω , and switches sign when going from σ^+ to σ^- polarization.

The eigenstates of the conduction band ($\nu = +1$) and valence band ($\nu = -1$) are given by

$$\begin{aligned} \text{K:} \quad & |u_{\nu=+1}(\vec{k})\rangle = \begin{pmatrix} \cos \frac{\beta}{2} \\ \sin \frac{\beta}{2} e^{i\phi_k} \end{pmatrix} & |u_{\nu=-1}(\vec{k})\rangle = \begin{pmatrix} \sin \frac{\beta}{2} \\ -\cos \frac{\beta}{2} e^{i\phi_k} \end{pmatrix} \\ \text{K':} \quad & |u_{\nu=+1}(\vec{k})\rangle = \begin{pmatrix} \sin \frac{\beta}{2} \\ -\cos \frac{\beta}{2} e^{-i\phi_k} \end{pmatrix} & |u_{\nu=-1}(\vec{k})\rangle = \begin{pmatrix} \cos \frac{\beta}{2} \\ \sin \frac{\beta}{2} e^{-i\phi_k} \end{pmatrix} \end{aligned} \quad (\text{A.34})$$

with respective eigenenergies of a Dirac particle with non-zero mass $\epsilon_\nu = \nu \sqrt{\left(\frac{\Delta}{2}\right)^2 + v_F^2 k^2}$. The definition of β remains and is given by $\tan \beta = \frac{v_F k}{\Delta/2}$ restricted to the range $0 \leq \beta \leq \pi$. The respective pseudo-spin vectors of the eigenstates are shown in fig. A.5. The pseudo-spin z-component is opposite at the two valleys corresponding to contrary sublattice content.

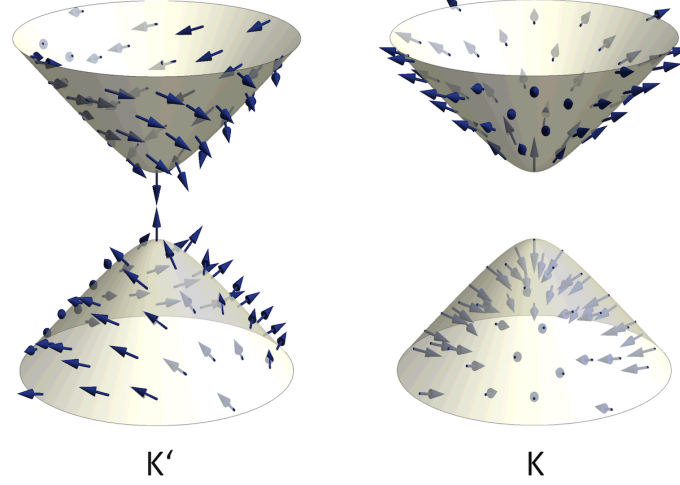


Figure A.5: Bandstructure and pseudo-spin structure of a honeycomb lattice with broken time-reversal symmetry: Massive Dirac cones at K and K' with a band gap of size Δ . The valence band carries pseudo-spin z-components with opposite signs at the K and K' valleys, equal to more B-sublattice content at K and more A-sublattice content at K'.

The Berry phase at the Dirac points is given by

$$\begin{aligned} \text{K: } \gamma_\nu &= -\pi(1 - \nu \cos \beta) \\ \text{K': } \gamma_\nu &= +\pi(1 + \nu \cos \beta) \bmod 2\pi = -\pi(1 - \nu \cos \beta) \end{aligned} \tag{A.35}$$

The Berry phase is equal at both valleys, it only switches sign when going from valence band to the conduction band. As a result, the Berry phase surrounding the full Brillouin zone adds up to a non-trivial value.

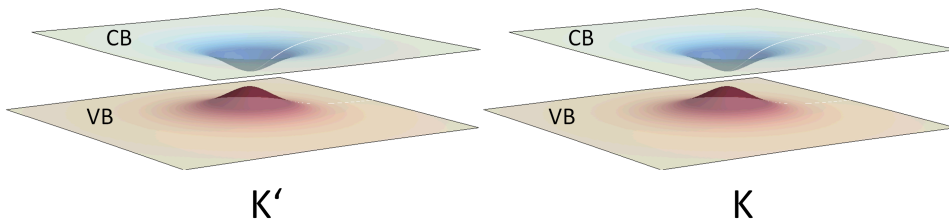


Figure A.6: Berry curvature for the conduction band (CB) and valence band (VB) of a Dirac system with broken time-reversal symmetry: Within one band, Berry curvature of equal magnitude and same sign is created in the vicinity of the Dirac points at the K and K' valley.

The same holds for the Berry curvature (fig. A.6), Berry curvature with the same sign is created at both valleys. The total amount of Berry curvature created within one band

adds up to a non-trivial value, depending on the strength of the driving, equivalently to the gap size. A honeycomb lattice system with broken time-reversal symmetry is therefore a topologically non-trivial material. Since it has a different topology than vacuum, it is predicted to hold one-dimensional metallic edge-states and give rise to an “anomalous” quantum Hall-effect in the absence of a magnetic field.

A.4 Renormalized Electronic Spectrum

Within manybody theory, the spectral function is a fundamental property of solids. In non-interacting systems, the spectral function is a δ -function yielding the electronic band dispersion in energy and momentum space: $\mathcal{A}(\epsilon, \vec{k}) = 2\pi\delta(\epsilon - \epsilon(\vec{k}))$. The respective spectral function of graphene in the absence of interaction has already been discussed in section A.2.2.

In interacting system, quasiparticles obtain a finite lifetime due to scattering with the manybody system. In contrast to a bare quasiparticle, these quasiparticles can be seen as electrons surrounded by a cloud of all other electrons, phonons, etc., constantly interacting with one-another. Within perturbation theory, the spectral function is renormalized due the appearance of a so-called self-energy, $\Sigma(\epsilon, \vec{k})$:

$$\mathcal{A}(\epsilon, \vec{k}) = -2\text{Im}G^R(\epsilon, \vec{k}) = -2\text{Im}\frac{1}{\epsilon - \epsilon_{\vec{k}} - \Sigma^R(\epsilon, \vec{k})} = -2\frac{\text{Im}\Sigma^R}{(\epsilon - \epsilon_{\vec{k}} - \text{Re}\Sigma^R)^2 + (\text{Im}\Sigma^R)^2} \quad (\text{A.36})$$

While the imaginary part of the self-energy, $\text{Im}\Sigma^R$, gives rise to a broadening of the spectral function, the real part of the self-energy, $\text{Re}\Sigma^R$, leads to a change of the band-dispersion. The optical theorem gives a physical meaning to the self-energy: the inverse lifetime of a quasiparticle is in fact equal to the the imaginary part of the (retarded) self-energy: $\tau(\epsilon, \vec{k})^{-1} = \text{Im}\Sigma^R(\epsilon, \vec{k})$.

The scattering mechanisms mentioned above lead to a renormalization of the tight-binding band structure of graphene from fig. 1.1b and fig. 1.2. The signatures in the band dispersion and the spectral broadening due to a finite lifetime of quasiparticles have been vastly observed with high-resolution angle-resolved photoemission spectroscopy [91, 110–116] (see sec. 2.1).

Three renormalization effects have been identified in graphene: Electron-hole creation, Electron-plasmon scattering, and Electron-phonon scattering (see fig. A.7).

- **Electron-hole-pair creation:** The process combines all possible electron-electron scattering events, shown in fig. 1.4, of creating an electron-hole-pair (electron above

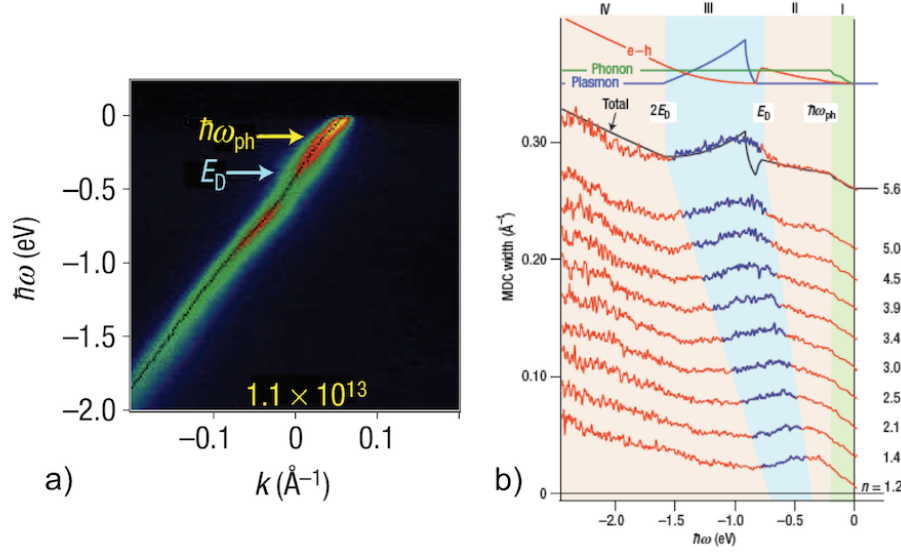


Figure A.7: Graphene linewidth analysis from [91]: (a) Measured photoemission spectrum and (b) fitted linewidths (proportional to $\text{Im}\Sigma$). Simulated total scattering rate (black line) and the partial contributions due to a photohole-decay into phonons (green), electron-hole pairs (red) and plasmons (blue) are compared with linewidths of graphene samples with different doping levels, achieved by potassium adsorption.

E_F). The main effect is broadening of bands, equal to decrease of quasi-particle lifetime, for high-binding energies where the phase space for electron-hole-pair creation grows. In contrast to Fermi-liquid theory where the scattering rates increases as $\sim (E - E_F)^2$, the linear band structure and the presence of the Dirac point with vanishing density-of-states, drastically modifies the energy dependence.

- **Electron-plasmon scattering:** Since plasmons are only stable up to $\sim |\mu|$ and its dispersion is always above the light-cone ($\omega_{\text{plasmon}} > v_F q$), energy and momentum conservation forces electron-plasmon scattering events to take place solely in the vicinity of the Dirac point in the range from $E_D - |\mu|$ to E_D . The effect of the Electron-plasmon interaction is an increase in band velocity in the vicinity of the Dirac point, which is referred to as *elongation of the Dirac point*.
- **Electron-phonon scattering:** The only phonon-mode with detectable influence on the bandstructure is given by the strongly coupled E_{2g} optical phonon mode at 200meV. The effect is a textbook example of electron-phonon coupling induced band renormalization, leading to a kink in the dispersion at $E_F - E_{\text{phonon}}$ and a sudden decrease of quasiparticle lifetime at the same energy. The electron-phonon coupling constant is doping-dependent in graphene due to the linear bandstructure and the following restrictions to the scattering phase space. The coupling constant is found to be $\lambda \approx 0.3$ in n-doped epitaxial graphene grown on SiC ($\mu = 0.4\text{eV}$) [91] and

$\lambda \approx 0.05$ in p-doped hydrogen-intercalated graphene ($\mu = -0.2eV$) [110,113].

Plasmaron Sidebands

In epitaxial graphene samples with low substrate dielectric screening (observed strongest in H- and F-intercalated monolayer graphene) which are heavily n-doped by potassium adsorption up to $\mu = 1eV$, plasmon satellites have been observed [111]. Under these circumstances, the electron-plasmon coupling is strong enough for the formation of new quasiparticles called plasmarons, which are plasmon-dressed electron or hole states. In photoemission spectra, plasmaron states in the form of plasmon-dressed photoholes appear as a sideband below the bare bandstructure, best observed in the vicinity of the Dirac point⁶. Comparing the data to G_0W -RPA-calculations, allowed to make estimates of dielectric screening constants ϵ_S of various substrates [111,192].

Electron-Phonon Coupling Constant of σ -Bands

An electron-phonon kink also appears in the σ -bands of graphene (fig. A.8a) at the phonon energy of 200meV below the band maximum at $E \approx E_F - 4.3eV$ close to the Γ -point (see fig. A.8b), observed on a variety of substrates such as SiC, Ir and Rb [114,116]. The abrupt disappearance of density of states at the band maximum plays the equivalent role which the Fermi-level does for the occurrence of the phonon kink in the π -bands. The Electron-phonon coupling constant in the σ -bands is found to be of considerable strength with $\lambda \approx 0.9$, independent of the substrate [114,116].

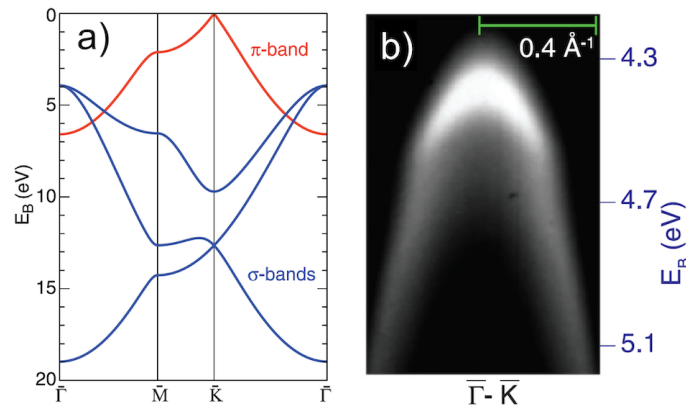


Figure A.8: Electron-phonon kink of σ bands in graphene: a) Simulated σ - and π -band structure of graphene, b) Experimental ARPES spectrum of σ -bands at Γ -point in the second Brillouin-zone from [116]

⁶The plasmaron sidebands are discussed controversially: In an extended GW-study including vertex corrections the plasmon satellites are accurately described without the formation of plasmarons [192].

A.5 Interband Excitation in Graphene

The experiment described in chapter 4 makes use of anisotropic interband excitations in graphene to study the thermalization dynamics in two-dimensional momentum space. The anisotropic excitation is polarization dependent, it has been widely predicted [78,129] and observed [126,127,130,131]. The optical interband transition in graphene can be understood within a simple Fermi's golden rule approximation.

The considerations shown here are very similar to the ones for the three-step model of photoemission for graphene, described in section B.2.2. The absorption rate is given by the transition rate from an initial single-particle state in the lower Dirac cone ($\nu_i = -1$) to the final single-particle state in the upper Dirac cone ($\nu_f = +1$):

$$w_{VB \rightarrow CB} = \frac{2\pi}{\hbar} \underbrace{\left| \langle \Psi_{\nu_f=+1}(\vec{k}_f) | H_{int} | \Psi_{\nu_i=-1}(\vec{k}_i) \rangle \right|^2}_{|M(\vec{k}, \vec{A})|^2} \delta(E_f - E_i - \hbar\omega) \quad (\text{A.37})$$

with the single-particle states $|\Psi_\nu(\vec{k})\rangle$ as given in eq. A.9 and the energy states: $E_i = -\hbar v_F k_i$ and $E_f = +\hbar v_F k_f$. Since the momentum of the photon can be neglected, the optical transition is vertical in energy-momentum space: $\vec{k}_i = \vec{k}_f = \vec{k}$ and $k = \frac{1}{2} \frac{\omega}{v_F}$.

The interaction Hamiltonian is discussed in section B.2.2 and reads:

$$H_{int} = -e v_F \vec{\sigma} \cdot \vec{A} \quad (\text{A.38})$$

Setting out the matrix multiplication, the transition matrix element is then given by

$$\begin{aligned} M(\vec{k}, \vec{A}) &= -e v_F \left(\frac{1}{\sqrt{2}} \right)^2 \begin{pmatrix} 1 & e^{-i\phi_k} \end{pmatrix} \left[A_x \cdot \begin{pmatrix} 0 & 1 \\ 1 & 0 \end{pmatrix} + A_y \cdot \begin{pmatrix} 0 & -i \\ i & 0 \end{pmatrix} \right] \begin{pmatrix} 1 \\ -e^{i\phi_k} \end{pmatrix} \\ &= -e v_F i (-A_x \sin \phi_k + A_y \cos \phi_k) \end{aligned} \quad (\text{A.39})$$

The absolute square of the matrix element reads:

$$\left| M(\vec{k}, \vec{A}) \right|^2 = e^2 v_F^2 A^2 \sin^2(\phi_A - \phi_k) \quad (\text{A.40})$$

Hence, there is no excitation in the direction of the electric field and maximum excitation perpendicular to it (see fig. A.9).

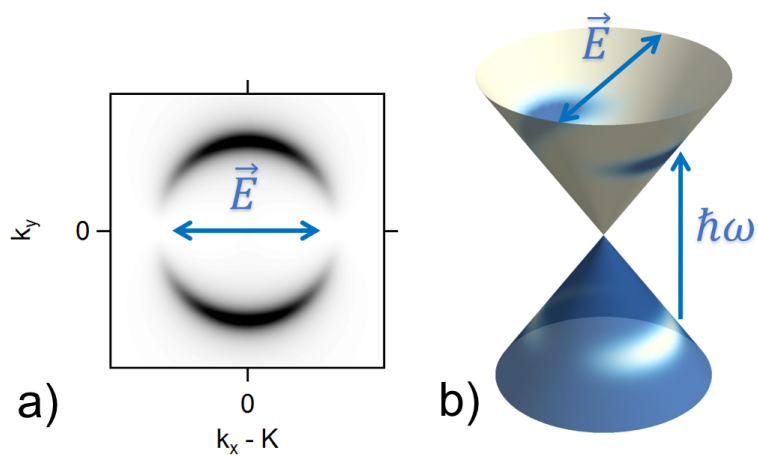


Figure A.9: Interband excitation in graphene: a) Optical interband matrix element squared as given by eq. A.40 in case of x-polarized light and b) resulting electronic distribution instantly after absorption of a respective linearly polarized pump pulse with photon energy $\hbar\omega$.

APPENDIX B

Theoretical Background of Photoemission Spectroscopy

B.1 Introduction

Photoemission spectroscopy (PES) refers to all techniques that are based on the application of the photoelectric effect. The effect was originally observed by Hertz [193] and later explained by Einstein [194] recognizing the quantized nature of light: When light is incident on a solid, an electron can absorb light-quanta called photons with energy $h\nu$ to escape from the material with a maximum kinetic energy $E_{kin} = h\nu - \phi$. ϕ is called the work function of the solid, which serves as the natural barrier at the surface which prevents the electrons from escaping, and its typical value in metals is 4-5eV. The energy relation is the consequence of energy conservation of the described photoemission process (see fig. B.1).

The first electron dispersion curve was measured in about 1980 with PES [195]. Since then the technique was developed way beyond its initial framework, fastly advancing into the method of choice for measuring band structures of solids. With synchrotron radiation and highly developed energy detectors, high energy resolution ($\sim 2\text{meV}$) and 0.2° angular resolution have been achieved [196]

However, modern techniques (sketched in fig. 2.1) retain the core approach as the first photoemission spectroscopy experiments. Hertz produced ultraviolet (UV) radiation by discharge of arcs driven by induction coils. Only UV radiation, or light of even shorter wavelengths, carries photons with energies high enough for the electrons to overcome the work function and escape the material. Light sources have changed since then, small

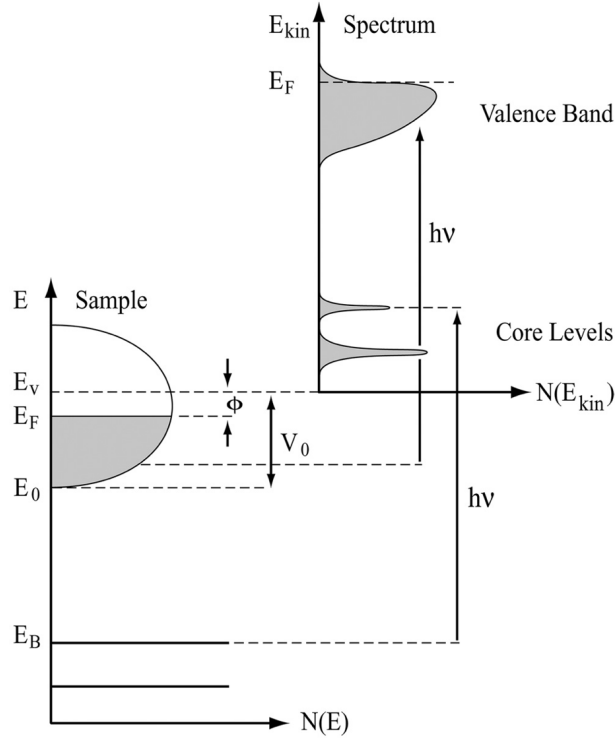


Figure B.1: Photoemission-Spectroscopy Energetics in a non-interacting solid from [195, 196]: Relation between the energy levels in the solid and the photo-electron energy distribution produced by photons of energy $\hbar\omega$. The kinetic energy of the photoelectrons with its zero at the vacuum level E_{vac} relate as $E_{kin} = \hbar\omega - E_B - \phi$ to the electron's binding energy E_B , and to the work function ϕ of the solid.

research labs use either gas-discharge lamps or X-ray tubes. Large synchrotron facilities have been built with the only purpose of producing highly monochromatic light in the right spectral range for users to take high quality photoemission spectra. Also the electron detectors have changed over the years. Not only the kinetic energy of the photoelectrons is detected, but also their emission angle (momentum) and their spin.

An alternative light source was provided by the development of ultrashort-lasers and the technique of high-harmonic generation (see sec. 2.2.2). Embedding this technique within a pump probe experiment allows adding time as a new dimension to PES. This combination of experimental techniques is widely used throughout this work. Electronic distributions are followed as function of energy, momentum and delay time (see sec. 2.2 on trARPES).

B.2 Theoretical Models

Understanding experimental results from photoemission is impossible without some insight into theory of photoemission spectroscopy (PES). This section describes some aspects of PES theory while focusing on graphene.

One common starting point for photoemission theories is Fermi's golden rule in the most general form between the N -electron states Ψ_i (initial) and Ψ_f (final). The transition rate reads:

$$w_{i,f} = \frac{2\pi}{\hbar} |\langle \Psi_f | H_{int} | \Psi_i \rangle|^2 \delta(E_f - E_i - \hbar\omega) \quad (\text{B.1})$$

In the general form and using gauge $\phi = 0$, the interaction term is given by:

$$H_{int} = \frac{e}{2mc} (\vec{A} \cdot \vec{p} + \vec{p} \cdot \vec{A}) + \frac{e^2}{2mc^2} \vec{A}^2 \approx \frac{e}{mc} \vec{A}_0 \cdot \vec{p} \quad (\text{B.2})$$

Where \vec{A} is the vector potential and $\vec{p} = i\hbar\vec{\nabla}$ the momentum operator. In most cases the terms \vec{A}^2 (two-photon absorption) and $\vec{\nabla}\vec{A} = 0$ are neglected, the latter due to the translational invariance of the solid. For typical photon-energies ($\hbar\omega = 10 - 30\text{eV}$) one has wavelengths of $\approx 10^3\text{\AA}$ and one often uses the dipole approximation $\vec{A} = \vec{A}_0 e^{i(\vec{k}\vec{x} - \omega t)} \approx \vec{A}_0 e^{-i\omega t}$. Altogether, these considerations lead to the approximation in the interaction term above.

The initial state $|\Psi_i\rangle$ is the N -electron state of the solid prior to photoemission. This state could be at thermal equilibrium or as it is the case in a trARPES experiment, an excited electronic state itself. Assuming that the initial state is a single Slater determinant (Hartree-Fock formalism), the state can be written as the product of a one-electron Bloch state $\phi_i(k_i)$ (the initial state of the electron which is going to be the photoelectron) and an $(N - 1)$ -particle term [196]:

$$|\Psi_i\rangle = |\Psi_i^N\rangle = |\phi_i(k_i)\rangle |\Psi_i^{N-1}\rangle \quad (\text{B.3})$$

The final state $|\Psi_f\rangle$ is what defines the theory and to some extent the quality of the model: Generally speaking, the final state is a state where one electron has been removed from the solid, which arrives at the detector with a certain kinetic energy E_{kin} and momentum $\hbar\vec{k}$, in combination with all possible states leaving $(N-1)$ electrons left behind in the material. This final state can be substantially different to the initial state, especially in a system with many degrees of freedom due to N being a big number. Thus, PES theory is a complex many body problem [195].

Most photoemission theories are based on the so-called sudden approximation: in that

case, it is assumed that the creation of the photohole happens instantaneously, meaning that there is no interaction of the escaping photoelectron with the remaining electronic system which is left behind. This theory is designed for the high energy photoelectron limit and gives accurate results for $E_{kin} \gtrsim 10eV$ [197]. In this case, the final state can be factorized into photoelectron and $(N - 1)$ terms:

$$|\Psi_f\rangle = \sum_s |\Psi_s^{N-1}; \vec{k}\rangle = |\phi_f(\vec{k})\rangle \sum_s |\Psi_s^{N-1}\rangle \quad (\text{B.4})$$

where $|\phi_f(\vec{k})\rangle$ is the wavefunction of the photoelectron with momentum \vec{k} and kinetic energy $E_{kin} = \frac{(\hbar k)^2}{2m}$. $|\Psi_s(N - 1)\rangle$ are all s final states of the $(N - 1)$ interacting electron system left behind with respective energies E_s^{N-1} , which can differ from one another. In accurate models, the final state wavefunction of the photoelectron is approximated by time-inverted LEED states. These states describe free electron states within the solid and become plane waves in the limit of the vacuum far away from the solid. Within the sudden approximation the photocurrent then reads:

$$\begin{aligned} w_{i,f} &= \sum_s \frac{2\pi}{\hbar} \left| \langle \phi_f(\vec{k}) | \langle \Psi_s^{N-1} | H_{int} | \Psi_i^N \rangle \right|^2 \delta(E_{kin} + E_s^{N-1} - E_0^N - \hbar\omega) \\ &= \frac{2\pi}{\hbar} \underbrace{\left| \langle \phi_f(\vec{k}) | H_{int} | \phi_i(k_i) \rangle \right|^2}_{|M_{f,i}^k|^2} \sum_s \left| \langle \Psi_s^{N-1} | \Psi_i^{N-1} \rangle \right|^2 \delta(E_{kin} + E_s^{N-1} - E_0^N - \hbar\omega) \end{aligned} \quad (\text{B.5})$$

The first term, $|M_{f,i}^k|^2$, is the square of the one-electron transition matrix element of photoemission. The second term describes all the relaxation processes of the left-behind $(N - 1)$ electronic system, and has a simple interpretation, which can be easily understood within the independent particle approximation: in combination with the δ -function, the term is equal to the lesser Green's function, $G^<(\epsilon, \vec{k})$, in the Lehmann-representation, one of the most fundamental properties of an N -electron system (compare e.g. to [183]).

$$\begin{aligned} &\sum_s \left| \langle \Psi_s^{N-1} | \Psi_i^{N-1} \rangle \right|^2 \delta(E_{kin} + E_s^{N-1} - E_0^N - \hbar\omega) \\ &= \sum_s \langle \Psi_i^N | c_{i,\vec{k}_i}^\dagger | \Psi_s^{N-1} \rangle \langle \Psi_s^{N-1} | c_{i,\vec{k}_i} | \Psi_i^N \rangle \delta(\epsilon_i - \phi - E_s^{N-1} + E_0^N) \\ &= \frac{1}{i\hbar} G^<(\epsilon_i, \vec{k}_i) = f(\epsilon_i) \mathcal{A}(\epsilon_i, \vec{k}_i) \end{aligned} \quad (\text{B.6})$$

Where $f(\epsilon_i)$ is the electronic distribution function evaluated at the photoelectron's initial state energy ϵ_i , i.e. the Fermi-function if the system is in the equilibrium state, and $\mathcal{A}(\epsilon_i, \vec{k}_i)$ is the spectral function of the system. Simply speaking, the spectral function describes all the relaxation processes of the left-behind $(N - 1)$ electronic system. It is noted, that after redefining the δ -function, the kinetic energy of the photoelectron is set to $E_{kin} = \hbar\omega + \epsilon_i - \phi$.

In case of photoemission, the spectral function represents the left-behind photohole, while the finite lifetime of the photohole leads to smearing of the spectral function. Nowadays, ARPES experiments reach high enough energy and momentum resolutions such that renormalization effects of the spectral function can be detected, allowing the observation of a variety of dynamical manybody effects.

B.2.1 Three-Step Model

While the means of photoemission spectroscopy is based on measuring the spectral function of an electronic system, the photocurrent is also influenced by the one-electron transition matrix element, $M_{f,i}^k$. In some cases, and to some degree this is true for graphene, parts of the band structure are simply turned “invisible”. However, the single-particle transition matrix element is a highly non-trivial object, theoretical calculations can be very complex and it can have severe influence on PES spectra. The most accurate calculations are performed within the so-called 1-step model where the final state is often taken as time-inverted LEED states. $M_{f,i}^k = \langle \phi_f^{trLEED}(\vec{k}) | H_{int} | \phi_i^{Bloch}(k_i) \rangle$.

The theory is typically further simplified within the so-called 3-step model (see fig. B.2). It was developed by Berglund and Spicer [198] and is the most commonly used model for the interpretation of photoemission spectra in solids: here, the photoemission process is split into three separate processes, giving rise to three terms of the one-electron photoemission matrix element (eq. B.7). At the heart of the approximation, these three steps are treated individually, thus, not taking in account any quantum interference effects that happen in the course of all three events, as the 1-step model does. It is a purely phenomenological theory but very successful, and in many cases leads to quite accurate results.

$$|M_{f,i}^k|^2 = |M^{(1)}|^2 |M^{(2)}|^2 |M^{(3)}|^2 \quad (\text{B.7})$$

Step 1: photoexcitation of an electron within the solid: this implies that the matrix element $M_{f,i}^k = \langle \phi_f^{trLEED}(\vec{k}) | H_{int} | \phi_i^{Bloch}(k_i) \rangle \approx \underbrace{\langle \phi_f^{Bloch}(\vec{k} = \vec{k}_i + \vec{G}) | H_{int} | \phi_i^{Bloch}(k_i) \rangle}_{M_{f,i}^{(1)}} M^{(2)} M^{(3)}$

is evaluated between two Bloch states (initial and excited Bloch state) in the solid, instead of the more realistic time-reversed LEED state for the final state. $M^{(2)}$ and $M^{(3)}$ are the phenomenological matrix elements from step 2 and 3. The matrix-element, $M_{f,i}^{(1)}$, implies momentum conservation up to an inverse lattice vector G .

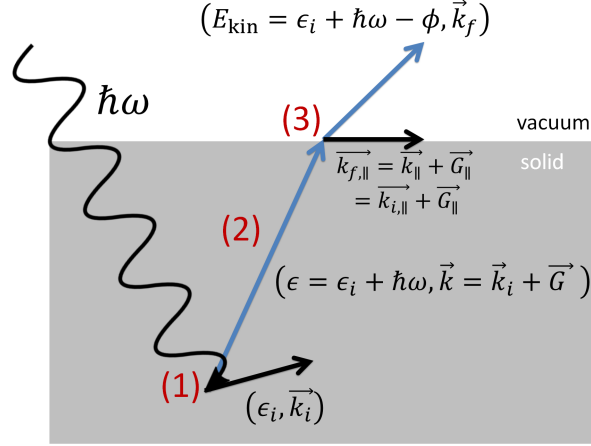


Figure B.2: Three-step model of the photoelectric effect: (1) Photoexcitation of an electron, (2) its passage to the surface, and (3) the transition to the vacuum.

Step 2: propagation of the photoexcited electron to the surface: the inelastic mean free path of electrons in solids, with energies higher than the vacuum level, follows a universal curve over a big range from 0-10keV [199] for all materials. The inelastic mean free path in the range from 10-120eV is particularly short (much shorter than the penetration depth of UV and X-Ray light), making photoemission a surface sensitive technique when using photon energies in that range. The effects of inelastic scattering can be taken in account by assuming a complex wavevector perpendicular to the surface $k_{\perp} = k'_{\perp} + ik''_{\perp}$, which gives rise to momentum smearing. Alternatively one can simulate the effect by using a complex (optical) potential for the crystal potential. In 2D materials, like graphene, these effects will be rather small and will be neglected here, thus, $M_{f,i}^{(2)} \approx 1$.

Step 3: escape of the electron from the solid to the vacuum: the matrix element, $M_{f,i}^{(3)}$, maps the excited Bloch state onto final plane wave states, which describe the free electron state in vacuum. Due to the translation invariance perpendicular to the surface normal, this process demands conservation of the in-plane k-vector up to an inverse lattice vectors: $|M^{(3)}|^2 = \delta(\vec{k}_{\parallel,vac} - \vec{k}_{\parallel} + \vec{G}_{\parallel})$. This conservation law at the solid-vacuum interface justifies ARPES for ensuring the equality of the parallel momentum component between the photoelectron's final and initial state. The validity of this approximation requires a perfectly flat crystallographic surface. A rough surface will lead to diffuse scattering, thus, to blurring of the momentum information.

The photocurrent within the 3-step model reads:

$$I_{k_f, E_{kin}} \propto \left| \langle \phi_f^{Bloch}(E_{kin}, \vec{k} = \vec{k}_i + \vec{G}) | H_{int} | \phi_i^{Bloch}(k_i) \rangle \right|^2 f(\epsilon_i) \mathcal{A}(\epsilon_i, \vec{k}_i) \delta(k_{f,\parallel} - k_{i,\parallel} + G_{\parallel}) \quad (\text{B.8})$$

where the photoelectron's kinetic energy is given by $E_{kin} = \frac{(\hbar k_f)^2}{2m} = \hbar\omega + \epsilon_i - \phi$.

B.2.2 Photoemission from Graphene within the Three-Step Model

A simple model for interpreting photoemission spectra of graphene in the vicinity of the Dirac point shall be given here. The starting point is given by the three step model, as shown in eq. B.8.

When applying the model to graphene, there is one complicating factor, which needs to be addressed first: the two-dimensionality of graphene's wavefunctions, which in the vicinity of the Dirac point become a spinors in pseudo-spin space (see sec. A.2), formally lead to a 2x2 matrix structure of the spectral function, $A(\epsilon_i, \vec{k}_i)$. The physical reason for the effect is, that quasiparticles' wavefunctions consist of two Blochwaves, each living on separate sublattices, which leads to interference when a quasi-particle is photoemitted.

For the given reasons, the interaction term h_{int} from eq. B.2 needs to be adapted. As pointed out in [92], the calculation of h_{int} requires special care considering that a tight-binding Hamiltonian describes a nonlocal system. Techniques to calculate the correct form of h_{int} for this case are described in [200, 201]. In respect to the whole Brillouin zone the interaction is then given by $H_{int} = -\frac{e}{c} \vec{A} \cdot \vec{p} = -\frac{e}{c} [\hat{r}, H_0]$, where $\hat{r} = i\hbar\nabla_k$. In the vicinity of the Dirac points, where the electrons are described by the Dirac equation, the coupling term can alternatively be found by the minimal coupling replacement $\vec{k} \rightarrow \vec{k} - e\vec{A}$:

$$h_{int} = -ev_F \vec{\sigma} \cdot \vec{A} \quad (\text{B.9})$$

where $\vec{\sigma} = (\sigma_x, \sigma_y)$ are the Pauli-matrices. Within the 3-step model the single-particle transition matrix-element in eq. B.8 is evaluated between the photoelectron's initial state $|\phi_i\rangle$ and the Bloch wave of the excited electron. The latter can be found by the projection of the final plane-wave state onto the p_z orbitals of graphene's atomic sites [92], expressed as two Bloch sums over the two sublattices A and B¹:

$$|\phi_f^{Bloch}(\vec{k}_f)\rangle = \frac{1}{\sqrt{2}} \begin{pmatrix} 1 \\ 1 \end{pmatrix}_{\vec{k}} \quad (\text{B.10})$$

¹See eq. A.1 in section A.1 on how the Bloch waves are constructed. The notation used in eq. B.10 implicates the parameters $C^A(\vec{k}) = C^B(\vec{k}) = 1$.

Since graphene has two bands, the photocurrent has two contributions, expressed by a sum over the band indice $\nu_i = \pm 1$. With the given considerations and according to eq. B.8 the photocurrent reads:

$$\begin{aligned}
 I_{k_f, E_{kin}} &\propto \sum_{\nu_i = \pm 1} \left| \langle \phi_f^{Bloch}(\vec{k}_f) | h_{int} | \phi_{\nu_i}(k_i) \rangle \right|^2 \sum_s |\langle \Psi_s^{N-1} | \Psi_{\nu_i}^{N-1} \rangle|^2 \delta(E_{kin} + E_s^{N-1} - E_0^N - \hbar\omega) \\
 &= \sum_{\nu_i = \pm 1} \langle \phi_f^{Bloch}(\vec{k}_f) | h_{int} | \underbrace{\phi_{\nu_i}(k_i)}_{=P_{\nu_i}(\hat{k}_i) = \frac{1+\nu_i\vec{\sigma}\cdot\hat{k}}{2}} | h_{int} | \phi_f^{Bloch}(\vec{k}_f) \rangle \\
 &\quad \cdot \underbrace{\sum_s \langle \Psi^N | c_{\nu_i, \vec{k}_i}^\dagger | \Psi_s^{N-1} \rangle \langle \Psi_s^{N-1} | c_{\nu_i, \vec{k}_i} | \Psi^N \rangle \delta(\epsilon_i - \phi + E_s^{N-1} - E_0^N)}_{= \frac{1}{i} G_{\nu_i \nu_i}^<(\epsilon_i, \vec{k}_i)}
 \end{aligned} \tag{B.11}$$

Where $G_{\nu_i \nu_i}^<(\epsilon_i, \vec{k}_i)$ are the diagonal elements of the lesser Green's function in the diagonalized *chiral* basis (see section A.2.3 in the appendix). By rewriting

$$\begin{aligned}
 h_{int} | \phi_f^{Bloch}(\vec{k}_f) \rangle &= -ev_F \vec{\sigma} \cdot \vec{A} \frac{1}{\sqrt{2}} \begin{pmatrix} 1 \\ 1 \end{pmatrix} = -ev_F \left(A_x \frac{1}{\sqrt{2}} \begin{pmatrix} 1 \\ 1 \end{pmatrix} + A_y \frac{1}{\sqrt{2}} \begin{pmatrix} -i \\ i \end{pmatrix} \right) \\
 &= -ev_F \underbrace{\left| \vec{A} \right| \frac{1}{\sqrt{2}} \begin{pmatrix} e^{-i\phi_A} \\ e^{i\phi_A} \end{pmatrix}}_{\equiv \vec{\epsilon}(\phi_A)},
 \end{aligned} \tag{B.12}$$

with $\vec{\epsilon}(\phi_A) = \frac{1}{\sqrt{2}}(e^{-i\phi_A}, e^{i\phi_A})^T$, the photocurrent reads²:

$$\begin{aligned}
 I_{k_f, E_{kin}} &\propto \sum_{\nu_i = \pm 1} \underbrace{\vec{\epsilon}^*(\phi_A) P_{\nu_i}(\hat{k}_i) \vec{\epsilon}(\phi_A)}_{= \frac{1}{2}(1+\nu_i \cos(\phi_{k_i} - 2\phi_A))} \frac{1}{i} G_{\nu_i \nu_i}^<(\epsilon_i, \vec{k}_i) \\
 &= \vec{\epsilon}^*(\phi_A) \frac{1}{i} G^<(\epsilon_i, \vec{k}_i) \vec{\epsilon}(\phi_A) = \vec{\epsilon}^*(\phi_A) f(\epsilon_i) \mathcal{A}(\epsilon_i, \vec{k}_i) \vec{\epsilon}(\phi_A)
 \end{aligned} \tag{B.13}$$

where $G^<(\epsilon_i, \vec{k}_i)$ and $\mathcal{A}(\epsilon_i, \vec{k}_i)$ are the lesser Green's function and spectral function in the *natural* non-diagonal sublattice basis. The polarization dependent vector $\vec{\epsilon}(\phi_A)$ contracts the (2x2) spectral function and gives rise to the *dark-corridor* as discussed in sec. 2.1.1.

²As seen in appendix A.2.3, all bare Green's functions become diagonal in a chiral basis. For the last equality in eq. B.13 it has been assumed that the fully dressed Green's function stays diagonal in this basis.

B.2.3 One-Step Model and Photoemission Theories Beyond the Sudden Approximation

Photoemission models that go beyond the three step model are taking in account propagation effects and quantum interferences which happen throughout the whole photoemission process. Since they do not divide the photoemission process into artificial individual steps, they are called one-step models. Some theories even go beyond the sudden approximation, taking in account the interaction of the photoexcited electron with the other (N-1) electrons left behind. The final state, in its most general form, was given by Lars Hedin in [197]:

$$\psi_{k,s} = \left(1 + \frac{1}{E - H - i\eta} V \right) c_k^\dagger |s\rangle \quad (\text{B.14})$$

where c_k^\dagger is the creation operator of a photoexcited electronic state with free electron energy. The additional term to the 1 describes the processes where the photoelectron scatters or interacts on its way out of the solid. In order to make 1-step calculations feasible, some approximations have to be made. One of the best-founded approximations is the use of time-inverted LEED states as the photoelectron's final state.

In graphene, the 3-step model gives quite accurate results for photon energies up to 40eV. For all photon energies used in this work, the simplistic model from section B.2.2 was sufficient for interpreting ARPES spectra. In a high-resolution ARPES study with synchrotron radiation it was seen, that for high photon energies above 40eV, deviations from the three-step model occur, which can be explained with time-reversed LEED as final states within one-step models [93].

APPENDIX C

Additional Results from Microscopic Simulations

In order to interpret experimental data from chapter 4, microscopic simulations were performed by the group of E. Malic at Chalmers University of Technology (Gothenburg, Sweden). Additional results from these simulations, not shown in chapter 4, are presented here and discussed in detail. All simulations display the magnitude of the anisotropy ΔN as defined in eq. 4.1 as a function of pump-probe time delay.

Impact of Pump Fluence

First, the pump-fluence dependence of the anisotropy is investigated. Considering an undoped graphene sample on a SiC substrate with a dielectric constant of $\varepsilon_s = 7.8$, the temporal evolution of the anisotropy for two different pump fluences ($50 \mu\text{J}/\text{cm}^2$ and $1.5 \text{mJ}/\text{cm}^2$, respectively) is directly compared in fig. C.1. The large pump fluence is comparable to the one used in the trARPES measurements in chapter 4. To reveal the elementary processes responsible for the decay of the anisotropy, the full dynamics (continuous lines) as well as calculations taking into account only carrier-phonon (c-ph, dashed lines) or carrier-carrier scattering (c-c, dotted lines) are compared. The most obvious impact of the fluence is a significantly increased anisotropy ΔN in the strong excitation regime, simply reflecting the higher number of photo-excited carriers.

It is noted that previous optical pump-probe measurements used a different definition for the anisotropy based on the pump-induced changes of the transmission ΔT . In this case, the ratio between ΔT for parallel and cross-polarized pump and probe beams was found to decrease with increasing fluence [129].

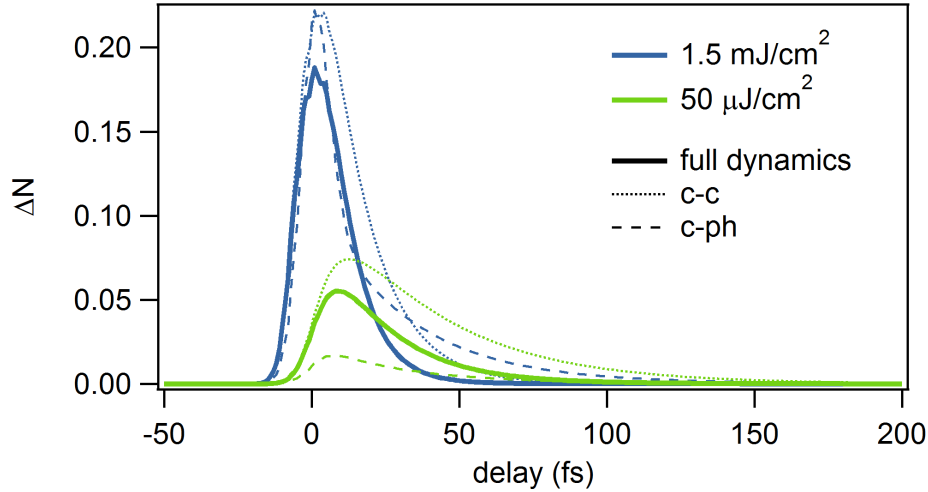


Figure C.1: Fluence dependence. Temporal evolution of the carrier anisotropy ΔN in an undoped graphene sample on SiC ($\epsilon_s = 7.8$) for a relatively small ($50 \mu\text{J}/\text{cm}^2$, green) and a relatively large pump fluence ($1.5 \text{ mJ}/\text{cm}^2$, blue). To reveal the role of single many-particle processes, the full dynamics (continuous lines) is compared with the dynamics taking into account only carrier-phonon scattering (dashed lines) and carrier-carrier scattering (dotted lines).

By comparing the dashed and dotted green lines in fig. C.2, it is concluded that the decay of the anisotropy in the small fluence regime is dominated by c-ph scattering in good agreement with literature [78, 126]. This is because optically excited carriers can efficiently scatter across the Dirac cone via different phonon modes. In contrast, Coulomb interaction prefers collinear scattering events [126, 131].

The situation is different in the high fluence regime, where c-c becomes more efficient due to the large number of photo-excited electrons. In this case, non-collinear c-c scattering and c-ph scattering become of similar importance for the decay of the anisotropy (see the dotted and dashed blue lines in fig. C.1). However, c-ph scattering still remains the dominant channel for the reduction of the anisotropy in the first tens of femtoseconds. Non-collinear c-c scattering becomes important at later times, where the dotted and dashed blue lines in fig. C.1 cross. This crossover happens once the photo-excited electrons, after having emitted a couple of phonons, are too close to the Fermi level to allow for further phonon emission.

Impact of doping

Now the influence of doping for a given fluence ($1.5 \text{ mJ}/\text{cm}^2$) and substrate screening ($\epsilon_s = 7.8$) is studied. N-doping of 400 meV, equivalent to n-doped TDMLG samples, is assumed. A bigger amplitude of the anisotropy is found in the n-doped graphene sample

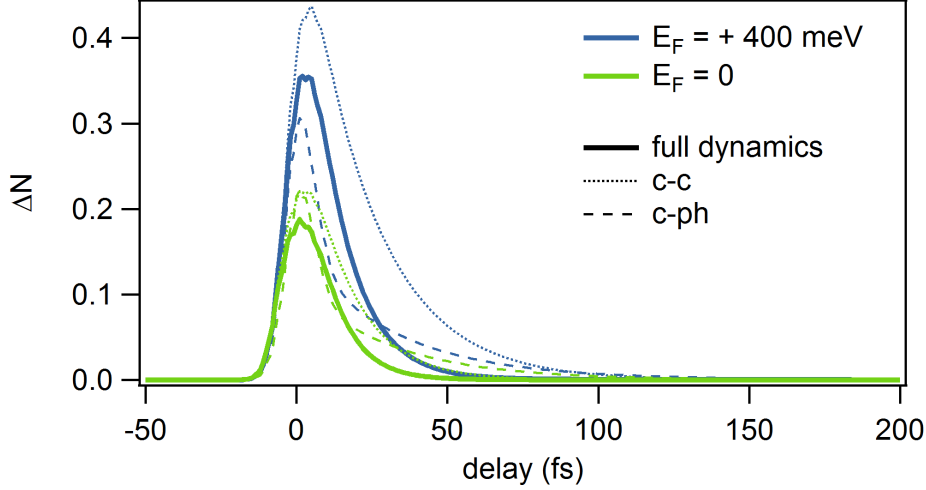


Figure C.2: Dopening dependence. Temporal evolution of the anisotropy ΔN in the strong excitation regime (1.5 mJ/cm^2) for n- ($E_F=400 \text{ meV}$, blue) and undoped graphene (green) on SiC ($\epsilon_s = 7.8$). The impact of Coulomb- (dotted line) and phonon-induced (dashed line) scattering channels is illustrated separately. The complete dynamics is shown as continuous lines.

compared to the undoped graphene sample (blue and green in fig. C.2, respectively) for the full dynamics as well as for carrier-carrier and carrier-phonon scattering only. This is attributed to a combination of a reduced scattering phase space for c-c and c-ph scattering as well as a bigger screening of the Coulomb interaction due to the increased number of free carriers in the n-doped graphene sample.

Impact of Substrate Screening

In fig. C.3 the influence of the substrate on the amplitude and decay of the anisotropy of the photo-excited carrier distribution is investigated. The presence of a substrate can efficiently screen the Coulomb interaction by a factor of $1/\epsilon_{\text{eff}}$, where $\epsilon_{\text{eff}} = (1 + \epsilon_s)/2$ is related to the dielectric constant of the substrate ϵ_s [111]. Here, the anisotropy in the presence of the substrate screening constants of QFMLG ($\epsilon_s = 7.8$) and TDMLG $\epsilon_s = 43$ are compared. In both cases, n-doped graphene samples with $E_F=400 \text{ meV}$ in the strong excitation regime (1.5 mJ/cm^2) are considered.

A considerably slower decay of the anisotropy for the large dielectric constant is found. This can be clearly ascribed to the drastically slower Coulomb-induced c-c scattering (see dotted lines in fig. C.3). In this situation, c-ph scattering becomes the dominant channel for redistributing the optically excited carriers and reducing the initial carrier anisotropy. It is noted that, in the framework of the present model, the c-ph coupling is unscreened.

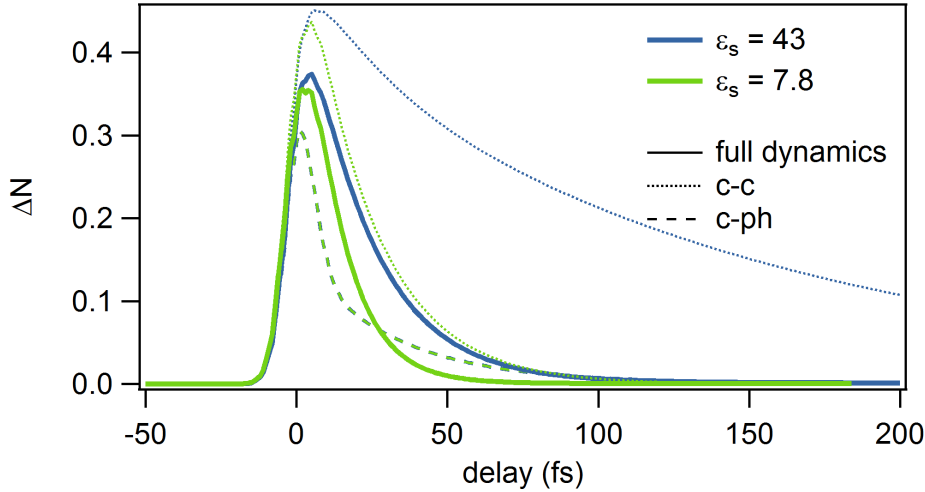


Figure C.3: Substrate dependence. Temporal evolution of the carrier anisotropy ΔN in the strong excitation regime (1.5 mJ/cm^2) for an n-doped ($E_F=400 \text{ meV}$) graphene sample on H-SiC (dielectric constant of $\varepsilon_s = 7.8$) and on $6\sqrt{3}$ C-SiC (dielectric constant of $\varepsilon_s = 43$). The continuous, dashed, and dotted lines represent the full dynamics, the dynamics with c-ph scattering only, and the dynamics with c-c scattering only, respectively. It is noted that the two dashed lines overlap.

Modelling of the Measured Anisotropy

Simulations investigating the anisotropy under the exact experimental conditions are already shown in fig. 4.6 in chapter 4. In agreement with the experimental observations, a more pronounced and a longer-lived carrier anisotropy is found for the n-doped TDMLG sample compared to the p-doped QFMLG sample.

With the obtained insights from the further simulations above, this can be understood by a combination of doping (fig. C.2) and screening (fig. C.3): The higher the chemical potential μ , the smaller the scattering phase space for c-c and c-ph scattering. The larger the screening ε_s , the slower the c-c scattering. Due to the large value of ε_s in the n-doped TDMLG sample, the decay of the anisotropy is still dominated by c-ph scattering, even in the high fluence regime.

Consistent with the experiment, the simulation from fig. 4.6b in chapter 4 shows a considerably smaller hole anisotropy in the valence band of TDMLG in comparison the respective electron anisotropy in the conduction band. This can be attributed to the non-zero doping of the samples which breaks the symmetry between the electron and hole dynamics. This results in a smaller scattering phase space for c-c and c-ph scattering for the electrons in the conduction band compared to the holes in the valence band.

APPENDIX D

Floquet Theory

In the last several years, the concept of *Floquet engineering* has gained increased popularity [169, 177, 202, 203]. The aim is to change the properties of a quantum material by applying a systematic time-periodic driving protocol to stabilize stationary states that are very different from the undriven eigenstates of the system. The theoretical framework which is used to describe this time-dependent problem is called Floquet theory. Within this framework an effective time-independent Hamiltonian can be found which successfully describes the dynamics and observables on a timescale which is long in comparison to a single period of the drive.

The traces of Floquet theory go back to the 19th century, when M. G. Floquet was studying linear differential equations with periodic coefficients [204]. The concept already had its analogon in solid state physics in the form of Bloch theory: the spatial periodicity of the lattice potential leads to electrons taking the form of Bloch states whose quasi-momentum is only defined up to an inverse lattice vector. Far later, in the 1960s, Floquet theory has been applied to time-periodic quantum systems [205–207]. With no means of being complete, some basic ideas and aspects of Floquet theory will be described here¹.

Floquet states

Floquet theory states that a quantum system described by a time-periodic Hamiltonian

$$H(t) = H(t + T) \tag{D.1}$$

¹Pedagogical descriptions can be found in [177, 190, 203]

possesses generalized stationary eigenstates $|\psi(t)\rangle$ which are solutions to the time-dependent Schroedinger equation

$$H(t)|\psi(t)\rangle = i\hbar\partial_t|\psi\rangle. \quad (\text{D.2})$$

The eigenstates are called Floquet states and have the form

$$|\psi(t)\rangle = |u_n(t)\rangle e^{-\frac{i}{\hbar}\epsilon_n t}, \quad (\text{D.3})$$

with quasienergy ϵ_n and time-periodic *Floquet modes* $|u_n(t)\rangle = |u_n(t+T)\rangle$.

Stroboscopic Floquet Hamiltonian and Micromotions

When studying the dynamics of a time-periodically driven system over time spans that are long compared to a single period, it is useful to introduce the static stroboscopic Floquet Hamiltonian. It is defined such that it generates the time evolution over one period.

$$e^{-iH_F^{t_0}T} \equiv U(t_0+T, t_0) = T e^{-i\int_{t_0}^{t_0+T} dt H(t)} \quad (\text{D.4})$$

The stroboscopic Floquet Hamiltonian, which is found either numerically, perturbatively or exactly, enables one to study the long time-evolution of arbitrary quantum states or observables when probing the system in a stroboscopic fashion only at times $t_0 + nT$: $U(t_0 + nT) = e^{-inH_F^{t_0}T}$. This method allows to ignore fast *micromotions* which describe the temporal evolution of quantum states that happen in between the probing points and occur at the frequency of the driving. Depending on the system (Hamiltonian) and the observables, micromotions can be either small or large.

As seen by its definition, the stroboscopic Floquet Hamiltonian carries a gauge, depending on the starting time t_0 , at which point during a cycle the probing takes place. All stroboscopic Floquet Hamiltonians are related by a unitary transformation

$$H_F^{t'_0} = U^\dagger(t_0, t'_0) H_F^{t_0} U(t_0, t'_0), \quad (\text{D.5})$$

from which it can be concluded that all stroboscopic Hamiltonians have eigenstates with the same quasi-eigenenergies ϵ_n . The Floquet modes $|u_n(t)\rangle$ which were introduced above are given by the orthogonal set of eigenstates of the particular stroboscopic Floquet Hamiltonian at the corresponding starting time t :

$$H_F^{t_0}|u_n(t_0)\rangle = \epsilon_n|u_n(t_0)\rangle \quad (\text{D.6})$$

Effective Floquet Hamiltonian

In contrast to the stroboscopic Floquet Hamiltonian $H_F^{t_0}$ which is gauge-dependent by the requirement of choosing a certain starting time t_0 , a modified gauge-independent version can be found. It is called the effective Floquet Hamiltonian and can be obtained by a unitary transformation which brings the stroboscopic Floquet Hamiltonian in a *micromotion free* frame. Up to a certain order in a high-frequency expansion, the effective Floquet Hamiltonian H_F is given by a starting time t_0 -averaged version of the stroboscopic Floquet Hamiltonian $H_F^{t_0}$, but that is a simplified picture.

$$H_F = U_F^\dagger(t)H(t)U_F(t) - iU_F^\dagger(t)\partial_t U_F(t) \quad (\text{D.7})$$

By construction the unitary operator of the form $U_F(t) = e^{-iK(t)}$ is chosen such that the effective Floquet Hamiltonian H_F is time-independent. The hermitian operator $K(t)$ has been given the intuitive name kick operator, for its purpose of kicking the system from a lab frame into an effective frame.

The effective Hamiltonian allows a very efficient way of addressing the long-time dynamics over several driving periods by separating the time-dependent problem entirely from the short-time dynamics within one driving period. The concept of Floquet engineering is based on modifying the effective Floquet Hamiltonian by a tailored periodic time-dependence.

Finding the effective Floquet Hamiltonian is not as intuitive as the stroboscopic Floquet Hamiltonian. One approach is to use a high-frequency expansion $H_F = \sum_{n=0}^{\infty} H_F^n \frac{1}{\Omega^n}$ where the t_0 -dependence of the Hamiltonian is automatically removed:

$$\begin{aligned} H_F^0 &= H_0 \\ H_F^1 &= \sum_{m=1}^{\infty} \frac{1}{m} [H_m, H_{-m}] \\ H_F^2 &= \sum_{m \neq 0} \left(\frac{[H_{-n}, [H_0, H_n]]}{2n^2} + \sum_{m' \neq (0,n)} \frac{[H_{-m'}, [H_{m'-m}, H_m]]}{3mm'} \right) \end{aligned} \quad (\text{D.8})$$

where $H_n = \frac{1}{T} \int_0^T dt e^{-in\Omega t} H(t)$ are the Fourier components of the (time-periodic) Hamiltonian $H(t)$. The lowest order term H_0 is therefore simply the time-averaged Hamiltonian over one period.

Floquet sidebands

In the same fashion as quasimomentum of Bloch states and the Bloch Hamiltonian is only defined up to an inverse lattice vector, Floquet states and the Floquet Hamiltonian have energy values that are only defined up to a value of the photon energy $\hbar\Omega = \hbar\frac{2\pi}{T}$. For that reason one also speaks of quasienergy and one can choose all quasienergies ϵ_n to lie within the same interval of width $\hbar\Omega$, often called Brillouin zone.

Starting from a known Floquet state $|\psi_n(t)\rangle$, allows rewriting the state in terms of all possible choices of quasienergy which do not alter the phase factor of the Floquet state over a whole time period:

$$|\psi_n(t)\rangle = |u_n(t)\rangle e^{-i\epsilon_n t} = |u_{nm}(t)\rangle e^{-i\epsilon_{nm} t} \quad (\text{D.9})$$

with $\epsilon_{nm} = \epsilon_n + m\hbar\omega$ and $|u_{nm}(t)\rangle = |u_n(t)\rangle e^{im\Omega t}$. Inserting the Floquet modes $|u_{nm}(t)\rangle$ into the time-dependent Schroedinger equation yields the eigenenergies ϵ_{nm} of an extended zone-scheme, as the values of m go from $-\infty$ to $+\infty$.

The Floquet mode of the m -th Brillouin-zone is also called the m -th order sideband of the spectrum for their interpretation of resembling a photondressed version of the undriven eigenstates.

Bibliography

- [1] I. Gierz, F. Calegari, S. Aeschlimann, M. Chávez Cervantes, C. Cacho, R. T. Chapman, E. Springate, S. Link, U. Starke, C. R. Ast, and A. Cavalleri, “Tracking primary thermalization events in graphene with photoemission at extreme time scales,” *Phys. Rev. Lett.*, vol. 115, p. 086803, Aug 2015.
- [2] S. Aeschlimann, R. Krause, M. Chávez-Cervantes, H. Bromberger, R. Jago, E. Malić, A. Al-Temimy, C. Coletti, A. Cavalleri, and I. Gierz, “Ultrafast momentum imaging of pseudospin-flip excitations in graphene,” *Phys. Rev. B*, vol. 96, p. 020301, Jul 2017.
- [3] S. Aeschlimann, M. Chavez-Cervantes, R. Krause, A. Rossi, S. Forti, F. Fabbri, C. Coletti, and I. Gierz, “Direct evidence for efficient ultrafast charge separation in epitaxial ws_2 /graphene heterostructure,” *arXiv:1904.01379*, 2019.
- [4] M. Chávez-Cervantes, R. Krause, S. Aeschlimann, and I. Gierz, “Band structure dynamics in indium wires,” *Phys. Rev. B*, vol. 97, p. 201401, May 2018.
- [5] K. S. Novoselov, A. K. Geim, S. V. Morozov, D. Jiang, Y. Zhang, S. V. Dubonos, I. V. Grigorieva, and A. A. Firsov, “Electric field effect in atomically thin carbon films,” *Science*, vol. 306, no. 5696, pp. 666–669, 2004.
- [6] K. S. Novoselov, D. Jiang, F. Schedin, T. J. Booth, V. V. Khotkevich, S. V. Morozov, and A. K. Geim, “Two-dimensional atomic crystals,” *Proceedings of the National Academy of Sciences*, vol. 102, no. 30, pp. 10451–10453, 2005.
- [7] S. Böhm, “Graphene against corrosion,” *Nature Nanotechnology*, vol. 9, pp. 741 EP –, 10 2014.
- [8] W. Ren and H.-M. Cheng, “The global growth of graphene,” *Nature Nanotechnology*, vol. 9, pp. 726 EP –, 10 2014.
- [9] O. V. Yazyev and Y. P. Chen, “Polycrystalline graphene and other two-dimensional materials,” *Nature nanotechnology*, vol. 9, no. 10, pp. 755–767, 2014.

- [10] K. Novoselov and A. C. Neto, “Two-dimensional crystals-based heterostructures: materials with tailored properties,” *Physica Scripta*, vol. 2012, no. T146, p. 014006, 2012.
- [11] F. Koppens, T. Mueller, P. Avouris, A. Ferrari, M. Vitiello, and M. Polini, “Photodetectors based on graphene, other two-dimensional materials and hybrid systems,” *Nature nanotechnology*, vol. 9, no. 10, p. 780, 2014.
- [12] A. Zurutuza and C. Marinelli, “Challenges and opportunities in graphene commercialization,” *Nature nanotechnology*, vol. 9, no. 10, p. 730, 2014.
- [13] G. Fiori, F. Bonaccorso, G. Iannaccone, T. Palacios, D. Neumaier, A. Seabaugh, S. K. Banerjee, and L. Colombo, “Electronics based on two-dimensional materials,” *Nature nanotechnology*, vol. 9, no. 10, p. 768, 2014.
- [14] J.-H. Ahn and B. H. Hong, “Graphene for displays that bend,” *Nature nanotechnology*, vol. 9, no. 10, p. 737, 2014.
- [15] W. Han, R. K. Kawakami, M. Gmitra, and J. Fabian, “Graphene spintronics,” *Nature nanotechnology*, vol. 9, no. 10, p. 794, 2014.
- [16] B. Radisavljevic, A. Radenovic, J. Brivio, i. V. Giacometti, and A. Kis, “Single-layer mos 2 transistors,” *Nature nanotechnology*, vol. 6, no. 3, p. 147, 2011.
- [17] S. Bae, H. Kim, Y. Lee, X. Xu, J.-S. Park, Y. Zheng, J. Balakrishnan, T. Lei, H. R. Kim, Y. I. Song, *et al.*, “Roll-to-roll production of 30-inch graphene films for transparent electrodes,” *Nature nanotechnology*, vol. 5, no. 8, p. 574, 2010.
- [18] T.-H. Han, Y. Lee, M.-R. Choi, S.-H. Woo, S.-H. Bae, B. H. Hong, J.-H. Ahn, and T.-W. Lee, “Extremely efficient flexible organic light-emitting diodes with modified graphene anode,” *Nature Photonics*, vol. 6, no. 2, p. 105, 2012.
- [19] K. Kim, S.-H. Bae, C. T. Toh, H. Kim, J. H. Cho, D. Whang, T.-W. Lee, B. Özyilmaz, and J.-H. Ahn, “Ultrathin organic solar cells with graphene doped by ferroelectric polarization,” *ACS applied materials & interfaces*, vol. 6, no. 5, pp. 3299–3304, 2014.
- [20] A. Pospischil, M. M. Furchi, and T. Mueller, “Solar-energy conversion and light emission in an atomic monolayer pn diode,” *Nature nanotechnology*, vol. 9, no. 4, pp. 257–261, 2014.
- [21] B. W. Baugher, H. O. Churchill, Y. Yang, and P. Jarillo-Herrero, “Optoelectronic devices based on electrically tunable p–n diodes in a monolayer dichalcogenide,” *Nature nanotechnology*, vol. 9, no. 4, p. 262, 2014.
- [22] M. Liu, X. Yin, E. Ulin-Avila, B. Geng, T. Zentgraf, L. Ju, F. Wang, and X. Zhang, “A graphene-based broadband optical modulator,” *Nature*, vol. 474, no. 7349, p. 64, 2011.
- [23] T. Low and P. Avouris, “Graphene plasmonics for terahertz to mid-infrared applications,” *ACS nano*, vol. 8, no. 2, pp. 1086–1101, 2014.

-
- [24] Z. Sun, T. Hasan, F. Torrisi, D. Popa, G. Privitera, F. Wang, F. Bonaccorso, D. M. Basko, and A. C. Ferrari, “Graphene mode-locked ultrafast laser,” *ACS nano*, vol. 4, no. 2, pp. 803–810, 2010.
- [25] T. Kampfrath, L. Perfetti, F. Schapper, C. Frischkorn, and M. Wolf, “Strongly coupled optical phonons in the ultrafast dynamics of the electronic energy and current relaxation in graphite,” *Physical review letters*, vol. 95, no. 18, p. 187403, 2005.
- [26] D. Sun, Z.-K. Wu, C. Divin, X. Li, C. Berger, W. A. de Heer, P. N. First, and T. B. Norris, “Ultrafast relaxation of excited dirac fermions in epitaxial graphene using optical differential transmission spectroscopy,” *Physical Review Letters*, vol. 101, no. 15, p. 157402, 2008.
- [27] P. A. George, J. Strait, J. Dawlaty, S. Shivaraman, M. Chandrashekar, F. Rana, and M. G. Spencer, “Ultrafast optical-pump terahertz-probe spectroscopy of the carrier relaxation and recombination dynamics in epitaxial graphene,” *Nano letters*, vol. 8, no. 12, pp. 4248–4251, 2008.
- [28] M. Breusing, C. Ropers, and T. Elsaesser, “Ultrafast carrier dynamics in graphite,” *Physical review letters*, vol. 102, no. 8, p. 086809, 2009.
- [29] M. Breusing, S. Kuehn, T. Winzer, E. Malić, F. Milde, N. Severin, J. Rabe, C. Ropers, A. Knorr, and T. Elsaesser, “Ultrafast nonequilibrium carrier dynamics in a single graphene layer,” *Physical Review B*, vol. 83, no. 15, p. 153410, 2011.
- [30] H. Wang, J. H. Strait, P. A. George, S. Shivaraman, V. B. Shields, M. Chandrashekar, J. Hwang, F. Rana, M. G. Spencer, C. S. Ruiz-Vargas, *et al.*, “Ultrafast relaxation dynamics of hot optical phonons in graphene,” *Applied Physics Letters*, vol. 96, no. 8, p. 081917, 2010.
- [31] T. Li, L. Luo, M. Hupalo, J. Zhang, M. Tringides, J. Schmalian, and J. Wang, “Femtosecond population inversion and stimulated emission of dense dirac fermions in graphene,” *Physical Review Letters*, vol. 108, no. 16, p. 167401, 2012.
- [32] C. H. Lui, K. F. Mak, J. Shan, T. F. Heinz, *et al.*, “Ultrafast photoluminescence from graphene,” *Physical review letters*, vol. 105, no. 12, p. 127404, 2010.
- [33] R. J. Stöhr, R. Kolesov, J. Pflaum, and J. Wrachtrup, “Fluorescence of laser-created electron-hole plasma in graphene,” *Physical Review B*, vol. 82, no. 12, p. 121408, 2010.
- [34] W.-T. Liu, S. Wu, P. Schuck, M. Salmeron, Y. Shen, and F. Wang, “Nonlinear broadband photoluminescence of graphene induced by femtosecond laser irradiation,” *Physical Review B*, vol. 82, no. 8, p. 081408, 2010.
- [35] I. Gierz, J. C. Petersen, M. Mitrano, C. Cacho, I. C. E. Turcu, E. Springate, A. Stöhr, A. Köhler, U. Starke, and A. Cavalleri, “Snapshots of non-equilibrium dirac carrier distributions in graphene,” *Nature Materials*, vol. 12, pp. 1119 EP –, 10 2013.

- [36] I. Gierz, S. Link, U. Starke, and A. Cavalleri, “Non-equilibrium dirac carrier dynamics in graphene investigated with time-and angle-resolved photoemission spectroscopy,” *Faraday discussions*, vol. 171, pp. 311–321, 2014.
- [37] I. Gierz, M. Mitrano, J. C. Petersen, C. Cacho, I. C. E. Turcu, E. Springate, A. Stöhr, A. Köhler, U. Starke, and A. Cavalleri, “Population inversion in monolayer and bilayer graphene,” *Journal of Physics: Condensed Matter*, vol. 27, no. 16, p. 164204, 2015.
- [38] I. Gierz, M. Mitrano, H. Bromberger, C. Cacho, R. Chapman, E. Springate, S. Link, U. Starke, B. Sachs, M. Eckstein, T. O. Wehling, M. I. Katsnelson, A. Lichtenstein, and A. Cavalleri, “Phonon-pump extreme-ultraviolet-photoemission probe in graphene: Anomalous heating of dirac carriers by lattice deformation,” *Phys. Rev. Lett.*, vol. 114, p. 125503, Mar 2015.
- [39] I. Gierz and A. Cavalleri, “Electronic-structural dynamics in graphene,” *Structural Dynamics*, vol. 3, no. 5, p. 051301, 2016.
- [40] E. Pomarico, M. Mitrano, H. Bromberger, M. A. Sentef, A. Al-Temimy, C. Coletti, A. Stöhr, S. Link, U. Starke, C. Cacho, R. Chapman, E. Springate, A. Cavalleri, and I. Gierz, “Enhanced electron-phonon coupling in graphene with periodically distorted lattice,” *Phys. Rev. B*, vol. 95, p. 024304, Jan 2017.
- [41] I. Gierz, “Probing carrier dynamics in photo-excited graphene with time-resolved arpes,” *Journal of Electron Spectroscopy and Related Phenomena*, vol. 219, pp. 53 – 56, 2017. SI: The electronic structure of 2D and layered materials.
- [42] J. C. Johannsen, S. Ulstrup, F. Cilento, A. Crepaldi, M. Zacchigna, C. Cacho, I. E. Turcu, E. Springate, F. Fromm, C. Raidel, *et al.*, “Direct view of hot carrier dynamics in graphene,” *Physical Review Letters*, vol. 111, no. 2, p. 027403, 2013.
- [43] S. Ulstrup, J. C. Johannsen, F. Cilento, J. A. Miwa, A. Crepaldi, M. Zacchigna, C. Cacho, R. Chapman, E. Springate, S. Mammadov, *et al.*, “Ultrafast dynamics of massive dirac fermions in bilayer graphene,” *Physical review letters*, vol. 112, no. 25, p. 257401, 2014.
- [44] S. Ulstrup, J. C. Johannsen, A. Crepaldi, F. Cilento, M. Zacchigna, C. Cacho, R. T. Chapman, E. Springate, F. Fromm, C. Raidel, *et al.*, “Ultrafast electron dynamics in epitaxial graphene investigated with time-and angle-resolved photoemission spectroscopy,” *Journal of Physics: Condensed Matter*, vol. 27, no. 16, p. 164206, 2015.
- [45] J. C. Johannsen, S. Ulstrup, A. Crepaldi, F. Cilento, M. Zacchigna, J. A. Miwa, C. Cacho, R. T. Chapman, E. Springate, F. Fromm, *et al.*, “Tunable carrier multiplication and cooling in graphene,” *Nano letters*, vol. 15, no. 1, pp. 326–331, 2014.
- [46] A. Stange, C. Sohrt, T. Rohwer, S. Hellmann, G. Rohde, L. Kipp, K. Rossnagel, and M. Bauer, “A direct view onto the carrier dynamics in graphite at the h point,” in *EPJ Web of Conferences*, vol. 41, p. 04022, EDP Sciences, 2013.

-
- [47] A. Stange, C. Sohr, L. Yang, G. Rohde, K. Janssen, P. Hein, L.-P. Oloff, K. Hanff, K. Rossnagel, and M. Bauer, “Hot electron cooling in graphite: Supercollision versus hot phonon decay,” *Physical Review B*, vol. 92, no. 18, p. 184303, 2015.
- [48] L. Fritz, J. Schmalian, M. Müller, and S. Sachdev, “Quantum critical transport in clean graphene,” *Phys. Rev. B*, vol. 78, p. 085416, Aug 2008.
- [49] T. Winzer, A. Knorr, and E. Malic, “Carrier multiplication in graphene,” *Nano letters*, vol. 10, no. 12, pp. 4839–4843, 2010.
- [50] T. Winzer and E. Malić, “Impact of auger processes on carrier dynamics in graphene,” *Physical Review B*, vol. 85, no. 24, p. 241404, 2012.
- [51] A. Tomadin, D. Brida, G. Cerullo, A. C. Ferrari, and M. Polini, “Nonequilibrium dynamics of photoexcited electrons in graphene: Collinear scattering, auger processes, and the impact of screening,” *Physical Review B*, vol. 88, no. 3, p. 035430, 2013.
- [52] M. Trushin, “Collinear scattering of photoexcited carriers in graphene,” *Phys. Rev. B*, vol. 94, p. 205306, Nov 2016.
- [53] A. F. Page, J. M. Hamm, and O. Hess, “Polarization and plasmons in hot photoexcited graphene,” *Physical Review B*, vol. 97, no. 4, p. 045428, 2018.
- [54] J. M. Hamm, A. F. Page, J. Bravo-Abad, F. J. Garcia-Vidal, and O. Hess, “Nonequilibrium plasmon emission drives ultrafast carrier relaxation dynamics in photoexcited graphene,” *Physical Review B*, vol. 93, no. 4, p. 041408, 2016.
- [55] J. He, N. Kumar, M. Z. Bellus, H.-Y. Chiu, D. He, Y. Wang, and H. Zhao, “Electron transfer and coupling in graphene–tungsten disulfide van der waals heterostructures,” *Nature Communications*, vol. 5, pp. 5622 EP –, 11 2014.
- [56] N. Huo, Z. Wei, X. Meng, J. Kang, F. Wu, S.-S. Li, S.-H. Wei, and J. Li, “Interlayer coupling and optoelectronic properties of ultrathin two-dimensional heterostructures based on graphene, mos 2 and ws 2,” *Journal of Materials Chemistry C*, vol. 3, no. 21, pp. 5467–5473, 2015.
- [57] M. Massicotte, P. Schmidt, F. Violla, K. G. Schädler, A. Reserbat-Plantey, K. Watanabe, T. Taniguchi, K.-J. Tielrooij, and F. H. Koppens, “Picosecond photoresponse in van der waals heterostructures,” *Nature nanotechnology*, vol. 11, no. 1, p. 42, 2016.
- [58] H. M. Hill, A. F. Rigosi, A. Raja, A. Chernikov, C. Roquelet, and T. F. Heinz, “Exciton broadening in ws 2/graphene heterostructures,” *Physical Review B*, vol. 96, no. 20, p. 205401, 2017.
- [59] L. Yuan, T.-F. Chung, A. Kuc, Y. Wan, Y. Xu, Y. P. Chen, T. Heine, and L. Huang, “Photocarrier generation from interlayer charge-transfer transitions in ws2-graphene heterostructures,” *Science Advances*, vol. 4, no. 2, 2018.

- [60] A. Avsar, J. Y. Tan, T. Taychatanapat, J. Balakrishnan, G. Koon, Y. Yeo, J. Lahiri, A. Carvalho, A. Rodin, E. O’Farrell, *et al.*, “Spin–orbit proximity effect in graphene,” *Nature communications*, vol. 5, p. 4875, 2014.
- [61] T. Kaloni, L. Kou, T. Frauenheim, and U. Schwingenschlögl, “Quantum spin hall states in graphene interacting with ws_2 or wse_2 ,” *Applied Physics Letters*, vol. 105, no. 23, p. 233112, 2014.
- [62] T. Wakamura, F. Reale, P. Palczynski, S. Guéron, C. Mattevi, and H. Bouchiat, “Strong anisotropic spin-orbit interaction induced in graphene by monolayer ws_2 ,” *Physical review letters*, vol. 120, no. 10, p. 106802, 2018.
- [63] T. Oka and H. Aoki, “Photovoltaic hall effect in graphene,” *Phys. Rev. B*, vol. 79, p. 081406, Feb 2009.
- [64] P. R. Wallace, “The band theory of graphite,” *Phys. Rev.*, vol. 71, pp. 622–634, May 1947.
- [65] M. Y. Kharitonov and K. B. Efetov, “Electron screening and excitonic condensation in double-layer graphene systems,” *Physical Review B*, vol. 78, no. 24, p. 241401, 2008.
- [66] I. Aleiner, D. Kharzeev, and A. Tsvelik, “Spontaneous symmetry breaking in graphene subjected to an in-plane magnetic field,” *Physical Review B*, vol. 76, no. 19, p. 195415, 2007.
- [67] B. Bezzerides and D. DuBois, “Many-body theory for quantum kinetic equations,” *Physical Review*, vol. 168, no. 1, p. 233, 1968.
- [68] M. I. Katsnelson, K. S. Novoselov, and A. K. Geim, “Chiral tunnelling and the klein paradox in graphene,” *Nature Physics*, vol. 2, pp. 620 EP –, 08 2006.
- [69] M. Schütt, *Coulomb Interaction and Transport in Graphene Structures*. PhD thesis, Karlsruhe Institute of Technology (KIT), 2013.
- [70] A. H. Castro Neto, F. Guinea, N. M. R. Peres, K. S. Novoselov, and A. K. Geim, “The electronic properties of graphene,” *Rev. Mod. Phys.*, vol. 81, pp. 109–162, Jan 2009.
- [71] B. Wunsch, T. Stauber, F. Sols, and F. Guinea, “Dynamical polarization of graphene at finite doping,” *New Journal of Physics*, vol. 8, no. 12, p. 318, 2006.
- [72] E. Hwang and S. D. Sarma, “Dielectric function, screening, and plasmons in two-dimensional graphene,” *Physical Review B*, vol. 75, no. 20, p. 205418, 2007.
- [73] H. Yan, T. Low, W. Zhu, Y. Wu, M. Freitag, X. Li, F. Guinea, P. Avouris, and F. Xia, “Damping pathways of mid-infrared plasmons in graphene nanostructures,” *Nature Photonics*, vol. 7, pp. 394 EP –, 04 2013.

-
- [74] P. A. Huidobro, M. Kraft, S. A. Maier, and J. B. Pendry, "Graphene as a tunable anisotropic or isotropic plasmonic metasurface," *ACS Nano*, vol. 10, no. 5, pp. 5499–5506, 2016. PMID: 27092391.
- [75] U. Monteverde, J. Pal, M. Migliorato, M. Missous, U. Bangert, R. Zan, R. Kashtiban, and D. Powell, "Under pressure: Control of strain, phonons and bandgap opening in rippled graphene," *Carbon*, vol. 91, pp. 266 – 274, 2015.
- [76] M. Mohr, J. Maultzsch, E. Dobardžić, S. Reich, I. Milošević, M. Damnjanović, A. Bosak, M. Krisch, and C. Thomsen, "Phonon dispersion of graphite by inelastic x-ray scattering," *Phys. Rev. B*, vol. 76, p. 035439, Jul 2007.
- [77] S. Piscanec, M. Lazzeri, F. Mauri, A. C. Ferrari, and J. Robertson, "Kohn anomalies and electron-phonon interactions in graphite," *Phys. Rev. Lett.*, vol. 93, p. 185503, Oct 2004.
- [78] E. Malic, T. Winzer, E. Bobkin, and A. Knorr, "Microscopic theory of absorption and ultrafast many-particle kinetics in graphene," *Physical Review B*, vol. 84, no. 20, p. 205406, 2011.
- [79] H. Yan, D. Song, K. F. Mak, I. Chatzakis, J. Maultzsch, and T. F. Heinz, "Time-resolved raman spectroscopy of optical phonons in graphite: Phonon anharmonic coupling and anomalous stiffening," *Physical Review B*, vol. 80, no. 12, p. 121403, 2009.
- [80] K. Kang, D. Abdula, D. G. Cahill, and M. Shim, "Lifetimes of optical phonons in graphene and graphite by time-resolved incoherent anti-stokes raman scattering," *Physical Review B*, vol. 81, no. 16, p. 165405, 2010.
- [81] J. C. Song, M. Y. Reizer, and L. S. Levitov, "Disorder-assisted electron-phonon scattering and cooling pathways in graphene," *Physical Review Letters*, vol. 109, no. 10, p. 106602, 2012.
- [82] M. W. Graham, S.-F. Shi, D. C. Ralph, J. Park, and P. L. McEuen, "Photocurrent measurements of supercollision cooling in graphene," *Nature Physics*, vol. 9, no. 2, p. 103, 2013.
- [83] A. Betz, S. H. Jhang, E. Pallecchi, R. Ferreira, G. Fève, J.-M. Berroir, and B. Plaçais, "Supercollision cooling in undoped graphene," *Nature Physics*, vol. 9, no. 2, p. 109, 2013.
- [84] R. R. Nair, P. Blake, A. N. Grigorenko, K. S. Novoselov, T. J. Booth, T. Stauber, N. M. Peres, and A. K. Geim, "Fine structure constant defines visual transparency of graphene," *Science*, vol. 320, no. 5881, pp. 1308–1308, 2008.
- [85] S. Gilbertson, G. L. Dakovski, T. Durakiewicz, J.-X. Zhu, K. M. Dani, A. D. Mohite, A. Dattelbaum, and G. Rodriguez, "Tracing ultrafast separation and coalescence of carrier distributions in graphene with time-resolved photoemission," *The Journal of Physical Chemistry Letters*, vol. 3, pp. 64–68, 01 2012.

- [86] D. Brida, A. Tomadin, C. Manzoni, Y. J. Kim, A. Lombardo, S. Milana, R. R. Nair, K. Novoselov, A. C. Ferrari, G. Cerullo, *et al.*, “Ultrafast collinear scattering and carrier multiplication in graphene,” *Nature communications*, vol. 4, p. 1987, 2013.
- [87] T. Plotzing, T. Winzer, E. Malic, D. Neumaier, A. Knorr, and H. Kurz, “Experimental verification of carrier multiplication in graphene,” *Nano letters*, vol. 14, no. 9, pp. 5371–5375, 2014.
- [88] T. Winzer, E. Malić, and A. Knorr, “Microscopic mechanism for transient population inversion and optical gain in graphene,” *Physical Review B*, vol. 87, no. 16, p. 165413, 2013.
- [89] V. Nicolosi, M. Chhowalla, M. G. Kanatzidis, M. S. Strano, and J. N. Coleman, “Liquid exfoliation of layered materials,” *Science*, vol. 340, no. 6139, p. 1226419, 2013.
- [90] X. Li, W. Cai, J. An, S. Kim, J. Nah, D. Yang, R. Piner, A. Velamakanni, I. Jung, E. Tutuc, *et al.*, “Large-area synthesis of high-quality and uniform graphene films on copper foils,” *science*, vol. 324, no. 5932, pp. 1312–1314, 2009.
- [91] A. Bostwick, T. Ohta, T. Seyller, K. Horn, and E. Rotenberg, “Quasiparticle dynamics in graphene,” *Nature Physics*, vol. 3, pp. 36 EP –, 12 2006.
- [92] C. Hwang, C.-H. Park, D. A. Siegel, A. V. Fedorov, S. G. Louie, and A. Lanzara, “Direct measurement of quantum phases in graphene via photoemission spectroscopy,” *Phys. Rev. B*, vol. 84, p. 125422, Sep 2011.
- [93] I. Gierz, J. Henk, H. Höchst, C. R. Ast, and K. Kern, “Illuminating the dark corridor in graphene: Polarization dependence of angle-resolved photoemission spectroscopy on graphene,” *Phys. Rev. B*, vol. 83, p. 121408, Mar 2011.
- [94] S. Eich, A. Stange, A. Carr, J. Urbancic, T. Popmintchev, M. Wiesenmayer, K. Jansen, A. Ruffing, S. Jakobs, T. Rohwer, *et al.*, “Time-and angle-resolved photoemission spectroscopy with optimized high-harmonic pulses using frequency-doubled ti: Sapphire lasers,” *Journal of Electron Spectroscopy and Related Phenomena*, vol. 195, pp. 231–236, 2014.
- [95] A. McPherson, “A. mcpherson, g. gibson, h. jara, u. johann, ts luk, ia mcintyre, k. boyer, and ck rhodes, j. opt. soc. am. b 4, 595 (1987).,” *J. Opt. Soc. Am. B*, vol. 4, p. 595, 1987.
- [96] M. Ferray, “M. ferray, a. l’huillier, xf li, la lomppe, g. mainfray, and c. manus, j. phys. b 21, 131 (1988).,” *J. Phys. B*, vol. 21, p. L31, 1988.
- [97] F. Frassetto, S. Bonora, P. Villoresi, L. Poletto, E. Springate, C. Froud, I. Turcu, A. Langley, D. Wolff, J. Collier, *et al.*, “Design and characterization of the xuv monochromator for ultrashort pulses at the artemis facility,” in *Advances in X-Ray/EUV Optics and Components III*, vol. 7077, p. 707713, International Society for Optics and Photonics, 2008.

-
- [98] F. Frassetto, C. Cacho, C. A. Froud, I. E. Turcu, P. Villorosi, W. A. Bryan, E. Springate, and L. Poletto, “Single-grating monochromator for extreme-ultraviolet ultrashort pulses,” *Optics express*, vol. 19, no. 20, pp. 19169–19181, 2011.
- [99] R. L. Fork, C. V. Shank, C. Hirlimann, R. Yen, and W. J. Tomlinson, “Femtosecond white-light continuum pulses,” *Opt. Lett.*, vol. 8, pp. 1–3, Jan 1983.
- [100] J. Graf, S. Hellmann, C. Jozwiak, C. Smallwood, Z. Hussain, R. Kaindl, L. Kipp, K. Rossnagel, and A. Lanzara, “Vacuum space charge effect in laser-based solid-state photoemission spectroscopy,” *Journal of applied physics*, vol. 107, no. 1, p. 014912, 2010.
- [101] J. Faure, J. Mauchain, E. Papalazarou, W. Yan, J. Pinon, M. Marsi, and L. Perfetti, “Full characterization and optimization of a femtosecond ultraviolet laser source for time and angle-resolved photoemission on solid surfaces,” *Review of Scientific Instruments*, vol. 83, no. 4, p. 043109, 2012.
- [102] B. Frietsch, R. Carley, K. Döbrich, C. Gahl, M. Teichmann, O. Schwarzkopf, P. Wernet, and M. Weinelt, “A high-order harmonic generation apparatus for time-and angle-resolved photoelectron spectroscopy,” *Review of Scientific Instruments*, vol. 84, no. 7, p. 075106, 2013.
- [103] Y. Ishida, T. Otsu, A. Ozawa, K. Yaji, S. Tani, S. Shin, and Y. Kobayashi, “High repetition pump-and-probe photoemission spectroscopy based on a compact fiber laser system,” *Review of Scientific Instruments*, vol. 87, no. 12, p. 123902, 2016.
- [104] L.-P. Oloff, K. Hanff, A. Stange, G. Rohde, F. Diekmann, M. Bauer, and K. Rossnagel, “Pump laser-induced space-charge effects in hhg-driven time-and angle-resolved photoelectron spectroscopy,” *Journal of Applied Physics*, vol. 119, no. 22, p. 225106, 2016.
- [105] M. Aeschlimann, C. Schmuttenmaer, H. Elsayed-Ali, R. Miller, J. Cao, Y. Gao, and D. Mantell, “Observation of surface enhanced multiphoton photoemission from metal surfaces in the short pulse limit,” *The Journal of chemical physics*, vol. 102, no. 21, pp. 8606–8613, 1995.
- [106] S. Ulstrup, J. C. Johannsen, F. Cilento, A. Crepaldi, J. A. Miwa, M. Zacchigna, C. Cacho, R. T. Chapman, E. Springate, F. Fromm, *et al.*, “Ramifications of optical pumping on the interpretation of time-resolved photoemission experiments on graphene,” *Journal of Electron Spectroscopy and Related Phenomena*, vol. 200, pp. 340–346, 2015.
- [107] G. Saathoff, L. Miaja-Avila, M. Aeschlimann, M. M. Murnane, and H. C. Kapteyn, “Laser-assisted photoemission from surfaces,” *Phys. Rev. A*, vol. 77, p. 022903, Feb 2008.
- [108] J. H. Buss, J. Maklar, F. Joucken, H. Wang, Y. Xu, S.-K. Mo, A. Lanzara, and R. A. Kaindl, “Ultrafast extreme-ultraviolet arpes studies of electronic dynamics in two-dimensional materials,” in *Ultrafast Phenomena and Nanophotonics XXI*, vol. 10102, p. 101020I, International Society for Optics and Photonics, 2017.

- [109] L. B. Madsen, “Strong-field approximation in laser-assisted dynamics,” *American journal of physics*, vol. 73, no. 1, pp. 57–62, 2005.
- [110] S. Forti, K. V. Emtsev, C. Coletti, A. A. Zakharov, C. Riedl, and U. Starke, “Large-area homogeneous quasifree standing epitaxial graphene on sic(0001): Electronic and structural characterization,” *Phys. Rev. B*, vol. 84, p. 125449, Sep 2011.
- [111] A. L. Walter, A. Bostwick, K.-J. Jeon, F. Speck, M. Ostler, T. Seyller, L. Moreschini, Y. J. Chang, M. Polini, R. Asgari, *et al.*, “Effective screening and the plasmaron bands in graphene,” *Physical Review B*, vol. 84, no. 8, p. 085410, 2011.
- [112] C. Hwang, D. A. Siegel, S.-K. Mo, W. Regan, A. Ismach, Y. Zhang, A. Zettl, and A. Lanzara, “Fermi velocity engineering in graphene by substrate modification,” *Scientific Reports*, vol. 2, pp. 590 EP –, 08 2012.
- [113] J. C. Johannsen, S. Ulstrup, M. Bianchi, R. Hatch, D. Guan, F. Mazzola, L. Hornekær, F. Fromm, C. Raidel, T. Seyller, *et al.*, “Electron–phonon coupling in quasi-free-standing graphene,” *Journal of physics: Condensed matter*, vol. 25, no. 9, p. 094001, 2013.
- [114] F. Mazzola, J. W. Wells, R. Yakimova, S. Ulstrup, J. A. Miwa, R. Balog, M. Bianchi, M. Leandersson, J. Adell, P. Hofmann, and T. Balasubramanian, “Kinks in the σ band of graphene induced by electron-phonon coupling,” *Phys. Rev. Lett.*, vol. 111, p. 216806, Nov 2013.
- [115] C. Straßer, B. M. Ludbrook, G. Levy, A. J. Macdonald, S. A. Burke, T. O. Wehling, K. Kern, A. Damascelli, and C. R. Ast, “Long- versus short-range scattering in doped epitaxial graphene,” *Nano Letters*, vol. 15, no. 5, pp. 2825–2829, 2015. PMID: 25822076.
- [116] F. Mazzola, T. Frederiksen, T. Balasubramanian, P. Hofmann, B. Hellsing, and J. W. Wells, “Strong electron-phonon coupling in the σ band of graphene,” *Physical Review B*, vol. 95, no. 7, p. 075430, 2017.
- [117] I. Pletikosić, M. Kralj, P. Pervan, R. Brako, J. Coraux, A. N’diaye, C. Busse, and T. Michely, “Dirac cones and minigaps for graphene on ir (111),” *Physical Review Letters*, vol. 102, no. 5, p. 056808, 2009.
- [118] X. Chen, L. Zhang, and S. Chen, “Large area cvd growth of graphene,” *Synthetic Metals*, vol. 210, pp. 95–108, 2015.
- [119] C. Riedl, C. Coletti, T. Iwasaki, A. A. Zakharov, and U. Starke, “Quasi-free-standing epitaxial graphene on sic obtained by hydrogen intercalation,” *Phys. Rev. Lett.*, vol. 103, p. 246804, Dec 2009.
- [120] S. Forti and U. Starke, “Epitaxial graphene on sic: from carrier density engineering to quasi-free standing graphene by atomic intercalation,” *Journal of Physics D: Applied Physics*, vol. 47, no. 9, p. 094013, 2014.

-
- [121] A. Van Bommel, J. Crombeen, and A. Van Tooren, “Leed and auger electron observations of the sic (0001) surface,” *Surface Science*, vol. 48, no. 2, pp. 463–472, 1975.
- [122] U. Starke, S. Forti, K. Emtsev, and C. Coletti, “Engineering the electronic structure of epitaxial graphene by transfer doping and atomic intercalation,” *MRS Bulletin*, vol. 37, no. 12, pp. 1177–1186, 2012.
- [123] A. Rossi, H. Büch, C. Di Rienzo, V. Miseikis, D. Convertino, A. Al-Temimy, V. Voliani, M. Gemmi, V. Piazza, and C. Coletti, “Scalable synthesis of ws₂ on graphene and h-bn: an all-2d platform for light-matter transduction,” *2D Materials*, vol. 3, no. 3, p. 031013, 2016.
- [124] S. Forti, A. Rossi, H. Büch, T. Cavallucci, F. Bisio, A. Sala, T. O. Mentş, A. Locatelli, M. Magnozzi, M. Canepa, *et al.*, “Electronic properties of single-layer tungsten disulfide on epitaxial graphene on silicon carbide,” *Nanoscale*, vol. 9, no. 42, pp. 16412–16419, 2017.
- [125] R. Nitsche, “The growth of single crystals of binary and ternary chalcogenides by chemical transport reactions,” *Journal of Physics and Chemistry of Solids*, vol. 17, no. 1, pp. 163 – 165, 1960.
- [126] M. Mittendorff, T. Winzer, E. Malic, A. Knorr, C. Berger, W. A. de Heer, H. Schneider, M. Helm, and S. Winnerl, “Anisotropy of excitation and relaxation of photogenerated charge carriers in graphene,” *Nano Letters*, vol. 14, no. 3, pp. 1504–1507, 2014. PMID: 24559191.
- [127] X.-Q. Yan, J. Yao, Z.-B. Liu, X. Zhao, X.-D. Chen, C. Gao, W. Xin, Y. Chen, and J.-G. Tian, “Evolution of anisotropic-to-isotropic photoexcited carrier distribution in graphene,” *Physical Review B*, vol. 90, no. 13, p. 134308, 2014.
- [128] E. L. Shirley, L. Terminello, A. Santoni, and F. Himpsel, “Brillouin-zone-selection effects in graphite photoelectron angular distributions,” *Physical Review B*, vol. 51, no. 19, p. 13614, 1995.
- [129] M. Trushin and J. Schliemann, “Anisotropic photoconductivity in graphene,” *EPL (Europhysics Letters)*, vol. 96, no. 3, p. 37006, 2011.
- [130] M. Trushin, A. Grupp, G. Soavi, A. Budweg, D. De Fazio, U. Sassi, A. Lombardo, A. C. Ferrari, W. Belzig, A. Leitenstorfer, *et al.*, “Ultrafast pseudospin dynamics in graphene,” *Physical Review B*, vol. 92, no. 16, p. 165429, 2015.
- [131] J. König-Otto, M. Mittendorff, T. Winzer, F. Kadi, E. Malic, A. Knorr, C. Berger, W. de Heer, A. Pashkin, H. Schneider, *et al.*, “Slow noncollinear coulomb scattering in the vicinity of the dirac point in graphene,” *Physical review letters*, vol. 117, no. 8, p. 087401, 2016.

- [132] E. Malic, T. Winzer, and A. Knorr, “Efficient orientational carrier relaxation in optically excited graphene,” *Applied Physics Letters*, vol. 101, no. 21, p. 213110, 2012.
- [133] A. Satou, V. Ryzhii, and T. Otsuji, “Effects of carrier-carrier scattering on population inversion in graphene under pulse photoexcitation,” in *Journal of Physics: Conference Series*, vol. 584, p. 012018, IOP Publishing, 2015.
- [134] H. Daimon, S. Imada, H. Nishimoto, and S. Suga, “Structure factor in photoemission from valence band,” *Journal of Electron Spectroscopy and Related Phenomena*, vol. 76, pp. 487–492, 1995. Proceedings of the Sixth International Conference on Electron Spectroscopy.
- [135] A. Bostwick, T. Ohta, J. L. McChesney, K. V. Emtsev, T. Seyller, K. Horn, and E. Rotenberg, “Symmetry breaking in few layer graphene films,” *New Journal of Physics*, vol. 9, no. 10, p. 385, 2007.
- [136] S. Ulstrup, J. C. Johannsen, M. Grioni, and P. Hofmann, “Extracting the temperature of hot carriers in time-and angle-resolved photoemission,” *Review of Scientific Instruments*, vol. 85, no. 1, p. 013907, 2014.
- [137] M. Lindberg and S. W. Koch, “Effective bloch equations for semiconductors,” *Physical Review B*, vol. 38, no. 5, p. 3342, 1988.
- [138] H. Haug and S. W. Koch, *Quantum Theory of the Optical and Electronic Properties of Semiconductors: Fifth Edition*. World Scientific Publishing Company, 2009.
- [139] F. Rossi and T. Kuhn, “Theory of ultrafast phenomena in photoexcited semiconductors,” *Reviews of Modern Physics*, vol. 74, no. 3, p. 895, 2002.
- [140] A. Knorr, S. Hughes, T. Stroucken, and S. Koch, “Theory of ultrafast spatio-temporal dynamics in semiconductor heterostructures,” *Chemical physics*, vol. 210, no. 1-2, pp. 27–47, 1996.
- [141] M. Kira and S. Koch, “Many-body correlations and excitonic effects in semiconductor spectroscopy,” *Progress in quantum electronics*, vol. 30, no. 5, pp. 155–296, 2006.
- [142] E. Malic and A. Knorr, *Graphene and Carbon Nanotubes: Ultrafast Optics and Relaxation Dynamics*. John Wiley & Sons, 2013.
- [143] T. Mueller, F. Xia, and P. Avouris, “Graphene photodetectors for high-speed optical communications,” *Nature photonics*, vol. 4, no. 5, p. 297, 2010.
- [144] F. Bonaccorso, Z. Sun, T. Hasan, and A. Ferrari, “Graphene photonics and optoelectronics,” *Nature photonics*, vol. 4, no. 9, p. 611, 2010.
- [145] N. M. Gabor, J. C. Song, Q. Ma, N. L. Nair, T. Taychatanapat, K. Watanabe, T. Taniguchi, L. S. Levitov, and P. Jarillo-Herrero, “Hot carrier-assisted intrinsic photoresponse in graphene,” *Science*, vol. 334, no. 6056, pp. 648–652, 2011.

-
- [146] D. Sun, G. Aivazian, A. M. Jones, J. S. Ross, W. Yao, D. Cobden, and X. Xu, “Ultrafast hot-carrier-dominated photocurrent in graphene,” *Nature nanotechnology*, vol. 7, no. 2, p. 114, 2012.
- [147] T. J. Echtermeyer, P. Nene, M. Trushin, R. V. Gorbachev, A. L. Eiden, S. Milana, Z. Sun, J. Schliemann, E. Lidorikis, K. S. Novoselov, *et al.*, “Photothermoelectric and photoelectric contributions to light detection in metal–graphene–metal photodetectors,” *Nano letters*, vol. 14, no. 7, pp. 3733–3742, 2014.
- [148] A. K. Geim and I. V. Grigorieva, “Van der waals heterostructures,” *Nature*, vol. 499, no. 7459, p. 419, 2013.
- [149] K. Novoselov, A. Mishchenko, A. Carvalho, and A. C. Neto, “2d materials and van der waals heterostructures,” *Science*, vol. 353, no. 6298, p. aac9439, 2016.
- [150] Y. Liu, N. O. Weiss, X. Duan, H.-C. Cheng, Y. Huang, and X. Duan, “Van der waals heterostructures and devices,” *Nature Reviews Materials*, vol. 1, no. 9, p. 16042, 2016.
- [151] T. Georgiou, R. Jalil, B. D. Belle, L. Britnell, R. V. Gorbachev, S. V. Morozov, Y.-J. Kim, A. Gholinia, S. J. Haigh, O. Makarovskiy, *et al.*, “Vertical field-effect transistor based on graphene–ws 2 heterostructures for flexible and transparent electronics,” *Nature nanotechnology*, vol. 8, no. 2, p. 100, 2013.
- [152] Z. Li, C. Cheng, N. Dong, C. Romero, Q. Lu, J. Wang, J. R. V. de Aldana, Y. Tan, and F. Chen, “Q-switching of waveguide lasers based on graphene/ws 2 van der waals heterostructure,” *Photonics Research*, vol. 5, no. 5, pp. 406–410, 2017.
- [153] Z. Zhu, Y. Cheng, and U. Schwingenschlögl, “Giant spin-orbit-induced spin splitting in two-dimensional transition-metal dichalcogenide semiconductors,” *Physical Review B*, vol. 84, no. 15, p. 153402, 2011.
- [154] Q. H. Wang, K. Kalantar-Zadeh, A. Kis, J. N. Coleman, and M. S. Strano, “Electronics and optoelectronics of two-dimensional transition metal dichalcogenides,” *Nature nanotechnology*, vol. 7, no. 11, p. 699, 2012.
- [155] K. S. Novoselov, A. K. Geim, S. V. Morozov, D. Jiang, M. I. Katsnelson, I. V. Grigorieva, S. V. Dubonos, and A. A. Firsov, “Two-dimensional gas of massless dirac fermions in graphene,” *Nature*, vol. 438, pp. 197 EP –, 11 2005.
- [156] V. Carozo, Y. Wang, K. Fujisawa, B. R. Carvalho, A. McCreary, S. Feng, Z. Lin, C. Zhou, N. Perea-López, A. L. Elías, *et al.*, “Optical identification of sulfur vacancies: Bound excitons at the edges of monolayer tungsten disulfide,” *Science advances*, vol. 3, no. 4, p. e1602813, 2017.
- [157] X. Hong, J. Kim, S.-F. Shi, Y. Zhang, C. Jin, Y. Sun, S. Tongay, J. Wu, Y. Zhang, and F. Wang, “Ultrafast charge transfer in atomically thin mos 2/ws 2 heterostructures,” *Nature nanotechnology*, vol. 9, no. 9, p. 682, 2014.

- [158] F. Ceballos, M. Z. Bellus, H.-Y. Chiu, and H. Zhao, "Ultrafast charge separation and indirect exciton formation in a mos₂-mose₂ van der waals heterostructure," *ACS nano*, vol. 8, no. 12, pp. 12717–12724, 2014.
- [159] P. Rivera, J. R. Schaibley, A. M. Jones, J. S. Ross, S. Wu, G. Aivazian, P. Klement, K. Seyler, G. Clark, N. J. Ghimire, *et al.*, "Observation of long-lived interlayer excitons in monolayer mose₂-wse₂ heterostructures," *Nature communications*, vol. 6, p. 6242, 2015.
- [160] X. Zhu, N. R. Monahan, Z. Gong, H. Zhu, K. W. Williams, and C. A. Nelson, "Charge transfer excitons at van der waals interfaces," *Journal of the American Chemical Society*, vol. 137, no. 26, pp. 8313–8320, 2015.
- [161] Y.-C. Lin, R. K. Ghosh, R. Addou, N. Lu, S. M. Eichfeld, H. Zhu, M.-Y. Li, X. Peng, M. J. Kim, L.-J. Li, *et al.*, "Atomically thin resonant tunnel diodes built from synthetic van der waals heterostructures," *Nature communications*, vol. 6, p. 7311, 2015.
- [162] H. Chen, X. Wen, J. Zhang, T. Wu, Y. Gong, X. Zhang, J. Yuan, C. Yi, J. Lou, P. M. Ajayan, *et al.*, "Ultrafast formation of interlayer hot excitons in atomically thin mos₂/wse₂ heterostructures," *Nature communications*, vol. 7, p. 12512, 2016.
- [163] Q. Zheng, W. A. Saidi, Y. Xie, Z. Lan, O. V. Prezhdo, H. Petek, and J. Zhao, "Phonon-assisted ultrafast charge transfer at van der waals heterostructure interface," *Nano letters*, vol. 17, no. 10, pp. 6435–6442, 2017.
- [164] Q. Zheng, Y. Xie, Z. Lan, O. V. Prezhdo, W. A. Saidi, and J. Zhao, "Phonon-coupled ultrafast interlayer charge oscillation at van der waals heterostructure interfaces," *Physical Review B*, vol. 97, no. 20, p. 205417, 2018.
- [165] D. Xiao, G.-B. Liu, W. Feng, X. Xu, and W. Yao, "Coupled spin and valley physics in monolayers of mos₂ and other group-vi dichalcogenides," *Physical Review Letters*, vol. 108, no. 19, p. 196802, 2012.
- [166] L. Xie and X. Cui, "Manipulating spin-polarized photocurrents in 2d transition metal dichalcogenides," *Proceedings of the National Academy of Sciences*, vol. 113, no. 14, pp. 3746–3750, 2016.
- [167] X. Chen, T. Yan, B. Zhu, S. Yang, and X. Cui, "Optical control of spin polarization in monolayer transition metal dichalcogenides," *ACS nano*, vol. 11, no. 2, pp. 1581–1587, 2017.
- [168] F. D. M. Haldane, "Model for a quantum hall effect without landau levels: Condensed-matter realization of the "parity anomaly"," *Phys. Rev. Lett.*, vol. 61, pp. 2015–2018, Oct 1988.
- [169] N. Goldman and J. Dalibard, "Periodically driven quantum systems: effective hamiltonians and engineered gauge fields," *Physical review X*, vol. 4, no. 3, p. 031027, 2014.

-
- [170] T. Oka and H. Aoki, “All optical measurement proposed for the photovoltaic hall effect,” in *Journal of Physics: Conference Series*, vol. 334, p. 012060, IOP Publishing, 2011.
- [171] G. Jotzu, M. Messer, R. Desbuquois, M. Lebrat, T. Uehlinger, D. Greif, and T. Esslinger, “Experimental realization of the topological haldane model with ultracold fermions,” *Nature*, vol. 515, pp. 237 EP –, 11 2014.
- [172] Y. H. Wang, H. Steinberg, P. Jarillo-Herrero, and N. Gedik, “Observation of floquet-bloch states on the surface of a topological insulator,” *Science*, vol. 342, no. 6157, pp. 453–457, 2013.
- [173] F. Mahmood, C.-K. Chan, Z. Alpichshev, D. Gardner, Y. Lee, P. A. Lee, and N. Gedik, “Selective scattering between floquet–bloch and volkov states in a topological insulator,” *Nature Physics*, vol. 12, pp. 306 EP –, 01 2016.
- [174] J. McIver, B. Schulte, F.-U. Stein, T. Matsuyama, G. Jotzu, G. Meier, and A. Cavalleri, “Light-induced anomalous hall effect in graphene,” *arXiv preprint arXiv:1811.03522*, 2018.
- [175] M. A. Sentef, M. Claassen, A. F. Kemper, B. Moritz, T. Oka, J. K. Freericks, and T. P. Devereaux, “Theory of floquet band formation and local pseudospin textures in pump-probe photoemission of graphene,” *Nature Communications*, vol. 6, pp. 7047 EP –, 05 2015.
- [176] S. T. Park, “Interference in floquet-volkov transitions,” *Physical Review A*, vol. 90, no. 1, p. 013420, 2014.
- [177] A. Eckardt and E. Anisimovas, “High-frequency approximation for periodically driven quantum systems from a floquet-space perspective,” *New Journal of Physics*, vol. 17, no. 9, p. 093039, 2015.
- [178] M. Kim, J. Hwang, L. A. Lepak, J.-w. Lee, M. G. Spencer, and S. Tiwari, “Improvement of carrier mobility of top-gated sic epitaxial graphene transistors using a pva dielectric buffer layer,” *Nanotechnology*, vol. 23, no. 33, p. 335202, 2012.
- [179] W. Zhu, V. Perebeinos, M. Freitag, and P. Avouris, “Carrier scattering, mobilities, and electrostatic potential in monolayer, bilayer, and trilayer graphene,” *Physical Review B*, vol. 80, no. 23, p. 235402, 2009.
- [180] J. Reimann, S. Schlauderer, C. Schmid, F. Langer, S. Baierl, K. Kokh, O. Tereshchenko, A. Kimura, C. Lange, J. Güdde, *et al.*, “Subcycle observation of lightwave-driven dirac currents in a topological surface band,” *Nature*, p. 1, 2018.
- [181] M. Claassen, C. Jia, B. Moritz, and T. P. Devereaux, “All-optical materials design of chiral edge modes in transition-metal dichalcogenides,” *Nature Communications*, vol. 7, pp. 13074 EP –, 10 2016.
- [182] C. Bena and G. Montambaux, “Remarks on the tight-binding model of graphene,” *New Journal of Physics*, vol. 11, no. 9, p. 095003, 2009.

- [183] A. Altland and B. D. Simons, *Condensed matter field theory*. Cambridge University Press, 2010.
- [184] K. v. Klitzing, G. Dorda, and M. Pepper, “New method for high-accuracy determination of the fine-structure constant based on quantized hall resistance,” *Phys. Rev. Lett.*, vol. 45, pp. 494–497, Aug 1980.
- [185] Y. Zhang, Y.-W. Tan, H. L. Stormer, and P. Kim, “Experimental observation of the quantum hall effect and berry’s phase in graphene,” *Nature*, vol. 438, pp. 201 EP –, 11 2005.
- [186] M. Katsnelson and K. Novoselov, “Graphene: New bridge between condensed matter physics and quantum electrodynamics,” *Solid State Communications*, vol. 143, no. 1, pp. 3 – 13, 2007. Exploring graphene.
- [187] M. V. Berry, “Quantal phase factors accompanying adiabatic changes,” *Proc. R. Soc. Lond. A*, vol. 392, no. 1802, pp. 45–57, 1984.
- [188] D. Xiao, M.-C. Chang, and Q. Niu, “Berry phase effects on electronic properties,” *Reviews of modern physics*, vol. 82, no. 3, p. 1959, 2010.
- [189] C.-K. Chiu, J. C. Y. Teo, A. P. Schnyder, and S. Ryu, “Classification of topological quantum matter with symmetries,” *Rev. Mod. Phys.*, vol. 88, p. 035005, Aug 2016.
- [190] G. Jotzu, *Probing Topological Floquet-Bands and Quantum Magnetism with Ultracold Fermions*. PhD thesis, ETH Zurich, 2017.
- [191] J. Cayssol, B. Dóra, F. Simon, and R. Moessner, “Floquet topological insulators,” *physica status solidi (RRL) – Rapid Research Letters*, vol. 7, no. 1-2, pp. 101–108, 2013.
- [192] J. Lischner, D. Vigil-Fowler, and S. G. Louie, “Physical origin of satellites in photoemission of doped graphene: An ab initio *gw* plus cumulant study,” *Phys. Rev. Lett.*, vol. 110, p. 146801, Apr 2013.
- [193] H. Hertz, “Ueber einen einfluss des ultravioletten liches auf die electriche entladung,” *Annalen der Physik*, vol. 267, no. 8, pp. 983–1000, 1887.
- [194] A. Einstein, “Einstein, a., 1905, ann. phys.(leipzig) 31, 132.,” *Ann. Phys.(Leipzig)*, vol. 31, p. 132, 1905.
- [195] S. Hüfner, *Photoelectron Spectroscopy (3rd Version)*. Springer, 2003.
- [196] A. Damascelli, “Probing the electronic structure of complex systems by arpes,” *Physica Scripta*, vol. 2004, no. T109, p. 61, 2004.
- [197] L. Hedin, “On correlation effects in electron spectroscopies and the *gw* approximation,” *Journal of Physics: Condensed Matter*, vol. 11, no. 42, p. R489, 1999.

-
- [198] C. N. Berglund and W. E. Spicer, “Photoemission studies of copper and silver: Theory,” *Phys. Rev.*, vol. 136, pp. A1030–A1044, Nov 1964.
- [199] M. P. Seah and W. Dench, “Quantitative electron spectroscopy of surfaces: A standard data base for electron inelastic mean free paths in solids,” *Surface and interface analysis*, vol. 1, no. 1, pp. 2–11, 1979.
- [200] A. F. Starace, “Length and velocity formulas in approximate oscillator-strength calculations,” *Phys. Rev. A*, vol. 3, pp. 1242–1245, Apr 1971.
- [201] S. Ismail-Beigi, E. K. Chang, and S. G. Louie, “Coupling of nonlocal potentials to electromagnetic fields,” *Phys. Rev. Lett.*, vol. 87, p. 087402, Aug 2001.
- [202] M. Bukov and A. Polkovnikov, “Stroboscopic versus nonstroboscopic dynamics in the floquet realization of the harper-hofstadter hamiltonian,” *Phys. Rev. A*, vol. 90, p. 043613, Oct 2014.
- [203] M. Bukov, L. D’Alessio, and A. Polkovnikov, “Universal high-frequency behavior of periodically driven systems: from dynamical stabilization to floquet engineering,” *Advances in Physics*, vol. 64, no. 2, pp. 139–226, 2015.
- [204] M. Floquet, “Sur les equations differentielles lineaires a coefficients periodique,” *Annales scientifiques de l’Ecole Normale Supérieure*, vol. 2, no. 47, 1883.
- [205] J. H. Shirley, “Solution of the schrödinger equation with a hamiltonian periodic in time,” *Physical Review*, vol. 138, no. 4B, p. B979, 1965.
- [206] Y. B. Zel’Dovich, “The quasienergy of a quantum-mechanical system subjected to a periodic action,” *Soviet Physics JETP*, vol. 24, no. 5, pp. 1006–1008, 1967.
- [207] H. Sambe, “Steady states and quasienergies of a quantum-mechanical system in an oscillating field,” *Physical Review A*, vol. 7, no. 6, p. 2203, 1973.

Acknowledgements

First and foremost I would like to express my gratitude to my supervisor, Isabella Gierz, for giving me the opportunity to work on this project. Thank you for your energy, your scientific guidance, your patience, all the great discussions and the many lessons you taught me.

I also wish to thank my co-advisor, Ludwig Mathey, for co-refereeing my thesis, for various *focus meetings* and for always being there in urgent cases.

I further thank Andrea Cavalleri for letting me be part of the condensed matter department and the opportunity to attend the group meetings.

Special thanks go to my colleagues in the lab, Mariana, Razvan and Hubertus with whom I went through all the ups and downs of keeping the *ARPESzilla* running. Thank you for all the good times at work and also outside of CFEL.

There are many people that I am grateful to have met during my time at the Max-Planck Institute in Hamburg. Apart from being great scientists, you made this time special and enjoyable:

Srivats - thank you for your many advices and debates on work and life in general and also for joining a few of my training sessions. Even though you gave up far too quickly on that last one.

Eliza, Tobia, Andrea - thank you for your help and introducing Hamburg to me, especially in the beginning of my time here. Eliza, I thank you for lively conversations and being what I consider my personal source for gossip.

Ankit, Alex, Ken - thanks for the great tradition of sunday NFL nights with Icke and Co. We should keep it up.

Matthias, Ivanka, Sebastian, all three Michaels, Alice, Thomas, Toru, Guido, Regina, Jörg, Boris, Michaela - thank you for improving the everyday life in Hamburg, you will all be missed.

I was fortunate to have spent my first ten months of my PhD at the Max-Planck-Institute for Solid State Research, in Stuttgart.

I wish to thank my advisor during that time, Christian Ast, with whom I was still able to discuss regularly even after leaving for Hamburg.

Special thanks go to Carola who did a great job of introducing the experimental setup to me, to Andreas who spent a beamtime with me, to Cornelius who ended up in Hamburg by now and to the rest of the group, including Bert, Matthias, Christian, Diana, Steven, Stefan, Alex, Ulli,

Klaus and many more.

I also thank Philip Hofmann and his group members, Marco, Charlotte, Jill and the others for a wonderful beamtime in Aarhus.

The list would not be complete if I did not acknowledge the ARTEMIS crew including Emma, Paulina, Yu and Richard. A big shout-out goes to Cephise who always kept things working and took me to boot camps during lunchbreaks.

Many thanks go to Camilla Coletti and her staff for providing us with all the samples, especially to Antonio who joined us for a week in Hamburg and who I met for another week of beamtime at ARTEMIS.

I further thank my chiropractor, Rene Ölenschläger, who keeps fixing my back and keeps me in a good physical condition.

With great emphasis, I would like to thank my father and brother for the unlimited support throughout the time of this thesis and all my life. Shohreh, Darius, Hans-Jörg, I am grateful to call you family as well. Finally, Wiebke, I thank you for your love and care, I am happy to have you in my life.

Eidesstattliche Versicherung / Declaration on oath

Hiermit erkläre ich an Eides statt, dass ich die vorliegende Dissertationsschrift selbst verfasst und keine anderen als die angegebenen Quellen und Hilfsmittel benutzt habe.

Die eingereichte schriftliche Fassung entspricht der auf dem elektronischen Speichermedium.

Die Dissertation wurde in der vorgelegten oder einer ähnlichen Form nicht schon einmal in einem früheren Promotionsverfahren angenommen oder als ungenügend beurteilt.

Hamburg, den 22.10.2018

Sven Aeschlimann